COMPUTATIONAL INVESTIGATION OF THERMOCAPILLARY MIGRATION OF BUBBLES AND DROPS IN ZERO GRAVITY

by

Selman Nas

A dissertation submitted in partial fulfillment
of the requirements for the degree of
Doctor of Philosophy
(Aerospace Engineering)
in The University of Michigan
1995

Doctoral Committee:

Associate Professor Grétar Tryggvason, Chairperson
Associate Professor Luis P. Bernal
Assistant Professor Steve L. Ceccio
Professor Gerard M. Faeth
David Jacqmin, Research Scientist, NASA Lewis Research Center

TABLE OF CONTENTS

CHAPTER

LIST OF FIGURES

Figure

CHAPTER I

INTRODUCTION

1.1 Motivation

Bubbles and drops in an ambient fluid with a temperature gradient will move toward the hot region due to thermocapillary forces. Surface tension decreases with increasing temperature and the nonuniform surface tension of the bubble surface causes shear stresses that are transmitted to the outer fluid by viscous forces, thus inducing a motion of the bubble in the direction of the thermal gradient. In space, where buoyancy forces are negligible, thermocapillary forces can be dominant. For material processing in microgravity, thermal migration can be used, for example, to remove gas bubbles or liquid drops in melts before solidification. It has been suggested that it is possible to produce high quality glass in space because of the ability to process it without a container (Uhlmann (1982)). However, bubbles due to chemical reactions have to be removed to achieve this. Thermocapillary migration could provide a way to do this in the absence of gravity. Vapor bubbles may also form due to evaporation in liquid-rockets which are used to power space vehicles and space probes (Ostrach (1982)). Similarly, the cooling system of the Space Shuttle uses liquids from which gas bubbles might form. The bubbles in these systems should be managed in order to have a properly working systems. Thermocapillary migration can also be important in the design of two-phase heat exchangers for space applications. Accumulations of bubbles on heated surfaces can act like an insulator and prevent heat transfer to the surface. To understand the interaction of many bubbles during thermocapillary induced motion and to investigate the effect of the various governing parameters, here we solve the full Navier-Stokes equations and the energy equation for both fluids, computationally.

1.2 Historical Background

In this section, we review some of the previous experimental, theoretical, and numerical investigations that have been carried out on thermocapillary migration of bubbles and drops.

Thermal migration of gas bubbles was first examined by Young *et al.* (1959), both theoretically and experimentally. Young *et al.* were able to hold a buoyant gas bubble stationary by applying a downward temperature gradient, found a first order approximation to the terminal velocity in the limit of negligible convective transport of momentum and energy, under the assumption that the bubble maintains a spherical shape. They also verified that the temperature gradient required to hold a bubble stationary was proportional to the bubble radius and that this gradient is independent of viscosity as predicted by their theoretical model.

Hardy (1979) performed experiments similar to Young *et al.* He reduced some of the experimental inaccuracies in the experiments of Young *et al.* and also obtained the temperature gradient needed to counter the buoyancy effect. His results were in good agreement with the theoretical predictions of Young *et al.*

Thompson (1979) and Thompson *et al.* (1980) used a NASA zero gravity drop tower to do experiments in 5.2 seconds of free fall. They used nitrogen bubbles in different host fluids. The results showed that the thermocapillary motion of bubbles occured in each test fluid except distilled water. Thompson suggested that the phenomena did not occur in distilled water due to surfactant contamination.

Meritt and Subramanian (1988) performed experiments on bubbles in silicon oil in a downward temperature gradient, overcoming the buoyant rise of the bubble. Although the bubbles in those experiments increased in size by as much as 100% during the experiment, due to the mass transfer from the liquid, their results showed good agreement with the work of Young *et al.* The surface tension, which was extracted from the experiments, was also in good agreement with earlier measurements of Hardy (1979).

Experimental investigations of the thermocapillary migration of liquid drops is a more recent field of research than work using gas bubbles. Wozniak and Siekman (1989) carried out a low gravity thermocapillary migration experiment on liquid drops in the European sounding rocket program. They reported that for high Reynolds (Re) and Marangoni (Ma) numbers, the measured migration velocities were close to the prediction given by Subramanian (1983). For intermediate non-dimensional numbers, however, they observed larger deviations from the theoretical model of Subramanian (1983).

Barton and Subramanian (1989) have completed measurements of drop migration speeds in circumstances where convective transport effects were negligible. These results are generally in agreement with the predictions of Young *et al.*

Rashidna and Balasubramaniam (1991) carried out experiments on drops in silicon oil using density matched systems. Drops moving towards the hot region in a vertical temperature gradient were observed. After a long time, however, drops began moving towards the cooler side. They attributed this surprising behavior to mass transfer between the phases, causing the drops to become more dense than the host-fluid.

Bratukhin (1976) derived an analytical solution for the thermocapillary flow of bubbles and drops based on a power series expansion in terms of the Marangoni number, and found the particle velocity, the fluid velocity, the temperature field, and the pressure field by using an Oseen approximation. Thus, his results are valid for small Reynolds numbers, to $O(Re)$. In zero gravity, and in the limit of zero Reynolds number, his formula is the same as the one found by Young *et al.*

Later, Subramanian (1981) obtained the migration velocity of a gas bubble for small, but nonzero convective heat transfer by using asymptotic expansion technique. In his analysis, it is assumed that the bubble is nondeformable and that the Reynolds number is small enough to be taken as zero. The migration velocity of the bubble is given up to $O(Ma^2)$. As the results show, the effect of convective transport of energy is to reduce the migration velocity of bubbles. Subramanian (1983) later extended his work to liquid drops. In the proper limit, his results give the correct value of the migration velocity for gas bubbles. For certain physical properties, it was shown that the drop velocity can be higher with increasing Marangoni number; in contrast, for bubbles, the effect is always a reduction in the migration velocity.

Balasubramaniam and Chai (1987) have given an exact solution for the migration velocity of a single drop in the limit of negligible convective transport of energy. They also computed the shape of the droplet, when deformations from a spherical shape are small. Their results are in agreement with previous results, such that the bubbles tend to deform oblately, and that droplets tend to elongate in the flow direction while droplets of the same density as the ambient fluid do not deform.

Shankar and Subramanian (1988) reconsidered the thermocapillary migration of a gas bubble in the limit of a zero Reynolds number at values of the Marangoni number ranging from 0 to 200, solving the energy equation by a finite difference method. They confirmed that increasing Marangoni number decreases the migration velocity of a gas bubble and presented a very simple formula for the bubble migration velocity for $Ma > 25$, by fitting their numerical solution.

Siekman and Szymczyk (1988) numerically solved the thermocapillary motion for a gas bubble, accounting fully for the convective transport of energy and momentum while assuming a nondeformable bubble. Their results show that convective energy and momentum transport effects tend to reduce the bubble migration velocity.

Balasubramaniam and Lavery (1989), extended the work of Siekman and Szymczyk (1988) and, for a large range of non-dimensional numbers, numerically solved the problem for an isolated axisymmetric spherical bubble. They found that the scaled bubble velocity is more sensitive to the Marangoni number at a fixed Reynolds number than to the Reynolds number at a fixed Marangoni number.

Haj-hariri *et al.* (1990) have examined the inertial effects on the thermocapillary velocity of a drop. It was found that with the convective transfer of heat neglected, droplets with densities higher/lower than the outside liquid deform to prolate/oblate spheroidal shapes, at small values of the Capillary and Reynolds numbers. It was shown that the migration velocity could increase, decrease, or remain unchanged depending on the ratios of physical properties.

Chen and Lee (1992) investigated numerically the effect of surface deformation on the terminal velocity of a single bubble and concluded that surface deformation reduces the terminal velocity considerably.

Other investigators have examined the thermocapillary motion for two bubbles or drops, but only for small Marangoni and Reynolds numbers. Meyyapan *et al.* (1983)

investigated the motion of two bubbles moving along their line of centers. They found that each bubble moves with the same velocity that it has if it is isolated. Their analysis also assumed that convective transport of energy and momentum is sufficiently small so it can be neglected and that the bubbles do not deform. When the bubbles differed in size, the smaller bubble moved faster than if isolated while the larger bubble moved slower. However, these interaction effects generally were small.

Meyyapan and Subramanian (1984) extended the analysis of Meyyapan *et al.* (1983) to the motion of two bubbles oriented arbitrarily with respect to the temperature gradient, using an approximate method. They found that a small bubble does not affect the motion of a larger bubble to any significant degree. It was further shown that if two bubbles are close and oriented with their line of centers perpendicular to the temperature gradient, the small bubble sometimes moves opposite to the direction of the temperature gradient.

Feuillebois (1989) has given an exact solution for the problem considered by Meyyapan *et al.* (1983).

The motion of two liquid drops oriented arbitrarily with respect to a temperature gradient was examined theoretically by Anderson (1985) in zero Reynolds and Marangoni number limit. In his analysis, where the method of reflections was used to solve the governing equations, the convective transport of energy and momentum as well as gravitational effects were neglected. He also utilized his two-drop theory to find the effect of the volume fraction of the drops on the mean drop velocity in a bounded suspension. It is shown that the mean velocity of a suspension is lower than for a single drop.

Acrivos *et al.* (1990) have studied the thermocapillary motion induced in a cloud of bubbles by a uniform temperature gradient under the assumptions that the bubbles are all the same size, that the surface tension is high enough to keep the bubbles spherical, and that the bubbles are non-conducting. It was shown that in a cloud of n particles surrounded by an infinite expanse of fluid, the velocity of each sphere under creeping flow conditions is equal to the velocity of an isolated particle, unchanged by interactions between particles.

Keh and Chen (1990) considered the axisymmetric thermocapillary motion of two spherical droplets in a constant applied temperature gradient along their line of centers under creeping flow conditions. It was shown that for the thermocapillary motion of two identical liquid droplets, both migrate faster than the velocity they would posses if isolated. For the case of two gas bubbles with equal radii, there was no particle interaction for all separation distance.

Keh and Chen (1992) investigated the axisymmetric thermocapillary motion of a chain of spherical droplets along their line of centers in a quasi-steady limit of conservation of energy and momentum by a combined analytical-numerical study. For the case of two droplets, the migration velocity of each drop were confirmed. For the special case of multiple gas bubbles, it was demonstrated that the migration velocity of each bubble is unaffected by the presence of the others if all the bubbles have identical radii.

Zhang and Davis (1992) examined the pairwise collision rate of small spherical drops undergoing thermocapillary migration in a dilute dispersion under creeping flow conditions by using a trajectory analysis. It was found that increases in the viscosity and/or thermal conductivity of the drop fluid decrease the collision efficiency, described as the effects of the drop interaction on collision rate, due to the effects of hydrodynamic and thermocapillary interactions.

Strape (1992) analytically examined the interaction between bubbles in the zero Marangoni and Reynolds number case. He also assumed that the Capillary number is negligible so that the bubbles are always spherical. He has given the trajectories for the two-bubble case in these limits. He also found that for a statistically homogeneous cloud of bubbles, the bubble collision rate increases with the standard deviation of the bubble size distribution.

Wei and Subramanian (1993) theoretically investigated the quasi-static thermocapillary migration of a chain of two and three spherical bubbles in an unbounded fluid with a uniform temperature gradient, at the limit of vanishing Reynolds and Marangoni number. They explored the flow topology and identified reverse flow wakes.

Keh and Chen (1993) considered the more general problem of droplet interactions in thermocapillary migration. They also solved this general problem in the limit of zero Reynolds and Marangoni numbers and showed that the terminal velocity of a drop is not affected by the presence of other drops if they all are equal in size. They have also examined the effect of volume fractions on the average thermocapillary migration velocities in a bounded dilute suspension.

The interaction between bubbles and drops and plane surfaces has been the subject of other investigations. Meyyapan *et al.* (1981) investigated theoretically the slow axisymmetric thermocapillary migration of a spherical gas bubble normal to a solid plane surface and a free liquid surface. Their calculation showed that the effect of the plane surface is to decrease the bubble's migration velocity. They also demonstrated that the distance at which the bubble starts to be affected by the presence of the plane surface is much smaller than for a gravity driven motion. They explained this behavior in terms of the decay rates of the disturbance velocity fields.

A gas bubble in a temperature gradient with an arbitrary orientation with respect to the plane surface, was studied by Meyyapan and Subramanian (1987), extending the work of Meyyapan *et al.* (1981). Their results show that the presence of the planar surface always reduces the migration velocity of the bubble. The highest reduction is observed when the bubble moves normal to the plane surface.

Ascoli and Leal (1990) considered the thermocapillary migration of a deformable drop moving normal to a planar wall and found that the deformation increases with increasing effective Capillary number.

Chen and Keh (1990) examined the migration of a drop towards a planar surface under creeping flow conditions. It was found that for the motion of a droplet normal to a solid plane, the effect of the plane surface is to reduce the migration velocity of the droplet. For the case of droplet migrating toward a free surface, the droplet velocity can be either greater or smaller than that which would exist in the absence of the plane surface, depending on the relative thermal conductivity of the droplet and its relative distance from the plane.

Chen *et al.* (1991) examined the steady, creeping, thermocapillary migration of a spherical fluid particle in a tube owing to an imposed axial temperature gradient under conditions of axisymmetry, negligible thermal convection and an insulated tube wall. They studied the influence of wall-fluid particle hydrodynamic and thermal interactions in determining the thermocapillary migration velocity.

1.3 Current Work

The literature on thermal migration is more extensive for single bubbles or drops than for the interaction of many bubbles and drops. In most previous work, it has been assumed that the bubbles do not deform and that convective transfer can be neglected. Here, we present results for both single and several bubbles and drops by solving the full governing equations numerically in two and three dimensions. In our computations, we do not impose any restriction on the shape of the bubbles, although we find that the bubbles remain nearly spherical in most cases.

The full Navier-Stokes equations, as well as the energy equation for the temperature distribution, are solved for the fluid inside and outside of the bubbles by a Front Tracking/Finite Difference Method. The material properties of the bubble fluid and the ambient fluid are different, and we assume temperature dependent surface tension. We explore the dependence of the thermal migration velocity and the deformation on the various non-dimensional parameters.

The definition of the physical problem and the mathematical formulation, as well as the governing parameters, are covered in Chapter II. Chapter II also includes a description of the numerical method used to solve the governing equations and the validation of the two and three dimensional code.

In Chapter III, we start with the rise of a single bubble and present the effect of the various governing parameters on the migration velocity and the deformation of the bubble. Then, we move to the interaction of two, two-dimensional bubbles and study the effect of the initial condition of bubbles on their interaction. The interaction between two bubbles or two drops is then explored in detail by two and three dimensional simulations in the rest of Chapter III.

We present the behavior of large numbers of bubble systems in Chapter IV. In the first part of Chapter IV, we consider simulation of a cloud of equal-sized bubbles. The evolution of six and sixteen equal-sized bubbles is explored by two-dimensional simulation. Then, the interactions of nine bubbles is investigated by fully three-dimensional simulations. Similar to the mono-dispersed case, the behavior of a polydispersed system is explored in the rest of Chapter IV. First, the interaction of six and sixteen unequal-sized two-dimensional bubbles is presented, followed by fully three-dimensional computation of nine, unequal-sized bubbles.

Chapter V contains the conclusions, and suggestions for future work on the thermocapillary migration of bubbles and drops.

CHAPTER II

FORMULATION AND NUMERICAL METHOD

The physical problem and the computational domain is sketched in Figure 2.1. We have a wall bounded region in the z direction and the domain is periodic in the x direction. The bubble has constant physical properties denoted by the subscript i and the ambient fluid has properties denoted by the subscript o. The surface tension varies along the interface. The top wall is hot and the bottom wall is cold, and initially, the temperature is linearly increasing in the z direction.

2.1 Governing Equations

The Navier-Stokes equations are valid for both fluids, and a single set of equations can be written for the whole domain as long as the jump in viscosity and density is correctly accounted for and surface tension is included. The Navier-Stokes equations, in conservative form are as follows:

$$\frac{\partial \rho \mathbf{u}}{\partial t} + \nabla(\rho \mathbf{u}\mathbf{u}) = -\nabla p + \nabla \cdot \mu(\nabla \mathbf{u} + \nabla \mathbf{u}^T) + \int_B \delta(\mathbf{x} - \mathbf{x}_f)(\sigma \kappa \mathbf{n} + \frac{\partial \sigma}{\partial s}\mathbf{t})\, ds \tag{2.1}$$

In the last term, we include the surface tension forces acting on the interface as a body force by representing it as a delta function. Here, $\mathbf{u}$ is the velocity field, ρ is the density, p is the pressure, μ is the viscosity, σ is the surface tension, κ is the mean curvature, $\mathbf{n}$ is a unit normal vector, $\mathbf{t}$ is a unit tangent vector, δ is the delta function, $\mathbf{x}_f$ is the position of the interface and the integral is over the interface separating the fluids.

The energy equation can be written as follows:

$$\rho c_p \left(\frac{\partial T}{\partial t} + \nabla \cdot (\mathbf{u} T) \right) = \nabla \cdot (k \nabla T), \tag{2.2}$$

where T is the temperature and k and c_p are the coefficients of heat conduction and heat capacity, respectively. Both fluids are immiscible and the physical properties are constant in each fluid. Therefore, the equations of state for density, viscosity, heat capacity and heat conduction can be written as follows;

$$\frac{D\rho}{Dt} = 0; \qquad \frac{D\mu}{Dt} = 0 \tag{2.3}$$

$$\frac{Dk}{Dt} = 0; \qquad \frac{Dc_p}{Dt} = 0. \tag{2.4}$$

The incompressibility constraint gives the divergence free velocity field condition as follows;

$$\nabla \cdot \mathbf{u} = 0. \tag{2.5}$$

If we combine the momentum equation and the incompressibility condition, this leads to a non-separable elliptic equation for the pressure. Since the physical properties are taken to be constant, the density field is independent of temperature variation and we have therefore excluded natural convection in this problem.

We take the surface tension to be a linearly decreasing function of the temperature:

$$\sigma = \sigma_o + \sigma_T (T_o - T) \tag{2.6}$$

where

$$\sigma_T = -(d\sigma/dT) = \text{constant}$$

and σ_o is the surface tension at a reference temperature T_o. In many cases, σ_T can be assumed to be a constant and for simplicity we assumed that it is so here. σ_T is positive for most fluids (see Braun *et al.* 1993 for negative value of σ_T). Therefore, increasing temperature reduces the surface tension. In a nonuniform temperature gradient, the cold side of the bubble will have a higher surface tension than the warm side and it will therefore pull surface from the warm side, where surface will be generated, around the bubble to the cold end, where the surface will disappear. This movement of the surface, with its viscous drag upon the outer fluid, will pick up a sheet of liquid and jet it off the cold back end. By jetting liquid one way, the bubble propels itself up the temperature gradient. Thermodynamically, such a self-propelling bubble is a heat engine. Whenever surface is created, heat is absorbed, and whenever surface is destroyed heat is given off. Therefore a swimming bubble absorbs heat at its hot end and rejects heat at its cold end (Trefethen, 1963).

2.2 Non-dimensional Numbers

Following other investigators we present our results in non-dimensional variables. The flow is governed by the following variables;

$$a,\ \sigma_o,\ \mu_o,\ \rho_o,\ c_{po},\ k_o,\ \mu_i,\ \rho_i,\ c_{pi},\ k_i,\ \sigma_T,\ \text{and}\ \nabla T_\infty.$$

Here a is a typical bubble or drop radius, σ_o is the average surface tension, μ is the viscosity, ρ is the density, c_p is the coefficient of heat capacity, k is the coefficient of heat conduction, σ_T is the rate of change of surface tension with temperature, and ∇T_∞ is the undisturbed temperature gradient in the ambient fluid far from the bubble. The physical properties of the bubble are denoted by the subscript i and those of the ambient fluid by the subscript o. This leads to the following non-dimensional numbers;

$$\frac{\rho_i}{\rho_o}, \ \frac{\mu_i}{\mu_o}, \ \frac{c_{pi}}{c_{po}}, \ \frac{k_i}{k_o}, \ Ma = \frac{\sigma_T a^2}{\mu_o \alpha_o} \nabla T_\infty,$$

$$Re = \frac{\sigma_T \rho_o a^2}{\mu_o^2} \nabla T_\infty, \text{ and } Ca = \frac{\sigma_T a}{\sigma_o} \nabla T_\infty$$

where,

$$\alpha_o = \frac{k_o}{\rho_o c_{po}}$$

Here, Ma is the Marangoni number, Re is the Reynolds number, and Ca is the average Capillary number. The average Capillary number is computed at the middle of the domain in the vertical direction. These three non-dimensional numbers are based on the properties of the outer fluid. Sometimes, the Prandtl number, $Pr_o = \nu_o/\alpha_o$, is used instead of the Re number. α_o is the thermal diffusivity of the outer fluid. As is usually done in the literature for Marangoni bubble motion, we define a reference velocity by:

$$U_r = \frac{\sigma_T a}{\mu_o} \nabla T_\infty .$$

The non-dimensional numbers can now be written in a much simpler form:

$$Ma = \frac{U_r a}{\alpha_o}, \qquad Re = \frac{U_r a}{\nu_o}, \qquad Ca = \frac{\mu_o U_r}{\sigma_o}$$

The Marangoni number is the Péclet number as it is usually used in the heat transfer literature and is the product of the Prandtl and the Reynolds number. When we present our results, velocities will be scaled by the reference velocity defined above and time will be scaled by the ratio of the initial bubble radius and the reference velocity. In the creeping flow regime, it is more appropriate to use diffusion time scale since the convection is negligible. Either viscous time scale or thermal time scale can be used. When the Prandtl number is very small than unity, the thermal field attains its steady-state value while the fluid motion is just beginning to develop. Therefore, the flow is governed by the viscous time scale. When the Prandtl number is very large than unity, the fluid motion becomes quasi-static with a slowly-developing thermal field. Hence, the thermal time scale determines when the bubble reaches a steady state as pointed out by Dill (1988).

When the non-dimensional numbers are either small or large, several interesting limiting cases arise. At the zero Marangoni number limit, the energy equation reduces to the Laplace's equation for temperature since the convective transport of energy can be neglected in this case. Hence, the problem becomes a quasi-static problem. For a gas bubble, when the physical properties of the gas are much smaller than those of the ambient fluid, the energy transfer on the bubble surface can be neglected. This implies that the isotherms should be perpendicular to the bubble surface. Small Prandtl number results apply to liquid metals and large Prandtl number to heavy oils. Liquids have Prandtl numbers on the order of unity. Typical values are Pr=7 for water and Pr=0.72 for air, at standard conditions. The zero Reynolds number limit reduces the momentum equation to the steady case since inertial effects can be neglected in this limit.

When the Marangoni number is large, the convective terms in the energy equation are dominant. In this limit, conduction of energy can be neglected. If the Reynolds number is of the order of unity, large Prandtl numbers correspond to high Marangoni numbers. Heavy oils, like silicon oil, have large Prandtl numbers, on the order of 10^3.

In the limit of zero Capillary number, it can be assumed that deformation from a spherical shape is negligible. As the Capillary number increases, however, deformation of the bubble increases. If the deviation from a spherical shape is large, the scaled terminal velocity of the bubble/drop decreases. In the zero Capillary, Marangoni and Reynolds number limit, the scaled migration velocity of a gas bubble is known to be 0.5.

In order to report the deformation of a bubble in later chapters, we define the deformation of a bubble as follows;

$$\gamma = \frac{1-\epsilon}{1+\epsilon}$$

where

$$\epsilon = \frac{\text{minor axis of the bubble}}{\text{major axis of the bubble}}.$$

In the simulations presented in this thesis, we include all terms in the governing equations and do not impose any restrictions inherent for these limiting cases.

2.3 Numerical Method

The numerical technique used for the simulations presented here is the Immersed Front Tracking method for multi-fluid flows developed by Unverdi (1990) and discussed by Unverdi and Tryggvason (1992 a,b). To solve the Navier-Stokes equations we use a fixed, regular, staggered grid and discretize the momentum equations using a conservative, second order centered difference scheme for the spatial variables and an explicit second order time integration method. We have used first order time integration in other problems and generally find little differences for the relatively short simulation times of interest here. The effect does show up in long time simulations, however, and is usually accompanied by a failure to conserve mass. In the computations discussed here, mass is always conserved within a fraction of a percent. The interface is represented by separate computational points that are moved by interpolating their velocity from the grid. These points are connected to form a front that is used to keep the density and viscosity stratification sharp and to calculate surface tension forces. At each time step, information must be passed between the front and the stationary grid. This is done by a method that has become known as the Immersed Boundary Technique and is based on assigning the information carried by the front to the nearest grid points. While this replaces the sharp interface by a slightly smoother grid interface, all numerical diffusion is eliminated since the grid-field is reconstructed at each step.

The original Immersed Boundary Technique was developed by Peskin and collaborators (see e.g. Peskin (1977)) for homogeneous flows. The extension to stratified flows includes a number of additional complications. The first is that density now depends on the position of the interface and has to be updated at each time step. There are several ways to do this but we use a variant of the method developed by Unverdi (1990) where the density jump at the interface is distributed onto the fixed grid to generate a grid-density-gradient field. The divergence of this field is equal to the Laplacian of the density field and the resulting Poisson equation can be solved efficiently by a Fast Poisson Solver. The particular attraction of this method is that close interfaces can interact in a very natural way, since the grid-density gradients simply cancel. Therefore, when two interfaces come close together the full influence of the surface tension forces from both interfaces is included in the momentum equations, but the mass of the fluids in the thin layer between the interfaces—which is very small—is neglected. A second complication is that the pressure equation now has a nonconstant coefficient (or is non-separable) since the density varies. This prevents the use of Fast Poisson Solvers based on Fourier Methods, or variants there of. We used a simple SOR for many of our early computations (in the so-called Black and Red form for computations on a CRAY computer), but here, a multigrid package (MUDPACK from NCAR) was used for most of the computations.

The computation of the surface tension forces poses yet another difficulty. Generally, curvature is very sensitive to minor irregularity in the interface shape and it is difficult to achieve accuracy and robustness at the same time. However, by computing the surface tension forces on each element directly by

$$F_s = \oint_{elem} \sigma \mathbf{n} \times \mathbf{t} ds, \tag{2.7}$$

we explicitly enforce that the integral over any portion of the surface gives the right value, and for closed surfaces, in particular, we enforce that the integral of surface tension forces is zero. This is important for long time simulations since even small errors can lead to a net force that moves the bubble in an unphysical way. Here, $\mathbf{n}$ is the surface normal vector, $\mathbf{t}$ is the unit vector tangent to the boundary of the surface element, σ is the surface tension coefficient.

The energy equation is solved in the same way as the momentum equation. Central differencing is used for the spatial derivatives on the staggered mesh and a second order time stepping is used to advance the temperature in time. The temperature on the front is interpolated from the neighboring stationary grid points by using an interpolation function invented by Peskin (1977). Given the temperature, surface tension can be found and the surface forces computed. The momentum and the energy equations are coupled through this relation.

We use different platforms to compute the simulations. This includes CRAY YMP and CRAY C90 supercomputers as well as HP, IBM RS/6000, IBM SP1 workstations. Due to the frequent crashes and the use of backup files in order to choose the low load times, it is hard to estimate the time to complete each run. It varies from one day to several days on a local workstation for two-dimensional simulations. This goes as high as two months for three dimensional simulations on workstations.

2.4 Validation

In order to establish the correctness of the method presented here, we have done three tests to compare our results with existing analytical results. The first test is for the creeping flow regime. The terminal velocity of a single bubble rising in an unbounded domain has been found by Young *et al.* (1959). Young *et al.* utilize the solution of Hadamard and Rybczynski (1911) for flow around a fluid sphere and assume that convective transport of momentum and energy can be neglected. In other words, they assume that Reynolds and Marangoni numbers are very small and that the convective terms in the governing equations can be neglected. Once this is done, the problem becomes quasi-static. The energy equation reduces to a form where the Laplacian of temperature vanishes over the whole domain. They also assume that deformation from a spherical shape is negligible. This implies that Capillary effects can be neglected. They have given the scaled rising velocity as follows:

$$V_{YGB} = \frac{2}{(2+k^*)(2+3\mu^*)} \tag{2.8}$$

where k^* is the ratio of the coefficient of heat conductivity of the bubble to that of the ambient fluid and μ^* is the ratio of the viscosity of the bubble to that of the ambient fluid. For a gas bubble, since the conductivity and viscosity ratios are negligible, this formula reduces to $V_{YGB} = \frac{1}{2}$.

In an attempt to compare our results with the migration velocity of a bubble in the creeping flow regime, we first conducted resolution tests using two-dimensional simulations. The non-dimensional numbers are $Re = 2.5 \times 10^{-3}$, $Ma = 2.5 \times 10^{-3}$ and $Ca = 10^{-3}$ and the ratios of the physical properties of the bubble to that of the outer fluid is 0.5. We have examined the sensitivity of the solution to the grid resolution by simulating a single bubble on 32×32, 64×64 and 128×128 grids for a square domain which extends four bubble radii in each direction. This corresponds to 16, 32 and 64 mesh points per bubble, respectively. As we increase the resolution the terminal velocities converge and the difference between the 64×64 grid and 128×128 grid is about 2%. Figure 2.2 shows the velocity versus time for these three runs.

We then do fully three dimensional simulations of a single bubble to compare our results with three-dimensional analytical solutions in the creeping flow regime. In order to reduce the computational costs, and due to limited computational resources, 32 grid points per bubble diameter were used in the three dimensional simulations. We have done these simulations for $Re = 2.5 \times 10^{-3}$, $Ma = 2.5 \times 10^{-3}$ and $Ca = 10^{-3}$. The ratios of the physical properties of the bubble to that of the outer fluid (k^* and μ^* in Equation (2.8)) are 0.5. The theoretical value of the rising velocity for a bubble migrating in an unbounded domain is 0.228 from Equation (2.8). Figure 2.3 shows the results of the fully three dimensional simulation of a single bubble migrating at steady state for these non-dimensional numbers. The migration velocity versus the distance, H, between the wall and the bubble centroid, scaled by bubble radius, is plotted in Figure 2.3. Since we have walls on the top and bottom of the computational domain as well as periodic horizontal boundaries, there are wall effects which reduce the rise velocity of the bubble. As we increase the size of the computational box, Figure 2.3 shows that the results approach the unbounded domain results.

For one of the cases in Figure 2.3, where the bubble is two bubble radii away from the wall, we plot the bubble and the temperature field in the middle plane of the computational box at steady state in Figure 2.4. The detailed structure of the isotherms is shown in the middle plane in Figure 2.5. Figure 2.5 shows that the temperature field is consistent with the theoretical prediction that the temperature gradient inside the bubble does not change and the temperature field is uniform. For the same simulation, Figure 2.6 shows the velocity field in the middle cross sectional plane of the bubble while Figure 2.7 shows the detailed structure of this velocity field in the same plane.

In our second test we examine the qualitative behavior of a single bubble in the creeping flow regime with respect to changes in the ratio of the physical properties. Equation (2.8) indicates that the density and the heat capacity ratio do not play a role in the migration velocity of the bubble. The migration velocity is only affected by viscosity and heat conductivity according to Equation (2.8). Figure 2.8 shows the scaled migration velocity with respect to time for different viscosity ratios. When the bubble reaches steady state, it is seen clearly that beyond the viscosity ratio $\mu^* = 1/50$, the effect is negligible. This is consistent with Equation (2.8). While the viscosity ratio changes, the ratio of other physical properties are kept constant at unity. Similarly, the effect of the heat conductivity ratio is shown in Figure 2.9. While we decrease the ratio, we see that once it is smaller than about $k^* = 1/40$, the effect is negligible. Both of these results are qualitatively consistent with the prediction of Equation (2.8). We have also done a similar test for the density and heat capacity ratios. Figure 2.10 shows the effect of the density ratio while the effect of the heat capacity ratio is plotted in Figure 2.11. Both of these results show that these ratios do not change the migration velocity of the bubble at steady state as predicted by Equation (2.8). When the conductivity ratio is unity, the change in the heat capacity ratio does not change the energy equation. Therefore, in Figure 2.11, the test is done with the coefficient of heat conductivity ratio equal to 1/20. In all these four different tests, the time is scaled by the viscous diffusion time scale. The other non-dimensional numbers are the same as for the three dimensional simulation, namely, $Re = 2.5 \times 10^{-3}$, $Ma = 2.5 \times 10^{-3}$ and $Ca = 10^{-3}$.

Finally, we show the results of a much simpler test. A strip of one fluid is laid down in a channel and surrounded by an ambient fluid. A schematic is shown in Figure 2.12. The domain is wall bounded in the vertical direction and periodic in the horizontal direction. There are two free surface at the top and the bottom of the symmetry axis x. The density of the middle layer is equal to the outer one, but its viscosity half of the outer one. We assume that the temperature field is fully developed and increases linearly with x. Since the surface tension is a function of temperature, the only force acting on each interface is the surface tension gradient along the interface, σ_x. The governing equation for this flow can be written as

$$\frac{d}{dy}\left(\mu\frac{du}{dy}\right) + \sigma_x\delta(y) = 0 \tag{2.9}$$

where u is the x component of the velocity. The solution of Equation (2.9) is subject to the no-slip boundary condition on the walls and because of symmetry zero velocity gradient at the symmetry axis. At each interface, the jump in shear stresses is balanced by the surface tension forces. The solution to Equation (2.9) can easily be found as

$$u(y) = \begin{cases} 2\sigma_x d/\mu_o(1 - |y|/d) & \text{if } d/2 < |y| < d \\ \sigma_x d/\mu_o & \text{if } |y| < d/2 \end{cases}$$

By integrating the velocity across the channel, the total mass flux is

$$Q_{ex} = \frac{3}{4}\frac{\sigma_x d^2}{\mu_o}$$

We examine the convergence of Q by computing the total mass flux at different resolution when the flow becomes fully developed, reaching a steady state. Figure 2.13 shows the mass flux normalized by the exact mass flux for different mesh size. The test is done on 1×1 domain with 16×16 grid points, 32×32 grid points, 64×64 grid points and 128×128 grid points. As we increase the resolution, or decrease the mesh size, it is seen that the solution converges well to the exact solution. This further establishes the correctness and the accuracy of the method.

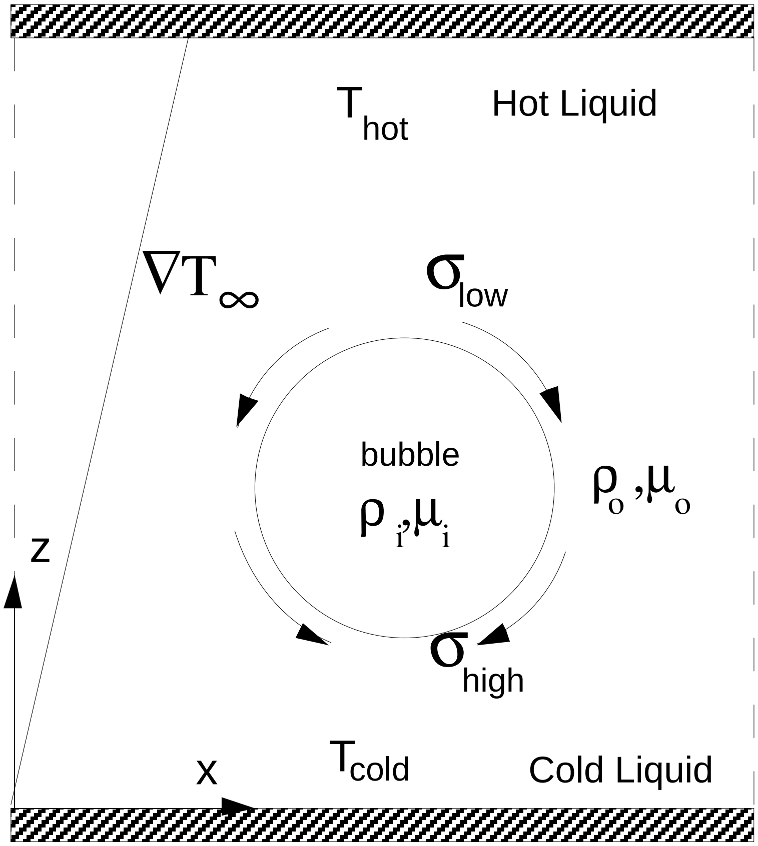

Figure 2.1: The computational setup. The top and bottom wall are no-slip boundaries with constant temperature T_{hot} and T_{cold}. The horizontal boundaries are periodic

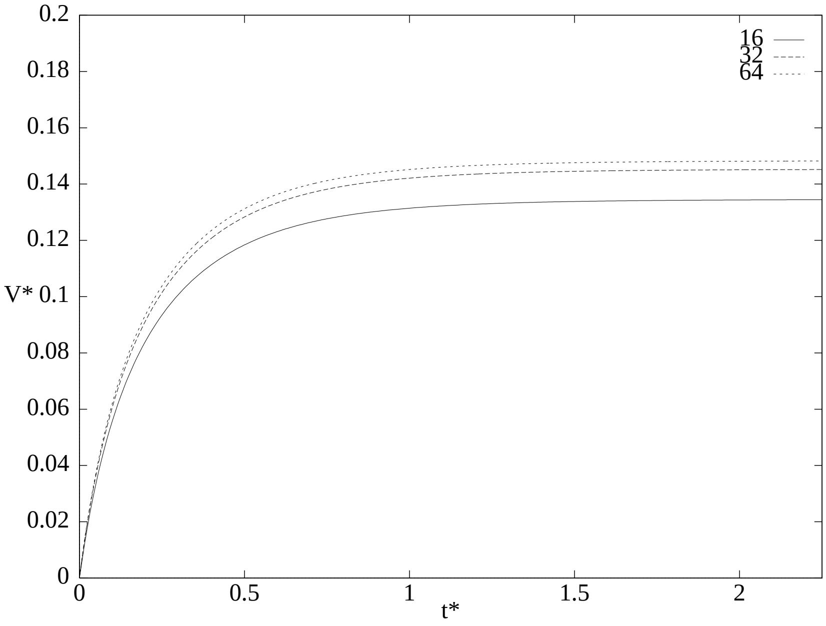

Figure 2.2: Velocity versus time. Convergent test for a single two-dimensional bubble on a computational domain which is 4 bubble radii in each direction.

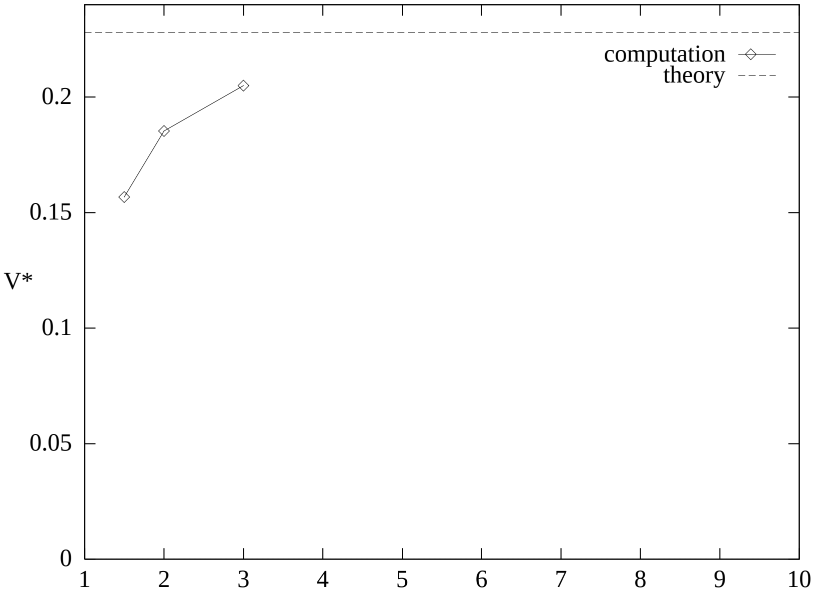

Figure 2.3: Velocity versus box size for a single bubble in 3d. The resolution is 48^3 grid points, 64^3 grid points and $80^2 \times 96$ grid points, respectively.

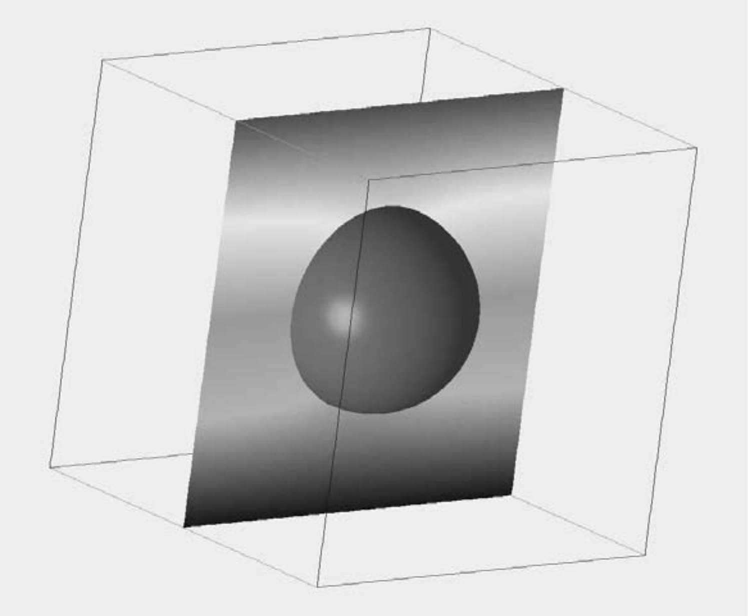

Figure 2.4: The temperature field in the middle plane of the computational domain. The domain is four bubble radii in each direction. The bottom wall is cold and the top wall is hot.

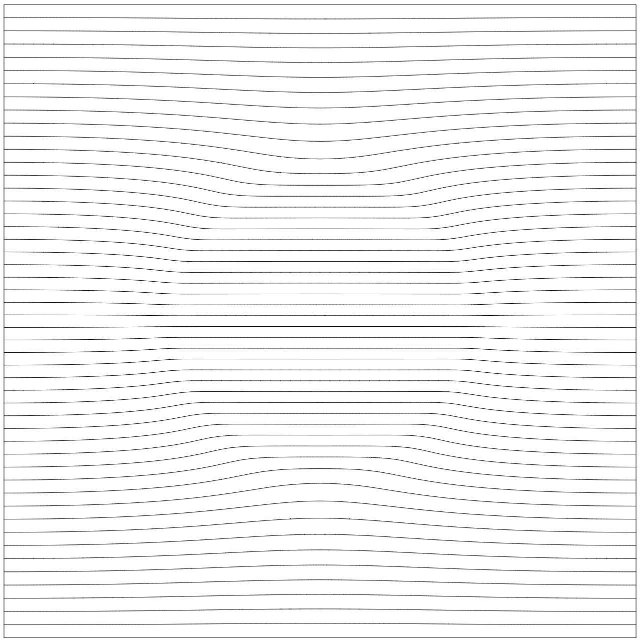

Figure 2.5: Temperature contours in the middle plane of the computational domain. 50 equally spaced contours are shown.

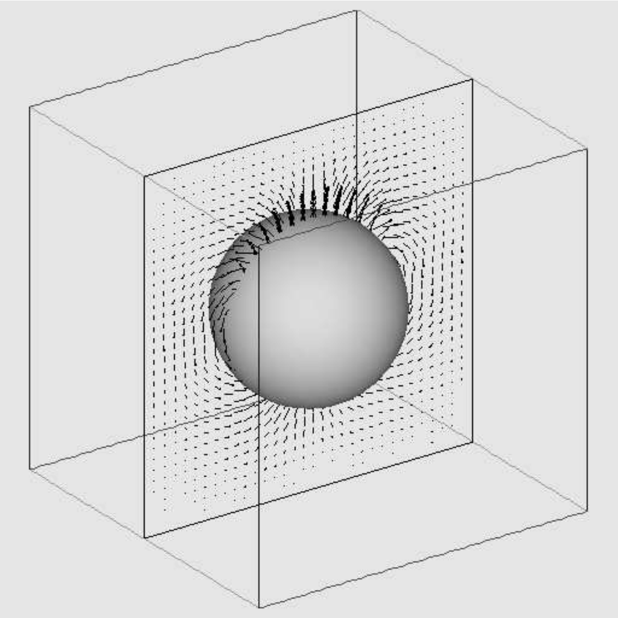

Figure 2.6: The velocity field in the middle plane of the computational domain.

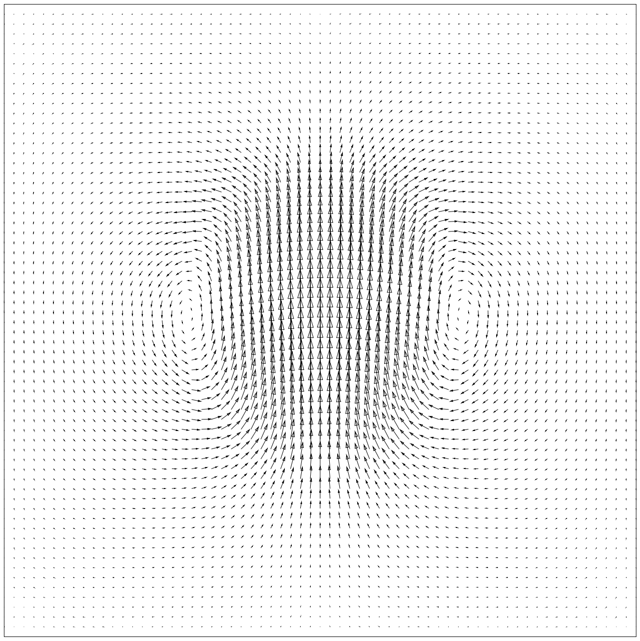

Figure 2.7: Details of the velocity field in the middle plane of the computational domain.

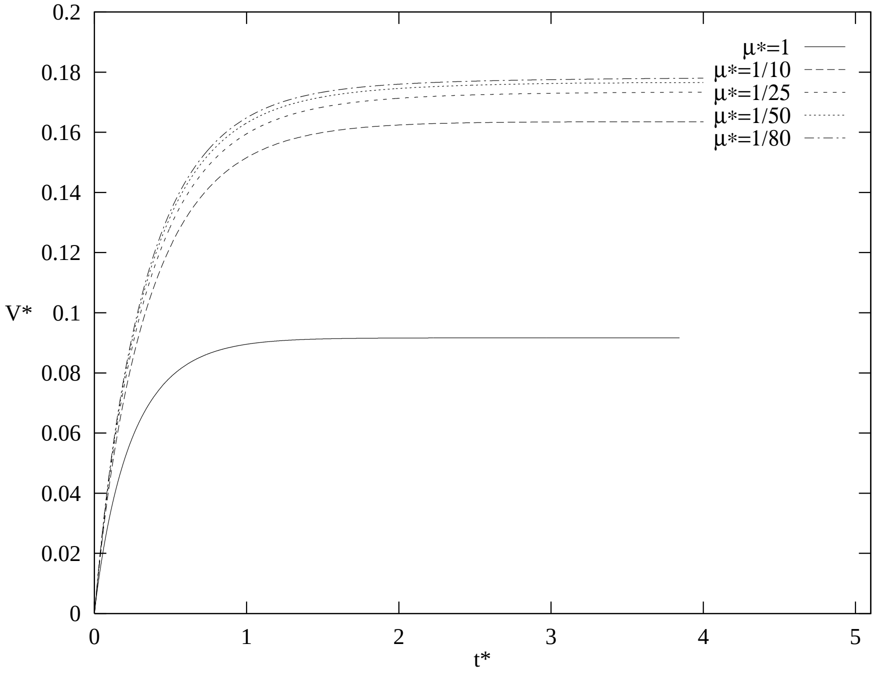

Figure 2.8: Effect of the viscosity ratio on the migration velocity.

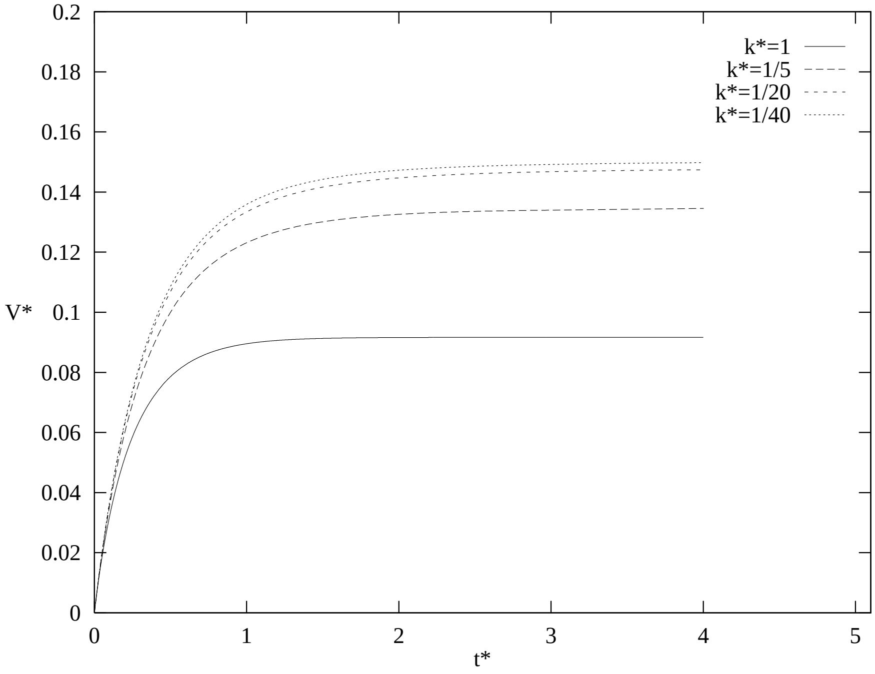

Figure 2.9: Effect of the conductivity ratio on the migration velocity.

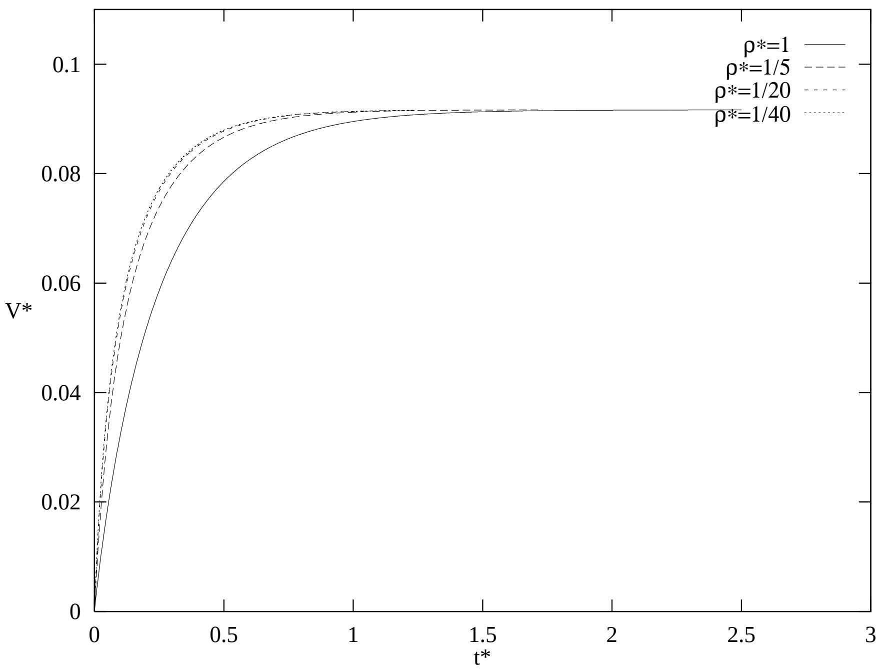

Figure 2.10: Effect of the density ratio on the migration velocity.

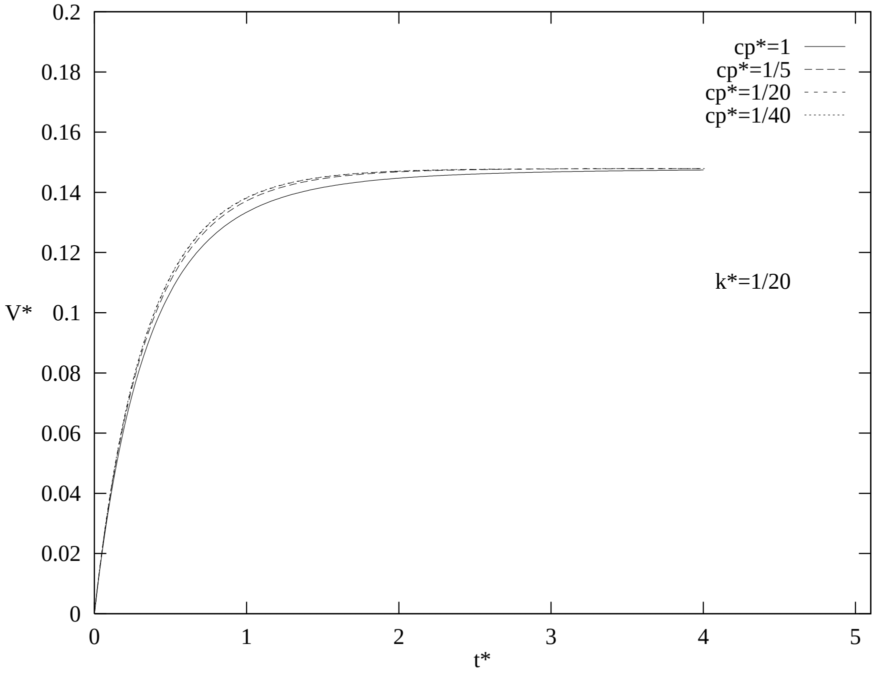

Figure 2.11: Effect of the heat capacity ratio on the migration velocity.

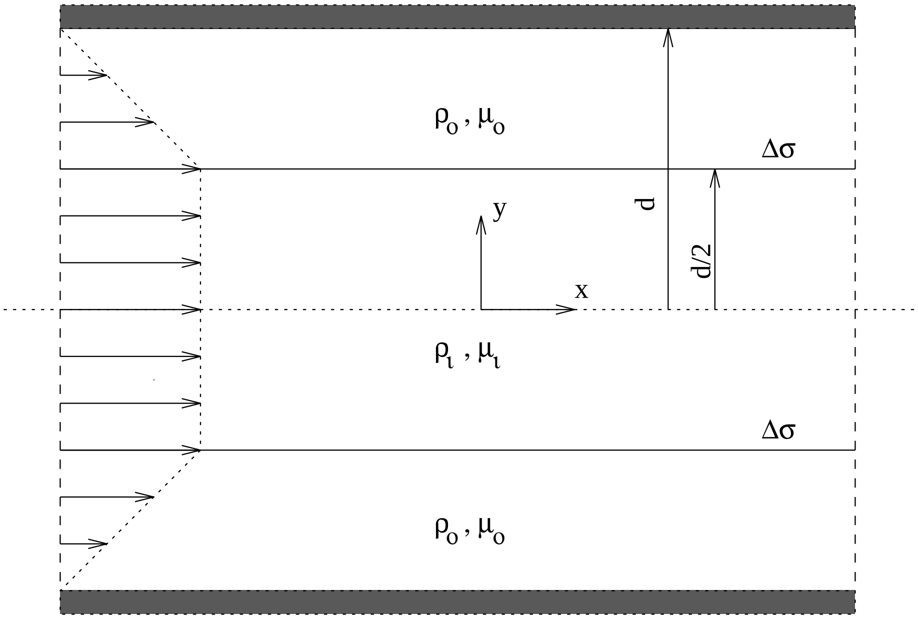

Figure 2.12: Schematic of the third test problem.

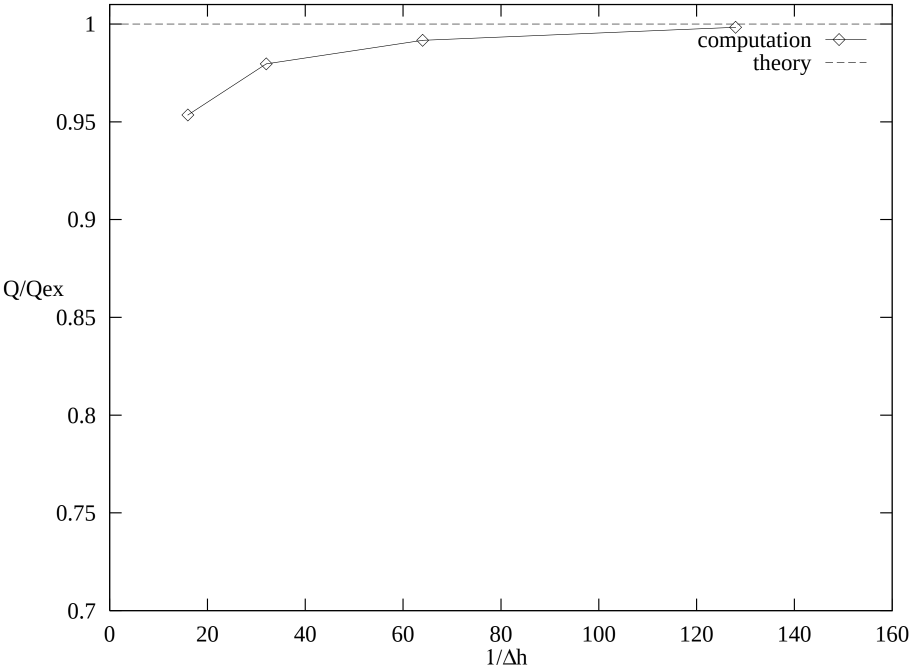

Figure 2.13: Resolution test for the problem in Figure 2.12. Total mass flux scaled by the exact mass flux versus grid resolution.

CHAPTER III

THERMOCAPILLARY INTERACTION OF TWO BUBBLES OR DROPS

3.1 Introduction

In this chapter, we study the interactions between a pair of bubbles or drops, using both two- and three-dimensional simulations. Before discussing these simulations, a convergence test on a single bubble is done, followed by a study of the effect of the various governing parameters on the migration velocity and the deformation of a single bubble. While most of these effects are already known, we nevertheless report them here to gain insight and to prepare the reader for the discussion of more complex results, such as the two-bubble and the multi-bubble simulations. To understand the behavior of a bubble cloud, it is essential to know the basic mechanisms acting between a few bubbles. The two-bubble interaction is the simplest case and has attracted considerable attention in the past as a result.

3.2 Resolution test

Here, we do a resolution test in the region where the non-dimensional numbers are high. We have computed the migration velocity of a single bubble until it reaches a steady state. We have explored the sensitivity of the solution to the grid resolution by simulating a single bubble on a 32×64, 64×128 and 128×256 grid for a domain which extends 4 bubble radii in the x direction and 8 bubble radii in the z direction. This corresponds to 16, 32 and 64 grid points per bubble, respectively. The non-dimensional numbers for this resolution test are: $Re = 5, Ma = 20, Ca = 0.01666$, while the ratio of the physical properties is 0.5 Figure 3.1 shows the velocity field in the top row, isotherms in the middle row and streamlines in a frame moving with the bubble in the bottom row. The resolution increases from left to right. Careful inspection of the last two columns indicates that the differences between these are small. As seen in Figure 3.2(a) and Figure 3.2(b), as the resolution is increased, the terminal velocities and the trajectories converge and we observed that beyond the 64×128 grid the change is negligible, amounts to about 0.6%. The difference between 16 grid points per bubble and 32 grid points per bubble resolution is about 2.1%. Therefore, the 32 grid points per bubble resolution was chosen for most of the simulations presented here in order to save computational resources. Where only qualitative information is required, we can use as few as 16 grid points per bubble, with an error of approximately 3%.

3.3 Thermocapillary migration of a single bubble

Here, we examine the effect of the various controlling parameters on the motion of a single bubble, specifically the rise velocity and the deformation.

To show the effect of the various non-dimensional parameters, the temperature and stream function contours for several different Marangoni numbers are plotted in Figure 3.3. The Marangoni numbers for each column, from left to right, are $1, 10, 20, 40$, and 60. The Reynolds number, $Re = 1$, and the Capillary number, $Ca = 0.0666$, for all these calculations. The ratio of the physical properties, bubble to host fluid, is 0.5. The size of the domain in the horizontal direction is 5 times the bubble radius and the vertical size of the domain is 10 times the bubble radius. Here, we plot the stream function contours in a laboratory fixed frame since the contours in a frame which is moving with the bubble do not show any interesting behavior. In all frames, the bubble has reached an essentially steady state. The major difference is the shape of the temperature contours and the structure of the wake. As the bubbles rise they carry cold fluid from the bottom. This fluid heats up as the bubble moves into warmer fluid and the disturbance in the temperature contours is a reflection of the relative importance of advection over conduction. The disturbance is smallest for the low Marangoni number computation on the left and largest for the high Marangoni number computation on the right. Although the wake is similar in the four last frames, the stagnation point is further away from the bubble in the run on the left. Although we plot 20 equally spaced streamlines close to the bubble, two more streamlines have been added in order to capture the wake region below the dividing streamline. In the first frame, no dividing streamline exists since the Marangoni number in this case is small enough. As a result, convection of energy is negligible and the rise of the bubble is similar to a bubble rising in an unbounded domain, where no dividing streamline exists in the creeping flow regime. The streamlines shown here are nearly identical to those found by Subramanian (1992) for axisymmetric bubbles. Figure 3.4(a) shows the migration velocity versus time. As we increase the Marangoni number, the migration velocity decreases. As a consequence of an increase in the convective transport of energy, the isotherms wrap around the bubble and this causes a reduction in the thermocapillary driving force and hence migration velocity. The bubble remains nearly cylindrical for the computations shown here. Figure 3.4(b) shows that the deformation is decreasing with increasing Marangoni number. However, the magnitude of the deformation is very small. Since the temperature distribution around the bubble is more uniform for higher Marangoni numbers, the change in thermocapillary driving force around the bubble is small. This results in a small deformation of the bubble. Although we terminate these computations before the bubble reaches the top of the domain, we have conducted other calculations where the bubble interacts with the wall and have observed deformations similar to those computed by Ascoli and Leal (1990).

To show the effect of the Reynolds number, we present, in Figure 3.5, the temperature and stream function contours for three different cases. The Reynolds number for each column, from left to right, is $1, 5$, and 10. The Marangoni number, Ma, is 1 and the Capillary number and the ratios of the physical properties are the same as in the previous case. In all three frames, the bubble has reached steady state. Since the Marangoni number is unity, the conduction and convection of energy are equal. As a result, the isotherms are identical. The major difference is the structure of the wake. The streamlines in the high Reynolds number run on the right show that the stagnation point is close to the bubble compared to the run in the middle frame. As in the previous case, two more streamlines are added in order to capture the wake region below the dividing streamline. The first column is the same as the first column in the previous case and was discussed there. The bubble remains nearly cylindrical in this case, as well. The migration velocity decreases with increasing Reynolds number as seen in Figure 3.6(a) although the reduction is small. An inspection of Figure 3.6(b) indicates that the bubble deforms much more, compared to the previous variable Marangoni case in Figure 3.3. This is an interesting result since previous results in the literature indicate that the migration velocity of a bubble increases with increasing Reynolds number for spherical shape bubbles. Therefore, the assumption of a non-deformable bubble is not valid and can cause unphysical predictions. It is the deformed shape of the bubble that leads to a reduction in the migration velocity.

The effect of the Capillary number on the migration velocity and the deformation of the bubble is plotted in Figure 3.7(a) and (b). For these different Capillary number runs, the other non-dimensional numbers are: Reynolds number, $Re = 1$; Marangoni number, $Ma = 10$; and $\mu^* = k^* = \rho^* = {c_p}^* = 0.5$. As noted earlier, zero Capillary number corresponds to a spherical bubble and as the Capillary number increases, the deformation of the bubble increases, as well. Figure 3.7(b) shows that this is indeed the case although the magnitude of the deformation is not big. Figure 3.7(a) shows that the migration velocity of the bubble decreases with increasing Capillary number. This is consistent with the results of Chen and Lee (1992) who also reach similar conclusions.

When the viscosity of the ambient fluid is lower than the bubble viscosity, the viscous shear stresses in the ambient fluid are smaller and most of the work of surface tension forces is done on the fluid inside the bubble. As a result, less fluid flows down around the bubble. Since the motion of the bubble is a reaction to the motion of the ambient fluid, the bubble will migrate with a smaller migration velocity. Figure 3.8(a) shows this behavior clearly. As the viscosity ratio increases, the migration velocity decreases. Here, the other non-dimensional numbers are, $Re = 1$, $Ma = 10$, $Ca = 0.0666$ and $k^* = \rho^* = c_p^* = 0.5$.

Figure 3.8(b) shows the effect of the ratio of the heat conductivity coefficients on the migration velocity. The migration velocity of the bubble is higher when the temperature gradient across the bubble is high. As a bubble in a temperature gradient moves toward the hot region, the north pole of the bubble absorbs heat and the south pole gives off heat to the cold ambient fluid. When the heat conductivity of the bubble is negligible, heat cannot enter at north pole of the bubble, nor leave to the ambient fluid at the south pole. This results in a temperature field where the isotherms are perpendicular to the bubble surface, showing no heat transfer to the bubble. As a result, the temperature gradient across the bubble's south and north poles is high, and consequently the migration velocity is high. Here the non-dimensional numbers are, $Re = 1$, $Ma = 10$, $Ca = 0.0666$ and $\mu^* = \rho^* = c_p^* = 0.5$.

Since the density of a drop is higher than that of the ambient fluid it should be expected that the drop will accelerate more slowly than a gas bubble. Figure 3.9(a) shows this slower acceleration when the density ratio is 10. Furthermore, with increasing density of the bubble phase, the heat convection inside the drop will increase. The isotherms will be more curved toward the hot portion of the drop surface. Because of this, a more uniform temperature field will be present inside the drop. Consequently, the migration velocity of the drop decreases with increasing drop density. This behavior is seen in Figure 3.9(a). The same argument also holds for the heat capacity ratio. The reduction of the drop migration velocity with increasing heat capacity is shown in Figure 3.9(b). Here the non-dimensional numbers are, $Re = 1$, $Ma = 10$, $Ca = 0.0666$ and for the density ratio effect $\mu^* = k^* = c_p^* = 0.5$ and for the heat capacity $\mu^* = \rho^* = k^* = 0.5$.

3.4 Effect of initial position on the interaction of two bubbles

After obtaining some insight about the thermocapillary migration of a single bubble, we move to the interaction of two bubbles. To understand the effect of the initial orientation of the bubbles on the evolution, we vary the gap between the bubbles and their angular position with respect to the initial temperature gradient. In Figure 3.10(a), (b) and (c), the angle between the x axis and a line connecting the center of the bubbles is $\pi/8, \pi/4$ and $3\pi/8$, respectively. The angular orientation of the bubbles in the other frames, $(d), (e), (f)$ is the same. In the first three frames, the gap between the bubbles, center to center, is 2.5 times the bubble radius. In the last three frames, this distance is three bubble radii. The computations was done on a domain which is 8 bubble radii wide in x and 16 bubble radii high in z. The resolution used here is 128×256 grid points. The non-dimensional numbers for all the cases are: $Re = 10, Ma = 10, Ca = 0.041666$ while the ratio of the physical properties is equal to 0.5.

We report the results of these simulations in Figure 3.11 and Figure 3.12. An inspection of Figure 3.11(a) and (b) shows that the bubbles close the gap between themselves in the vertical direction while placing themselves side by side, almost equispaced across the channel. The last case is, however, an exception. Since the gap is large and the bubbles are almost oriented in tandem in that case, it takes a larger distance to close the gap vertically and the bubbles reach to the top wall before lining up across the channel. Nevertheless, the trends suggest that they will behave similar to the other cases, if given a longer box. Figure 3.12 shows the migration velocity difference between the bubble on the right and the bubble on left. This figure also shows that as the bubbles migrate in the vertical direction, they catch up with each other. When the bubbles reach a steady state, they migrate with the same velocity, side by side.

3.5 Two dimensional simulations of two bubbles or drops

While the primary goal of this study is to understand the basic physics involving bubble pairs in a real physical situation, much information can be gained by two dimensional simulations, even though they must be regarded as only a step toward fully three dimensional simulations. In this section, we discuss the interactions between two-dimensional bubbles and drops.

First, we explore the motion of gas bubbles. The physical properties of a gas bubble are small compared to the ambient fluid. Thus, the viscosity, the density, the coefficients of heat conductivity and the heat capacity are much smaller in the gas than in the fluid phase. In view of the findings of Chapter II, and the earlier sections of this chapter, where we examined the effect of the physical parameters on the bubble's migration velocity, we choose the ratio of physical properties to be 1/25, which is low enough to simulate the motion of a gas bubble. We take the Capillary number as fixed at $Ca = 0.04166$ in all simulations done in this section, but use various Reynolds and Marangoni numbers. The resolution for these runs is 128×256 grid points and the computational domain is 8 bubble radii wide in x and 16 bubble radii high in the z direction. The bubbles are released close to each other and the bubble on the right is ahead of the other bubble initially. The bubble on the left is at $x/a = 2.9$ and $z/a = 4$, and the one on the right is at $x/a = 5.1$ and $z/a = 5.8$. Here, both the Reynolds and the Marangoni numbers are 40; therefore convective transport of energy and momentum are higher than viscous and thermal diffusion. Figure 3.13 shows the velocity field, and the corresponding isotherms are plotted in Figure 3.14 at different times, showing the evolution.

As the bubbles rise, the bubble on the left first catches up with the bubble on the right. It draws hot fluid down its side and as the bubble on the right rises, some of this fluid is drawn into its wake, thereby reducing slightly the temperature increase across the bubble on the right and hence its velocity. After the bubbles move slightly closer together, the fluid in the narrow gap between the bubbles is pushed down more than in the wider gap, since the contribution of each bubble to the velocity field adds in this region. This is seen in the second frame of the velocity field. Hence, more hot fluid is drawn into the narrow gap between the bubbles than into the wide one. As a result, the bubbles attract each other. After they collide, they bounce back and the bubble on the left pushes the bubble on the right to the right. Since it catches up with a large velocity, it hits the bubble on the right and causes it to rotate clockwise. As seen in Figure 3.15(a), the bubble on the left has a higher migration velocity. After the collision, this bubble still moves faster upward than the other one and the bubble on the right is caught in the wake of the left one which is now ahead of it. Because of this, we see an interesting phenomena here, as well as in Figure 3.16; namely, that the bubble being caught in the wake of the other one migrates against the temperature gradient. From the temperature field in Figure 3.14, it is seen that when the bubbles are close, the hot ambient fluid flows down in the wide gap, satisfying the conservation of mass. Since the bubbles migrate toward the hot region, the bubbles move apart. This is seen in the fourth frame of Figure 3.14. Later, the bubble on the right moves far away from the bubble on the left and crosses into the next periodic box while still accelerating to reach its steady state migration velocity. Since the boundary conditions are periodic in x, we see the bubble reentering from the left side of the computational box. This time the bubbles collide horizontally and bounce back. The collision is not as strong as the previous one, as is seen from the trajectories in Figure 3.16. After the second collision, the bubbles move away from each other and migrate toward the hot wall. We have stopped the simulation before the bubbles hit the wall. If the periodic box is wide enough, it can be easily concluded that after the first collision, the bubbles would separate and migrate toward the hot wall almost independent of each other, similar to a single bubble migration. It should also be noted that the temperature field is disturbed much more by the circulating flow in the wake region of the bubbles than in the field ahead of them.

In the last frame of Figure 3.14, the temperature gradient across each bubble clearly shows its direction of motion. Figure 3.15(d) shows that the bubbles, by closing the gap in vertical direction, eventually move side by side. The internal circulation plot in Figure 3.15(b) indicates that the direction of motion of the bubbles is consistent with the sign of the internal circulation. From the elementary theory of lift, the bubble would move to the left in the configuration presented when the internal circulation is positive and it is in a uniform incoming velocity field. The internal circulation is calculated by $\oint \mathbf{u}_s \cdot d\mathbf{s}$ along the interface. When the bubbles collide, Figure 3.15(c) shows that the deformation increases with each collision.

We have repeated these computations for various Re and Ma numbers and studied the effect of these numbers on the separation distance and the migration velocity difference between the bubbles. We show these quantities in Figure 3.17. Although we attempted to simulate the $Re = 60, Ma = 20$ case, this was not possible because the pressure solution did not converge. The different Re and Ma number cases in Figure 3.17 indicate that the vertical alignment of the bubbles is unstable and bubbles eventually come side by side to form a more stable layer. When the bubbles migrate, they overtake each other but eventually the oscillation in the vertical gap dies out. The bubbles try to space themselves equally across the channel (note that the computational box is periodic in horizontal direction). The first case, $Re = 10, Ma = 10$ exhibits different behavior from the rest. In this case, the bubbles close the vertical gap much faster and reach to the same migration velocity in a shorter time. The most significant difference is seen in the horizontal spacing of the bubbles in Figure 3.17. The bubbles come side by side, migrate together for a long time and move apart only very slightly, retaining the initial separation. It is likely that these bubbles would coalescence if the interface were allowed to rupture but here we do not allow that to happen.

We then move to the interactions of two drops. The density of a drop is higher than that of the ambient fluid and we choose a density ratio of 10. Other ratios of the physical properties are the same as for the gas bubbles, namely $\mu^* = k^* = c_p^* = 1/25$. The Capillary number, the resolution, as well as the computational domain size are also the same as in the previous case. The drops are released close to each other with an arbitrary orientation with respect to the temperature gradient. The initial positions of the drops are the same as in the previous case in Figure 3.13. We also do these simulations for various Reynolds and Marangoni numbers. Similar to the gas bubbles, we report one of these cases where both the Reynolds and the Marangoni numbers are 40.

Figure 3.18 and Figure 3.19 show the velocity field and the isotherms, respectively, at different times. Some differences are easily seen in the interaction of drops as compared with the gas bubbles. Inspection of the velocity field shows that the interaction takes place from the beginning to the end in the computational box considered. The drops, also, do not cross the periodic boundaries. The velocity field plot shows strong velocities inside and outside of the drops. Especially, strong recirculating zones in the wake of the drops at later times are visible. It is also seen that the drops deform much more than the gas bubbles. The deformation occurs in such a way that the drops elongate in the flow direction. The isotherms show another major difference, inside the drops. Due to the convective transport of energy inside the drops, the temperature field inside the drops is very contorted. The isotherms wrap along the inside surface of the drop, causing it to slow down. The high velocity in the wake of the drops disturbs the temperature field considerably in this region. While the thermal wake region extends all the way to the bottom wall, the velocity and temperature field ahead of the drops remain almost unaffected due to small effect of conduction.

As seen in the velocity and the isotherm plots, the hot ambient fluid flows through the narrow gap between the drops, since each drop pushes the ambient fluid in the same direction in this region. As a result of this behavior, the drops move closer to each other. Similar behavior is also seen in the trajectories in Figure 3.21. When the drops collide, the drop on the left bounces back and slows down. This collision causes the drop on the right to speed up sharply, although it was initially moving slower than the drop on the left. The drop on the left feels the effect of the impact and slows down quickly. After the collision, both drops accelerate and migrate upward as seen in frames four to six of the velocity field. However, the drop on the left accelerates faster and catches up with the other drop in the sixth frame. Until then, unlike the interactions between gas bubbles, the drops do not come side by side, but migrate to a position such that the drop on the right is ahead of the drop on the left, but slightly on the left side, similar to their initial position. This is the major difference between the behavior of drops and the gas bubbles. Right before hitting the upper wall, the drops collide once more. The collision at this time is weak, causing small acceleration of the drop on the right and deceleration of the drop on the left. In the last time frame of the plot of the temperature field, since the drop on the right is very close to the wall, the drop on the left slides to the left so that it reaches the upper wall. Figure 3.20 shows a more quantitative description of this simulation where the migration velocity, internal circulation, deformation and separation distance are plotted. After each collision, the change in internal circulation and deformation is obvious. The vertical and the horizontal separation distance between the drops is clear in Figure 3.20(d). Although the vertical distance decreases in the early stages of the interaction, where the drops attract each other, later on this gap increases, showing the trend explained above. Because of this orientation of the drops, the horizontal gap obviously get smaller.

We have done simulations of drops for various Re and Ma numbers and have studied the effect of these numbers on the vertical and horizontal separation distance between them as a function of time. We show these quantities in Figure 3.22. The different Re and Ma number cases in Figure 3.22 clearly show that the behavior seen in the gas bubbles simulations does not apply to drops. When $Re = 60$ and $Ma = 20$, it seen that the drops close the vertical gap and move away from each other in the horizontal direction. Since they separate in the horizontal direction, their influence on each other becomes minimal. The other cases behave differently. When the Reynolds and the Marangoni numbers increase equally, there is a transient behavior seen in that plot. When both Re and Ma are 10, the drop on the left takes over and moves ahead of the drop on the right in the late stages of the simulations. The drops also separate horizontally. When Re and Ma are increased to 20, the drop on the left catches up with the drop on the right, but eventually the drop on the left takes over, just before both drops hit the top wall. They also separate horizontally but less than in the previous case. Further increase of Re and Ma to 40 shows a different picture. The drop on the right always stays ahead of the other drop and, most importantly, the vertical gap between them increases while the horizontal gap decreases. This is the case that we discussed earlier. In the final case, where Re and Ma are increased to 60, this behavior continues. This time, the drop on the right is well ahead of the other one while the horizontal gap is reduced significantly and these drops are almost in tandem when they reach the upper wall.

Next, we examine an intermediate case with bubbles where the physical properties of the bubble phase are half those of the ambient fluid. We also conduct these simulations for different Re and Ma numbers. The Capillary number, the initial position of the bubbles, the domain size and the resolution is the same as for the gas bubbles case in Figures 3.13 - 3.16. The velocity field, Figure 3.23, is similar to the velocity field of the gas bubbles in Figure 3.13, showing the recirculation zones in the wake of the bubbles. Figure 3.24 shows the temperature contours at different times. As the bubbles rise, the bubble on the left first catches up with the bubble on the right. As seen for the gas bubbles, it draws hot fluid down its side and as the bubble on the right rises, some of this fluid is drawn into its wake, thereby reducing slightly the temperature increase across it and hence its velocity. While the bubbles are moving side by side, close to each other, they migrate like one big bubble. Since the ambient fluid can no longer flow between them, it flows down near the side of the periodic box. Bubbles move toward the hot regions and separate as they continue to migrate to the upper wall. Since the bubble on the left pushes the bubble on the right to the side, and also due to the temperature gradient, the bubble on the right slides to the side, reappearing from the left side of the periodic box. From then on, the bubbles migrate side by side, almost equispaced across the channel. This is due to the fact that once the bubbles are side by side, and moving upward, the outer fluid has to flow down between them to satisfy continuity and when the spacing between the bubbles is uneven there is greater flow through the larger spacings. Since the downward moving fluid is hotter, the isotherms are pushed farther down where there is a large space between the bubbles than when the space is small. This is very clear in the second frame. Since the bubbles move from colder parts of the domain to the hotter ones, this leads to a lateral motion (in addition to the upward motion) where the small spaces become larger and the large spaces become smaller until the bubbles have arranged themselves in a horizontal array with equal spaces between them.

Figure 3.25 shows the migration velocity, the internal circulation, the deformation and the separation distance for the run in Figures 3.23 and 3.23. The initial acceleration is similar to the one bubble case, both bubbles accelerate rapidly, reach a large velocity and then slow down. The bubble on the left, that is closer to the bottom of the box, reaches a higher initial velocity and slows down more slowly than the one on the right. It is seen from this plot that the bubble on the left migrates at an almost steady state velocity in the last half of the interaction process. The deformation decreases in that period, too. The trajectories of the bubbles are plotted in Figure 3.26.

Investigations for different Re and Ma numbers shown in Figure 3.27 exhibit similar behavior as the gas bubbles considered in Figure 3.13. In all cases the bubbles close the vertical gap between them. As the non-dimensional numbers increase, the interaction becomes stronger and the bubble on the right crosses over to the next periodic box. Since the system is periodic horizontally, the bubble reenters through the other side of the box. Therefore, while the horizontal separation is calculated between the bubble on the right and the bubble on the left, it should actually be measured between the bubble on the left and the bubble which reenters from the left side of the domain once the one on the right crosses to the next periodic box. Thus, the results in Figure 3.27(b) show that two bubbles space themselves across the channel as equispaced as they can.

We have also investigated another case where the density and the heat capacity ratio of the bubble phase is half that of ambient fluid, but viscosity and heat conductivity ratio is 1/25, similar to Figure 3.13. Although we also explored several Reynolds and Marangoni numbers, the only qualitative difference we found is the structure of the temperature field inside the bubbles. The convection of energy inside the bubble is high and the isotherms are similar to the isotherms inside the drops while the temperature field in the ambient fluid is not much different from Figure 3.24.

3.6 Three-dimensional simulations of two bubbles

After gaining some insight into the interactions of two bubbles from two-dimensional simulations, we explore the interaction of two bubbles by fully three-dimensional simulations in this section.

The ratios of the physical properties are 0.5, same as for the two dimensional cases discussed at the end of Section 3.5. The Capillary number is also the same. The resolution for these runs is $64 \times 32 \times 128$ grid points in a $x/a = 5.71$, $y/a = 2.86$, $z/a = 11.43$ computational box. The bubbles are close to each other and are perturbed so that the bubble on the right is ahead of the other one. The location of the left bubble is $x_l/a = 1.71$, $z_l/a = 2.85$ and that of the right bubble is $x_r/a = 4$, $z_r/a = 3.43$. They are placed in the middle cross sectional plane in the y direction. The thermal gradient is such that temperature increases toward the top hot wall.

We report two different cases. For the first one, $Re = 20$ and $Ma = 60$. The bubbles are shown in Figure 3.28, along with the velocity and the temperature field in the middle cross sectional plane. A more detail description of the velocity field and isotherms in that plane are plotted at different times in Figure 3.29 and Figure 3.30, respectively. The first frame in Figure 3.28 shows the starting motion of the bubbles where the velocity field is weak. In the second frame the velocity is much stronger than in the other frames. This is the time when the bubbles attain their highest migration velocity. The interaction follows a similar pattern as was seen in the two dimensional simulations. Since the ambient fluid between the bubbles is pushed down, as is seen from the velocity field, the bubble on the left is attracted to the bubble on the right. The curved isotherms in Figure 3.30 show the relative effect of the convective transport of energy. Since the Marangoni number is high, the convection of energy is large. Both bubbles accelerate very fast, attain a high migration velocity and then slow down. When the bubble on the left moves to the right, it pushes the other bubble to the side. As the bubbles get close to each other, the hot ambient fluid flows down along the sides of the computational box, thereby increasing the temperature in that region. This is clearly seen in the third frame of the isotherms in Figure 3.30. This shape of the isotherms is also determined by the fact that the bubbles carry cold fluid with them. As a result, they move apart. Since the bubble on the left has a higher velocity, it catches up with the other one. As they slow down to a steady migration velocity, the velocity difference between them decreases, as is seen in Figure 3.31(d). Figure 3.31 gives a more quantitative description of this simulation. The migration velocity, vertical position, separation distance, and velocity difference are plotted versus time. Figure 3.31 as well as Figure 3.32, where the trajectories are shown, show that when the bubbles reach a steady state, they are almost side by side and equispaced horizontally. The behavior of the bubbles presented here confirms the predictions of the two-dimensional simulations discussed in Section 3.5.

Comparison of two- and three-dimensional simulations reveals that the disturbances of the velocity and the temperature field decay in the three-dimensional simulations at a much faster rate than in the two dimensional simulations as we go away from the bubbles. See, for example, the isotherms in Figure 3.30. Although weak, recirculating zones seen in two-dimensional simulations are also observed in the three-dimensional simulations and are visible in the middle frames of the velocity field.

After examining the interactions between two bubbles in a parameter range where convective transport of energy is higher than convective transport of momentum, we move to the second case where $Re = 60$ and $Ma = 20$. All other parameters are the same as in the previous case. Here, we place the bubbles in such a way that they are disturbed more in the vertical direction than in the previous case. Specifically, the left bubble is at $x_l/a = 2.14$ and $z_l/a = 2$ and the right bubble is at $x_r/a = 3.57$ and $z_r/a = 3.85$. Both are placed in the middle cross sectional plane in the y direction. Figure 3.33 shows the evolution of this case. Both the velocity field and the temperature field are plotted in the middle cross sectional plane. The velocity field in that plane is also while in Figure 3.34 and Figure 3.35 shows the isotherms in the same plane. It is easily seen that there are some differences in the velocity field compared with the previous case. Although the first frame of both Figure 3.28 and Figure 3.33 are similar, the rest of the evolution is different and the velocity does not decrease here. An inspection of Figure 3.36, where a more quantitative description of this simulation is presented, shows that although the bubbles slow down, the rate of decrease is small. After reaching an initial high velocity, they migrate at this high velocity until they reach the upper wall. Although the velocity decreases slightly at the end of the simulations, the bubbles do not have enough distance to slow down to a steady migration velocity. This behavior is due to the higher Reynolds number and is similar to what was seen in the two-dimensional, two-bubble interaction. Nevertheless, Figure 3.36 shows that as in the previous case, the bubbles strive to close the vertical gap while moving apart in the horizontal direction. From the trajectories in Figure 3.37 it is seen that the bubble on the left is ahead and moves straight up while the other one slides to the side. This is due to the temperature field which is different than the previous case, see Figure 3.37. The bubble on the left does not feel the effect of the other bubble to any significant degree. But, since the bubble on the left migrates straight ahead faster, it pushes the other bubble to the side which is actually blocking the way of the other bubble. The forth and the fifth frames of Figure 3.35 show that the ambient fluid on the right side of the bubble on the right is hotter than on the other side. Therefore, the bubble should move to the right as it does, because bubbles move in the direction of a higher temperature.

Since the convective transport of energy is not as high as in the previous case, the isotherms do not curve as much. While the disturbances of the temperature field decay as fast as the previous case, the velocity fields differ. Once the recirculation zones form, they are present until the end of the simulation, as seen in Figure 3.34.

We have also computed similar simulations for different Reynolds and Marangoni numbers. Figure 3.38, where the vertical and the horizontal separation distance between the bubbles are shown, summarizes the results of these simulations. In all these different Re and Ma number cases, it is seen that the bubbles strive to close the vertical gap while moving apart horizontally.

3.7 Conclusion

The major finding reported here is the tendency of the bubbles to line up, side by side, perpendicular to the temperature gradient. While this behavior appears to be similar to what is found for spheres and cylinders in fluidized beds, where rows of spheres align themselves into a string perpendicular to the flow, the mechanism here is different. For solid spheres the reason is the low pressure region at the "waist" which attracts other particles. In the simulations carried out here the bubbles actually repel each other, since cold fluid is more easily carried with the bubbles in the narrow gaps between them than in bigger gaps, and the bubbles generally move away from cold regions. Thus, while the bubbles line up across the channel they tend to maximize the distance between adjacent bubbles. This formation of bubble layers could be of considerable significance for material processing in microgravity where layers like these might affect the bulk properties of solidified material. Drops, on the other hand, behave somewhat differently. In the low Re and Ma number region they behave similar to bubbles, but they tend to line up in tandem in most of the simulations presented here when both Re and Ma are high. Drops also deform much more than bubbles along the direction of the temperature gradient.

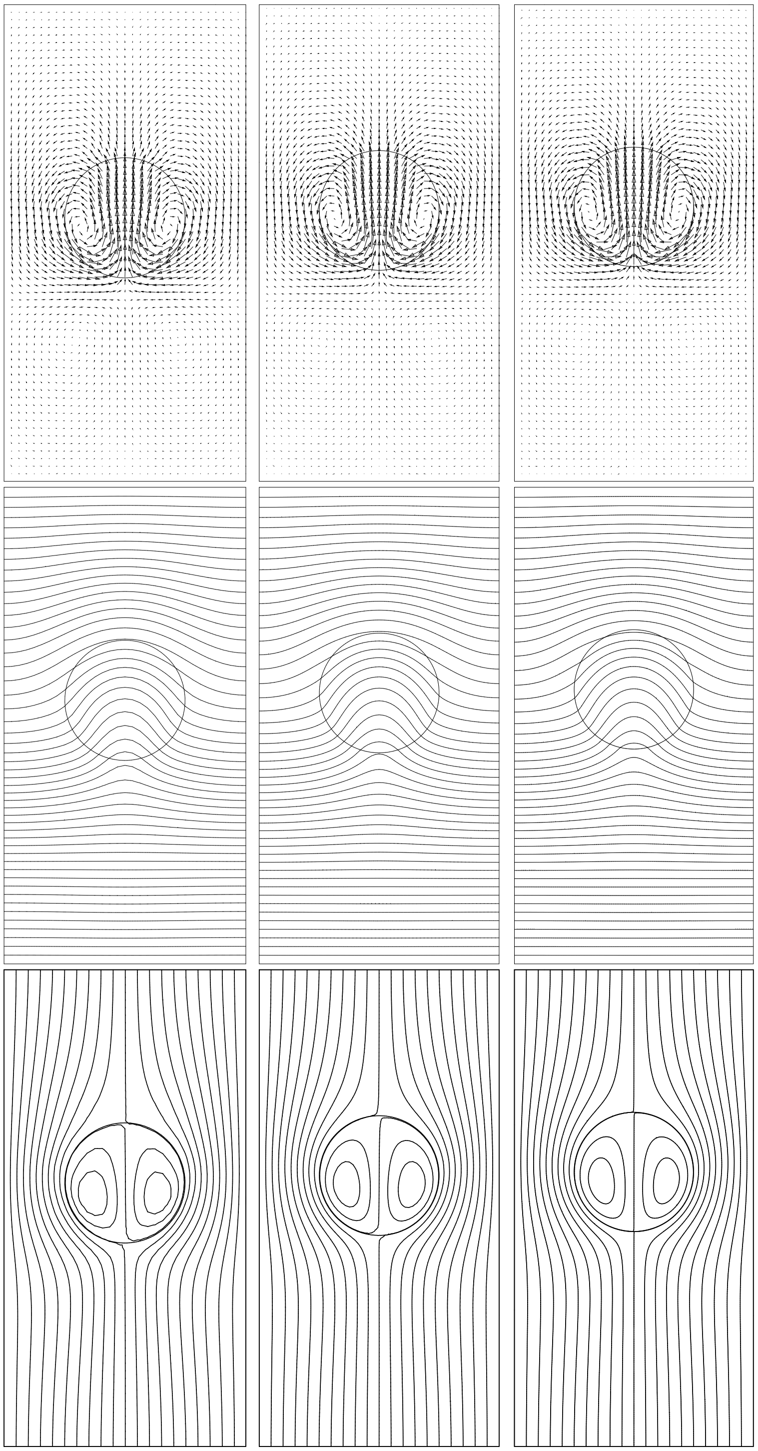

Figure 3.1: Velocity field (top), isotherms (middle) and streamlines (bottom) of a single bubble rising at steady state. 32 × 64 grid points of the velocity field, 50 equally spaced isotherms and 21 equally spaced streamlines in a frame moving with the bubble are shown. First column is a 32 × 64 grid, second column is for a 64 × 128 grid and third column is for a 128 × 256 grid.

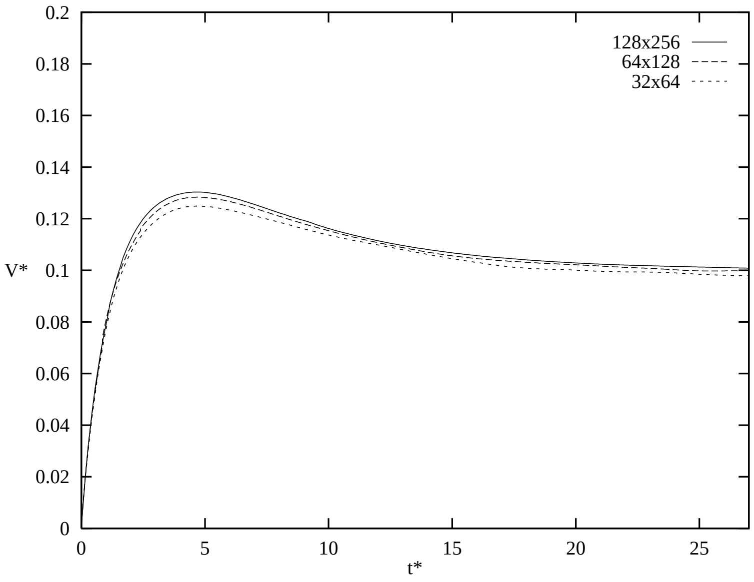

(a) Migration velocity

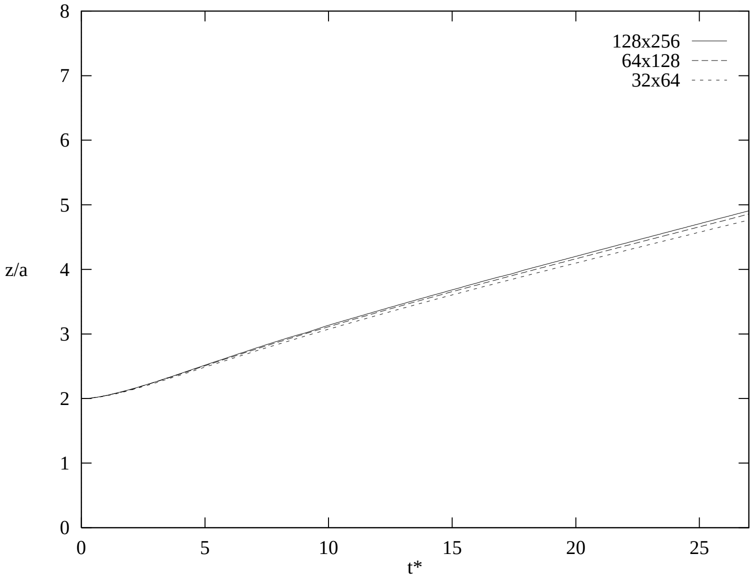

(b) Trajectories

Figure 3.2: Resolution test for a single bubble. (a) Migration velocity versus time (b) z component of the trajectories versus time.

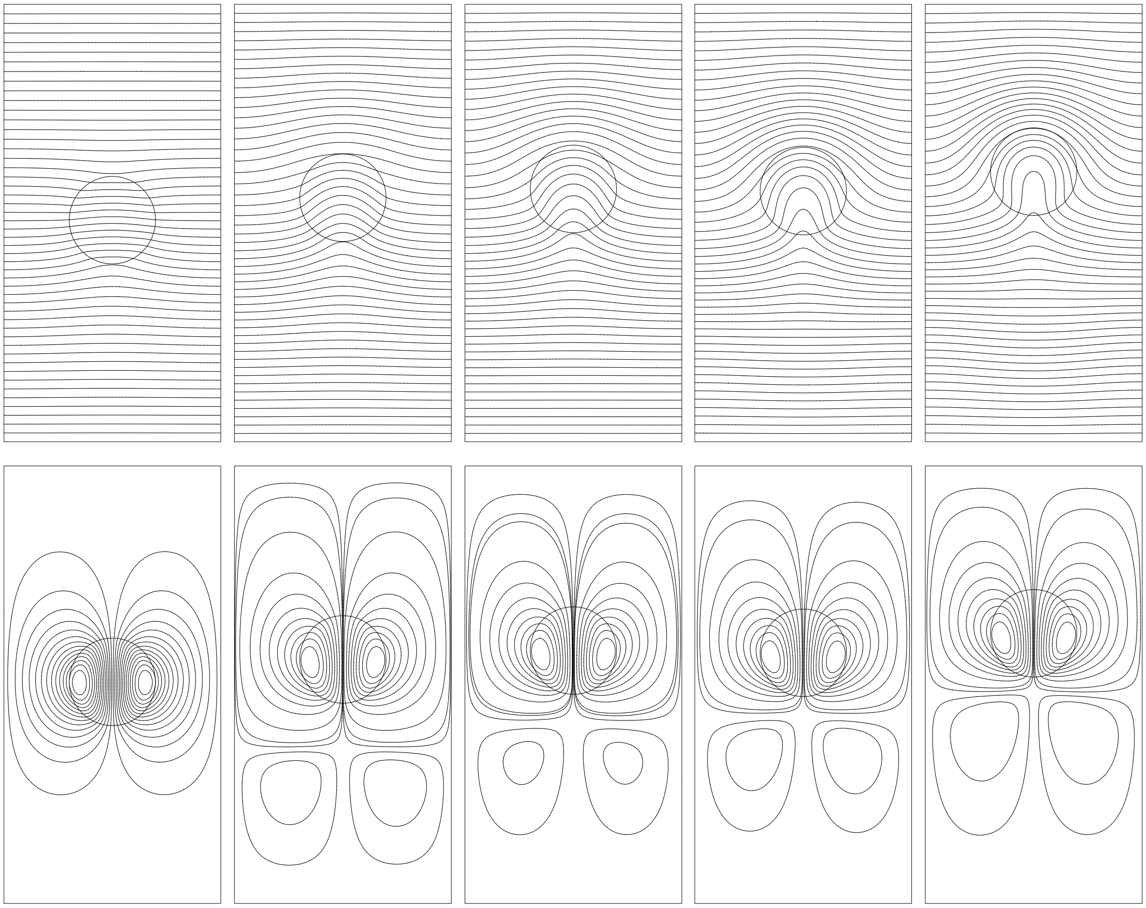

Figure 3.3: Isotherms (top) and streamlines (bottom) of a single bubble migrating at steady state for different Marangoni number. 50 equally spaced isotherms and 20 equally spaced streamlines are shown. Marangoni number for each column from left to right is 1, 10, 20, 40, 60. Here, $Re = 1$ and $Ca = 0.06666$.

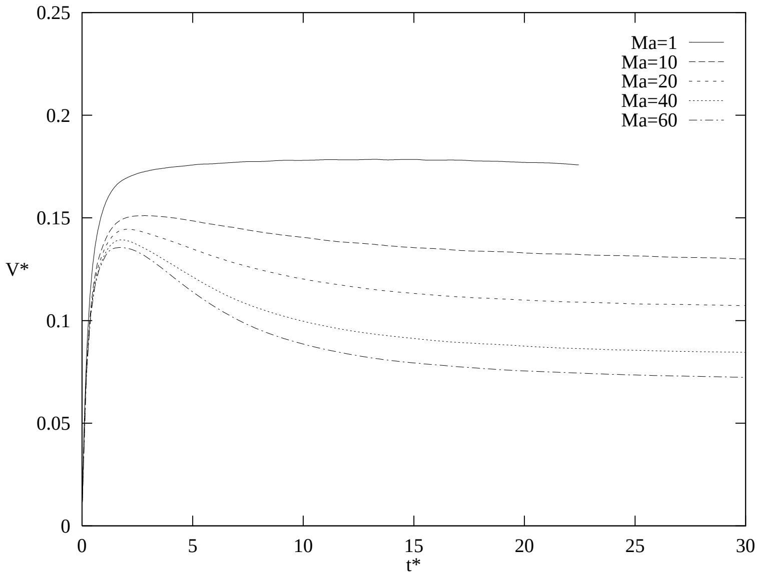

(a) Migration velocity

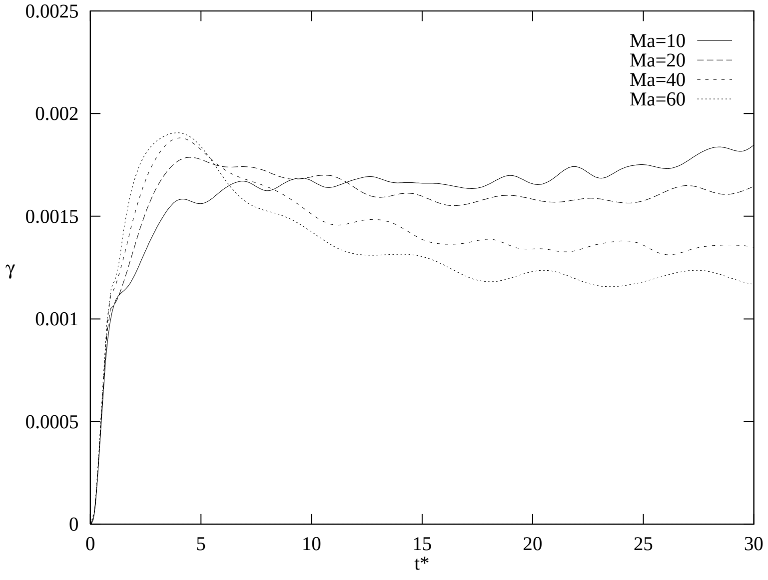

(b) Deformation

Figure 3.4: Effect of Marangoni number on the migration velocity and the deformation of a single bubble.(*a*) Migration velocity versus time (*b*) Deformation versus time.

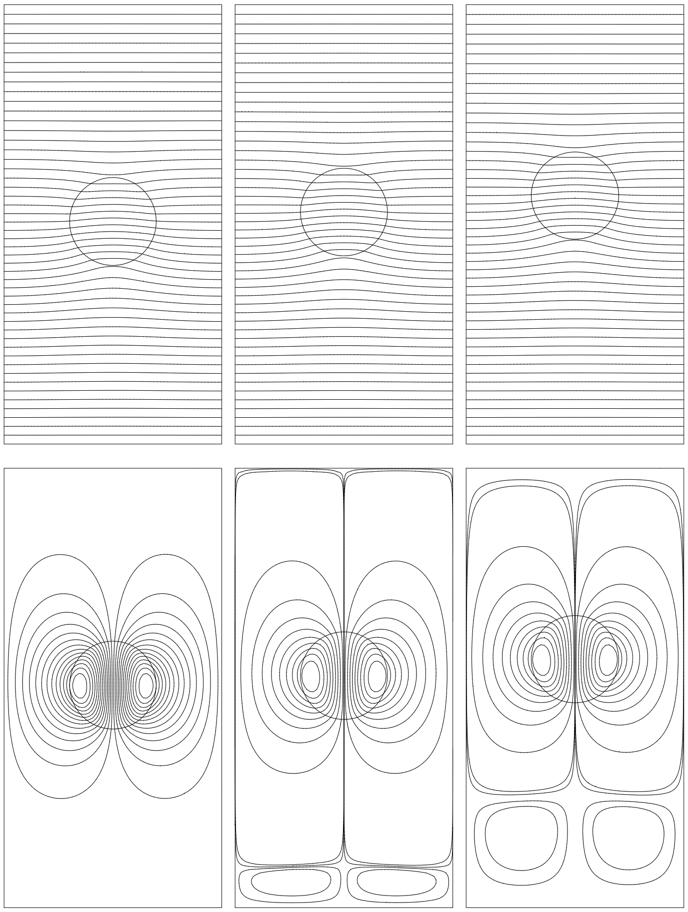

Figure 3.5: Isotherms (top) and streamlines (bottom) of a single bubble migrating at steady state for different Reynolds number. 50 equally spaced isotherms and 20 equally spaced streamlines are shown. Reynolds number for each column from left to right is $1, 5, 10$. Here, $Ma = 1$ and $Ca = 0.06666$ and the resolution is 64×128 grid points.

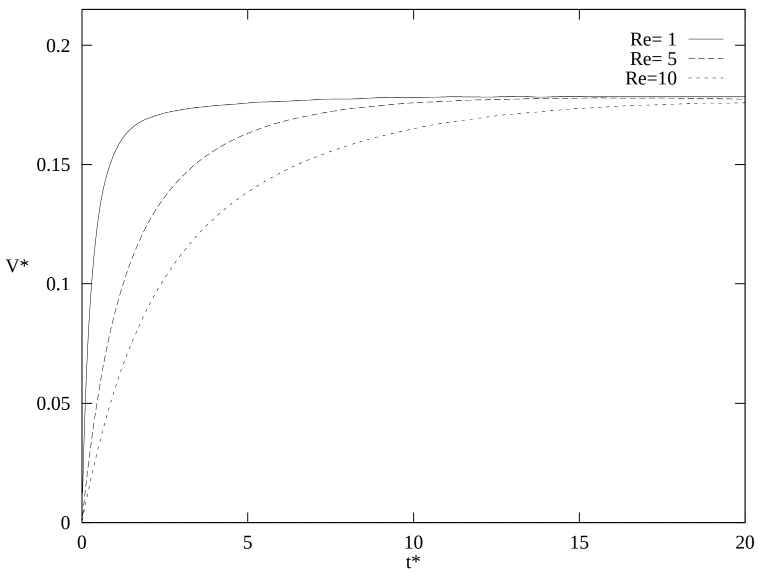

(a) Migration velocity

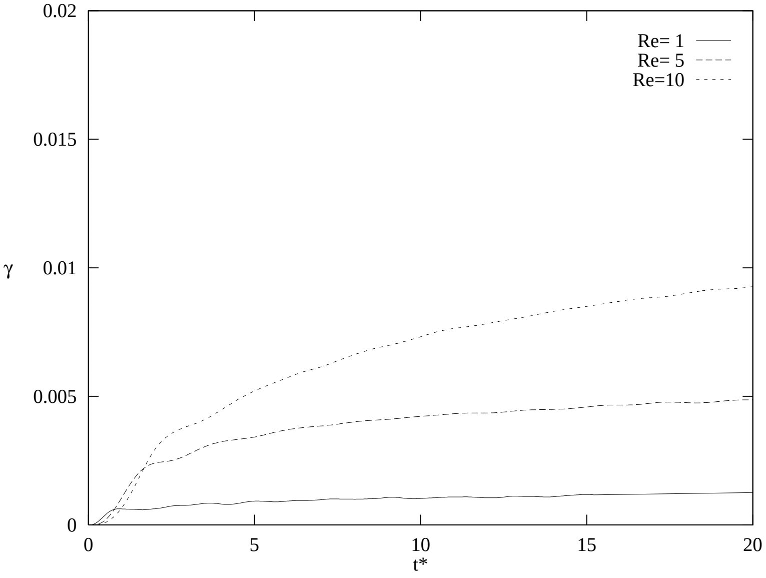

(b) Deformation

Figure 3.6: Effect of Reynolds number on the migration velocity and the deformation of a single bubble. (a) Migration velocity (b) Deformation versus time. Here, $Ma = 1$ and $Ca = 0.06666$.

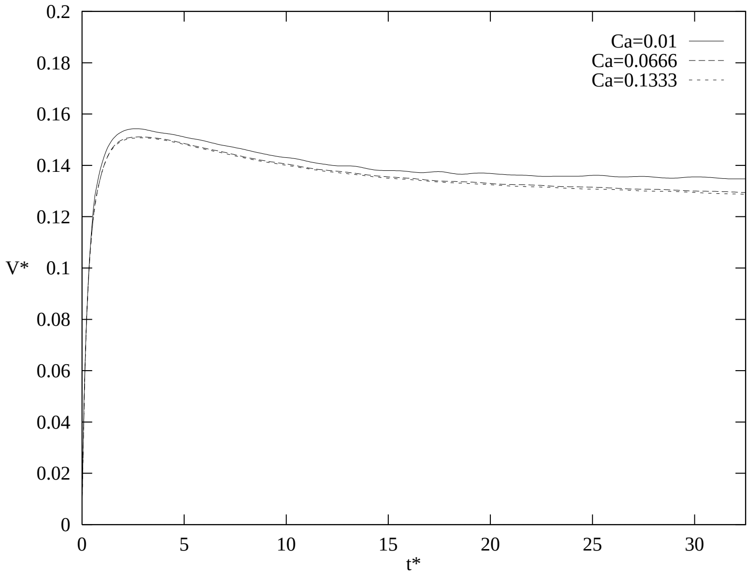

(a) Migration velocity

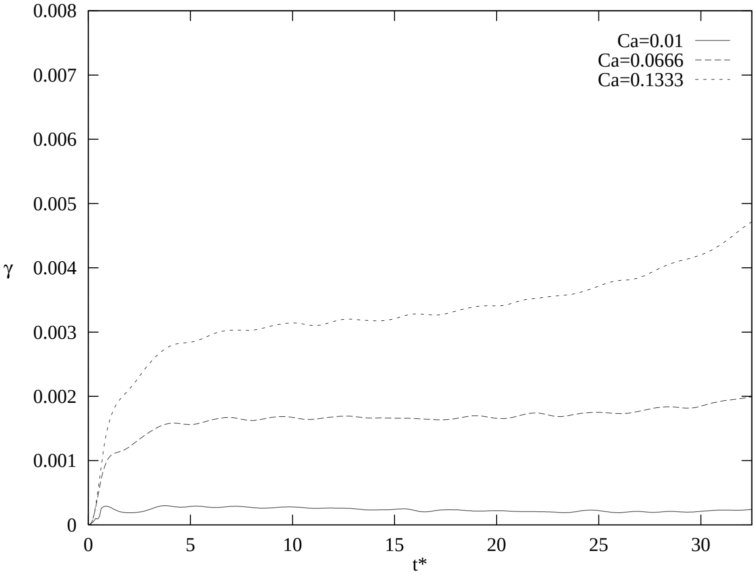

(b) Deformation

Figure 3.7: Effect of Capillary number on the migration velocity and the deformation of a single bubble. (a) Migration velocity (b) Deformation versus time. Here, $Re = Ma = 1$.

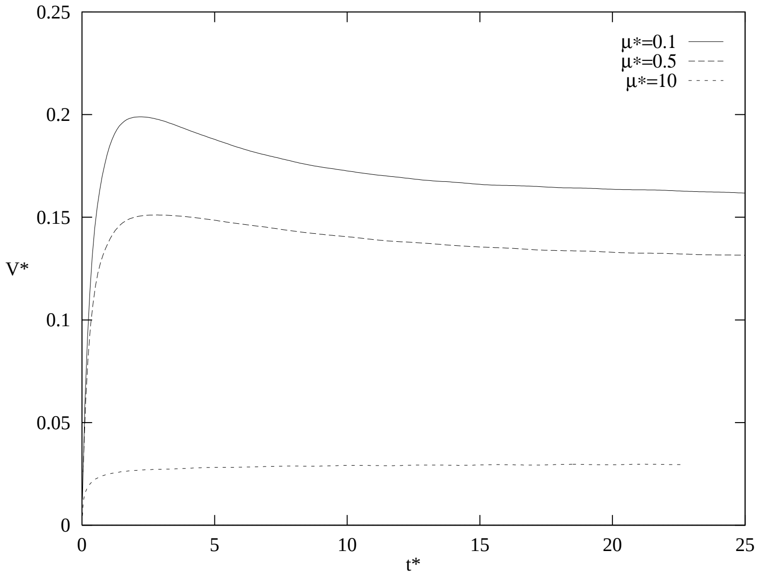

(a) Effect of the viscousity ratio

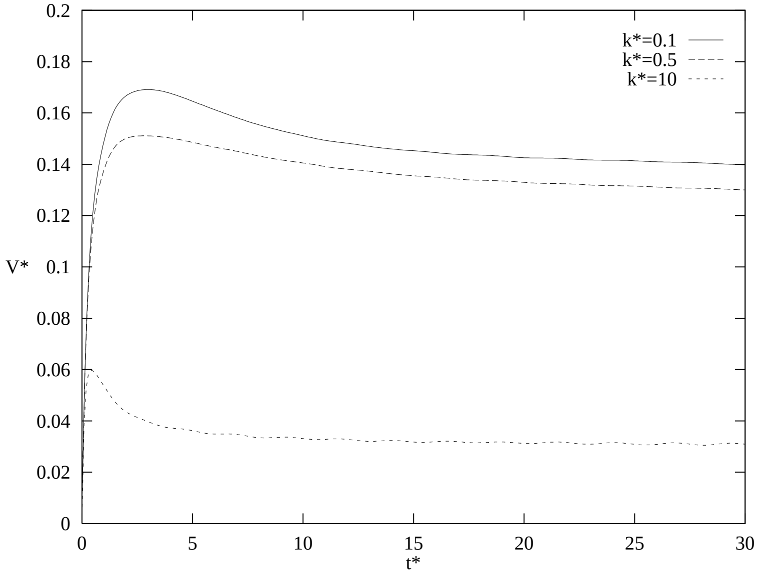

(b) Effect of the conductivity ratio

Figure 3.8: (a) The effect of the viscousity ratio and (b) the effect of the conductivity ratio on the migration velocity of a bubble. Here, $Re = Ma = 1$ and $Ca = 0.06666$.

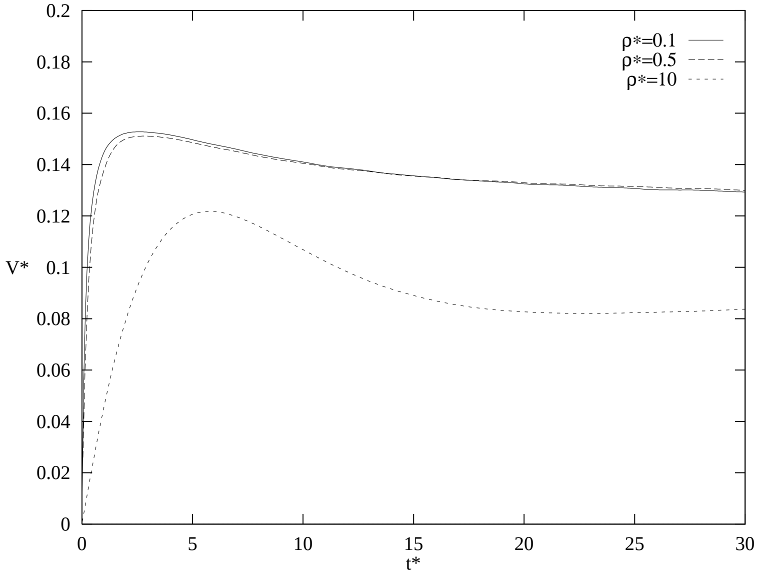

(a) Effect of the density ratio

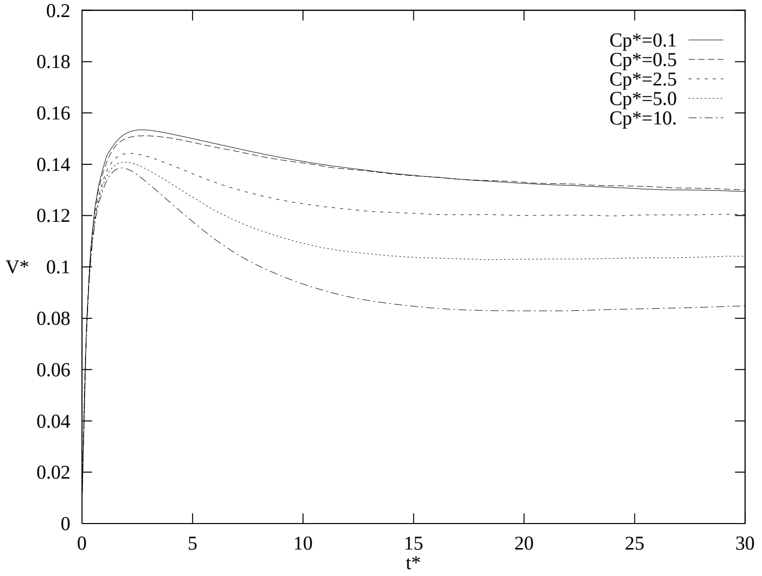

(b) Effect of the heat capacity ratio

Figure 3.9: (*a*) The effect of the density ratio and (*b*) the effect of the heat capacity ratio on the migration velocity of a single bubble. Here, $Re = Ma = 1$ and $Ca = 0.06666$.

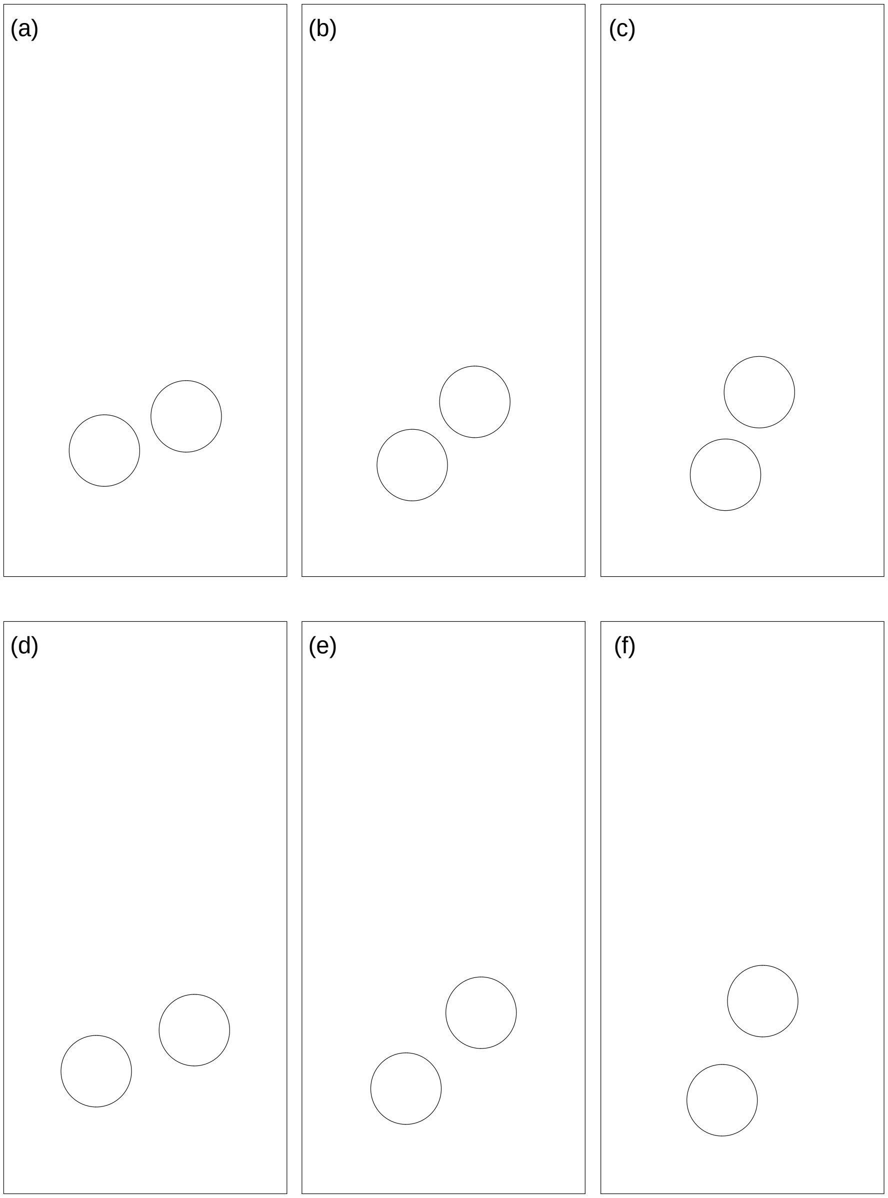

Figure 3.10: 6 different initial position for two-bubble interaction. Computational domain size is $x/a = 8$ and $z/a = 16$.

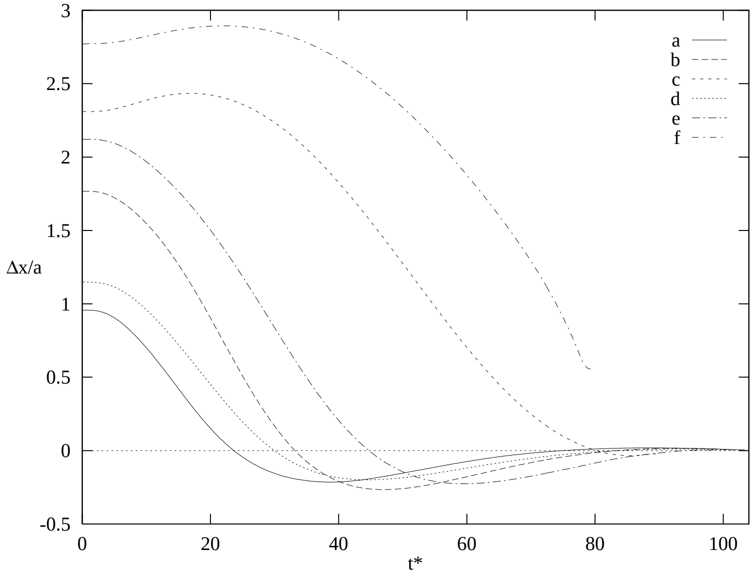

(a) The scaled vertical separation

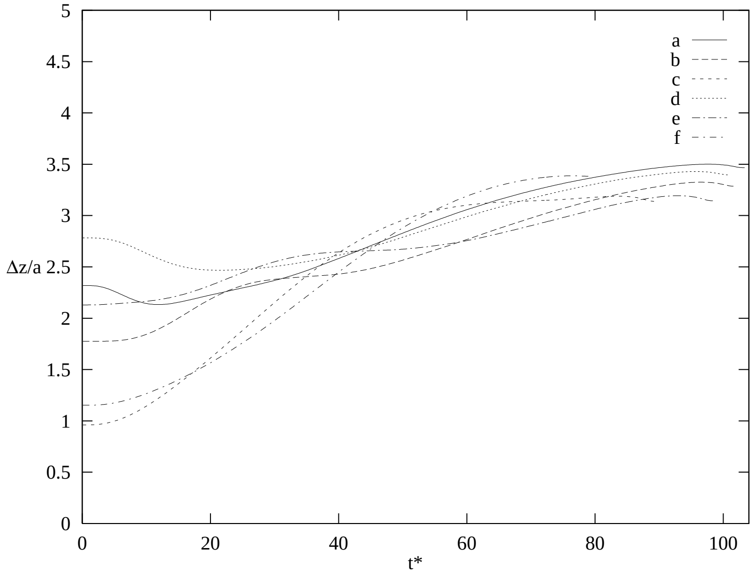

(b) The scaled horizontal separation

Figure 3.11: The scaled (*a*) vertical (*b*) horizontal separation between the bubble on the right and the left versus time. The distance is scaled by bubble radius, a and time is scaled by a/U_r.

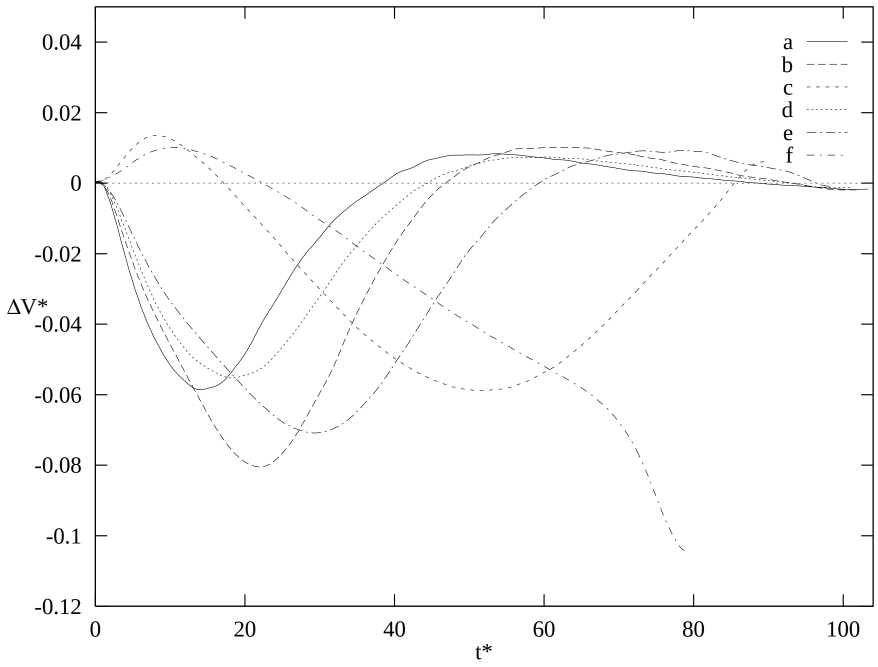

Figure 3.12: The scaled migration velocity difference between the bubble on the right and the left versus time. The velocity difference is scaled by U_r and time is scaled by a/U_r.

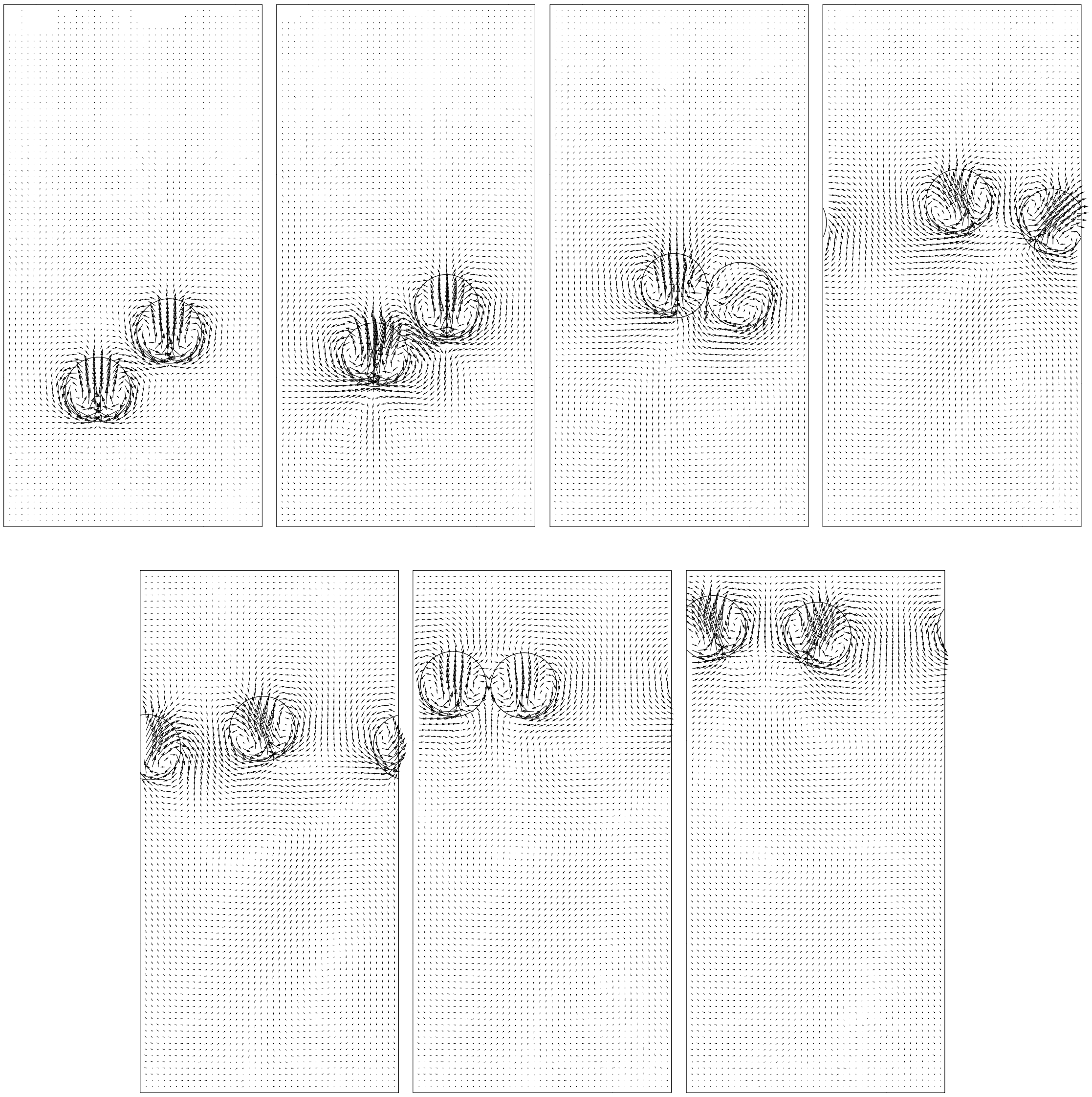

Figure 3.13: Velocity field for selected frames from the computation of two bubble interaction. Only one third of the velocity field is shown. Time progresses from left to right. The nondimensional time, t^*, is equal to $3.8, 11.4, 25.3, 56.9, 69.5, 88.5, 107.5$. The nondimensional time is scaled by a/U_r and velocity is scaled by reference velocity, U_r. Computational domain size is $x/a = 8$ and $z/a = 16$.

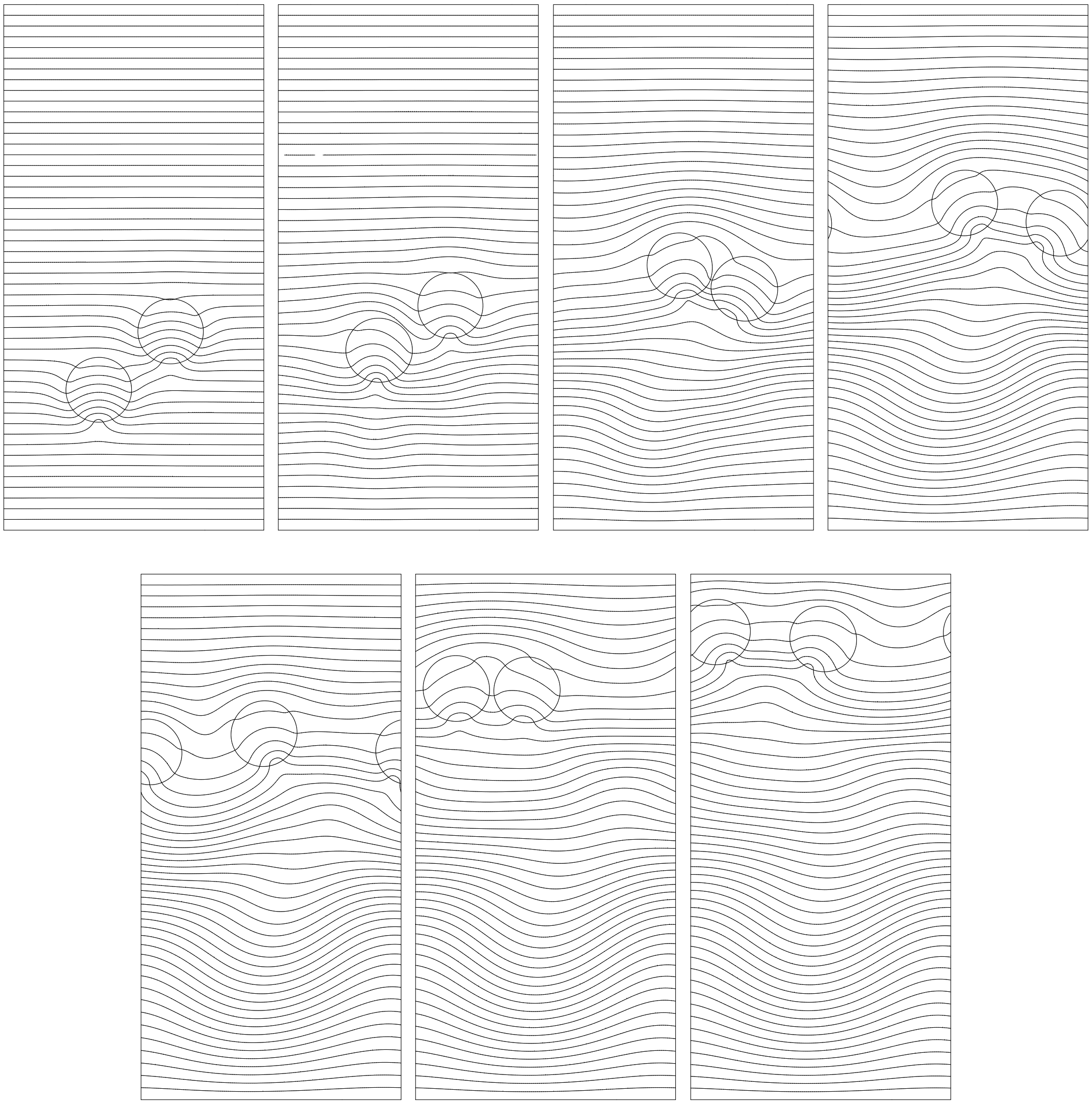

Figure 3.14: Temperature contours for selected frames from the computation of two bubble interaction. 50 equally spaced contours are shown. Time progresses from left to right. The nondimensional time, t^*, is equal to $3.8, 11.4, 25.3, 56.9, 69.5, 88.5, 107.5$. The nondimensional time is scaled by a/U_r and temperature is scaled, after subtracting a reference temperature, by $a\nabla T_\infty$. Computational domain size is $x/a = 8$ and $z/a = 16$. Here, $Re = Ma = 40$ and $Ca = 0.04166$.

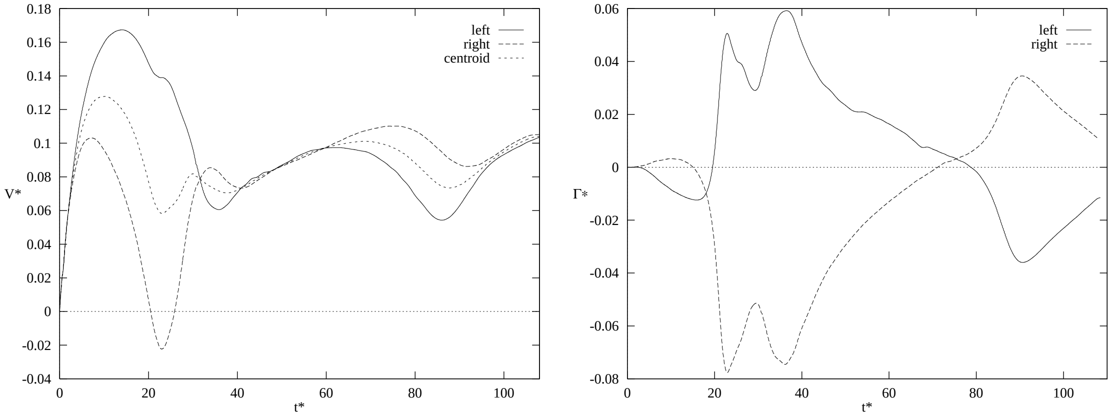

(a) Migration velocity

(b) Internal circulation

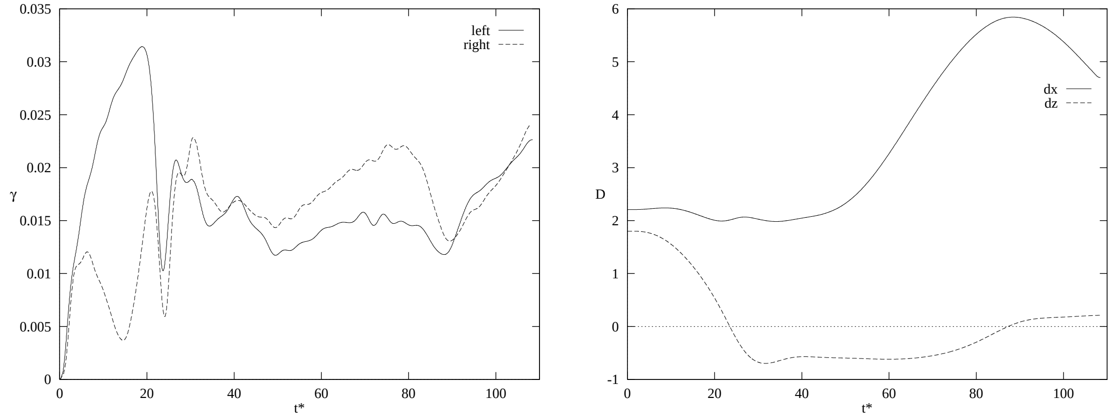

(c) Deformation

(d) Seperation distance

Figure 3.15: Quantitative description of the two bubble interaction in Figure 3.13 and 3.14. (a) Migration velocity versus time. (b) Internal circulation versus time. (c) Deformation versus time. (d) Seperation distance versus time. Velocity is scaled by U_r, separation distance by a, time by a/U_r, and the internal circulation by $2\pi a U_r$.

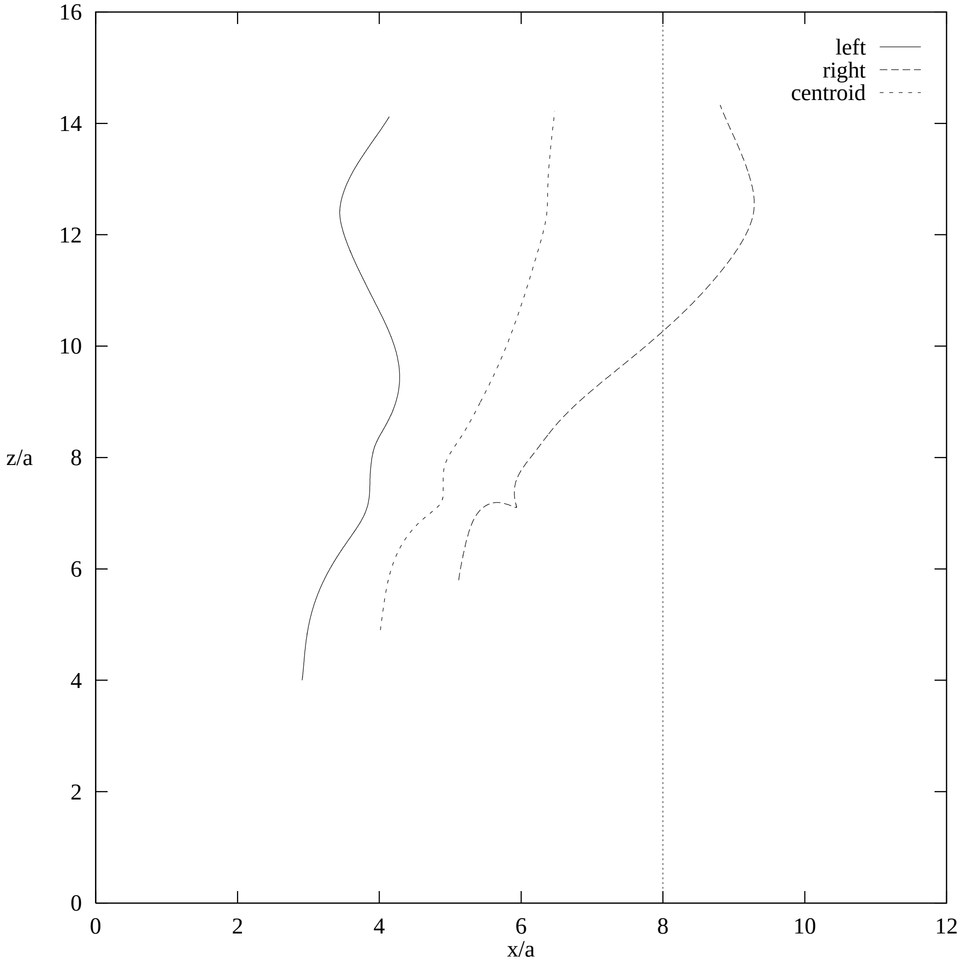

Figure 3.16: Trajectories of the center of mass of the bubbles in Figure 3.13 and 3.14. Both axis are scaled by the bubble radius a.

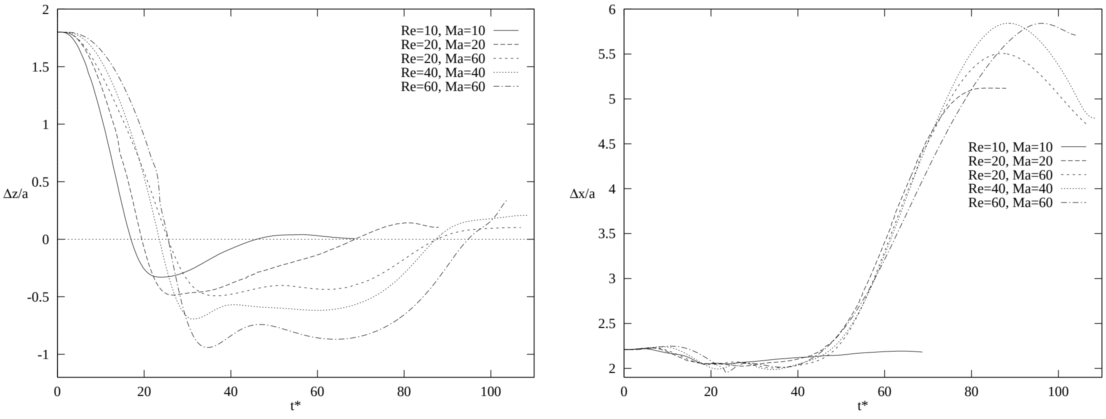

(a) The vertical separation distance

(b) The horizontal separation distance

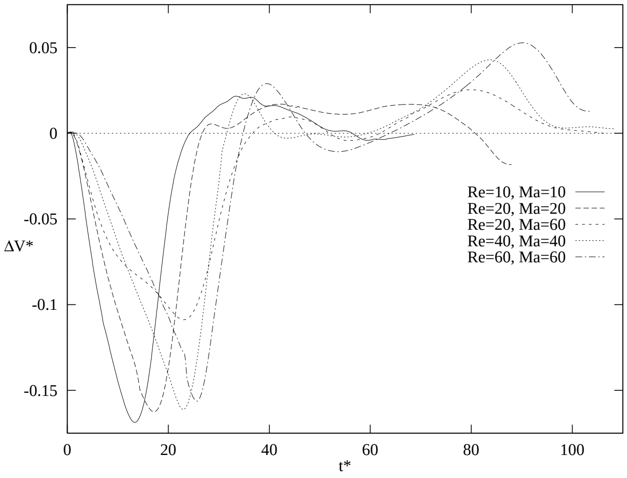

(c) The migration velocity difference

Figure 3.17: Quantitative information about two-bubble interaction for different Reynolds and Marangoni numbers. (*a*) The vertical separation distance versus time. (*b*) The horizontal separation distance versus time. (*c*) The migration velocity difference versus time. Time is scaled by a/U_r, separation difference, Δ, by, a, and the velocity difference by U_r. The differences are between the bubble on the right and the left.

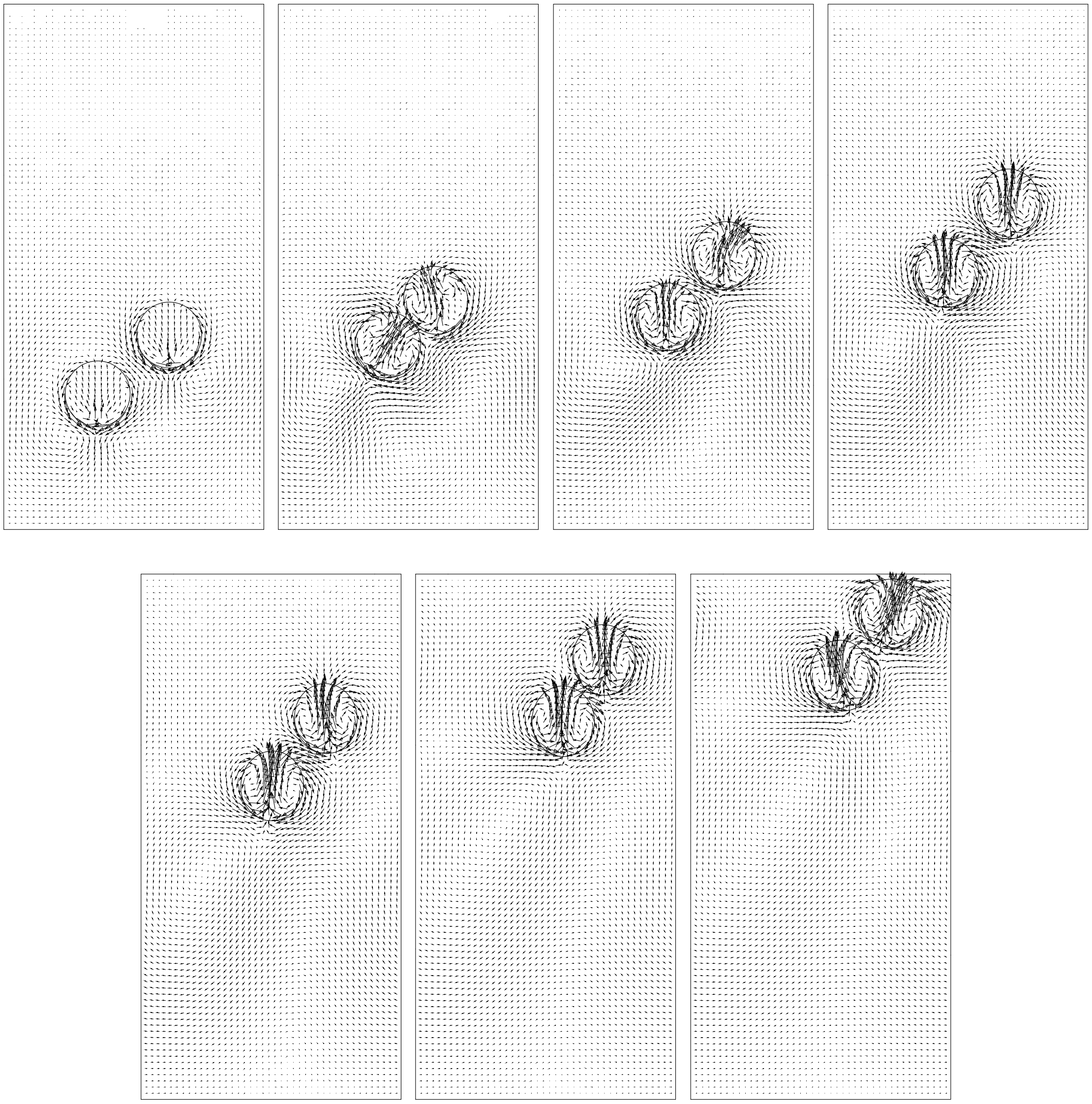

Figure 3.18: Velocity field for selected frames from the computation of two drop interaction. The velocity field is shown at every third grid point. Time progresses from left to right. The nondimensional time, t^*, is equal to $12.65, 50.60, 75.89, 101.19, 126.49, 151.79, 170.0$. The nondimensional time is scaled by a/U_r and velocity is scaled by reference velocity, U_r. Computational domain size is $x/a = 8$ and $z/a = 16$. Here, $Re = Ma = 40$ and $Ca = 0.04166$.

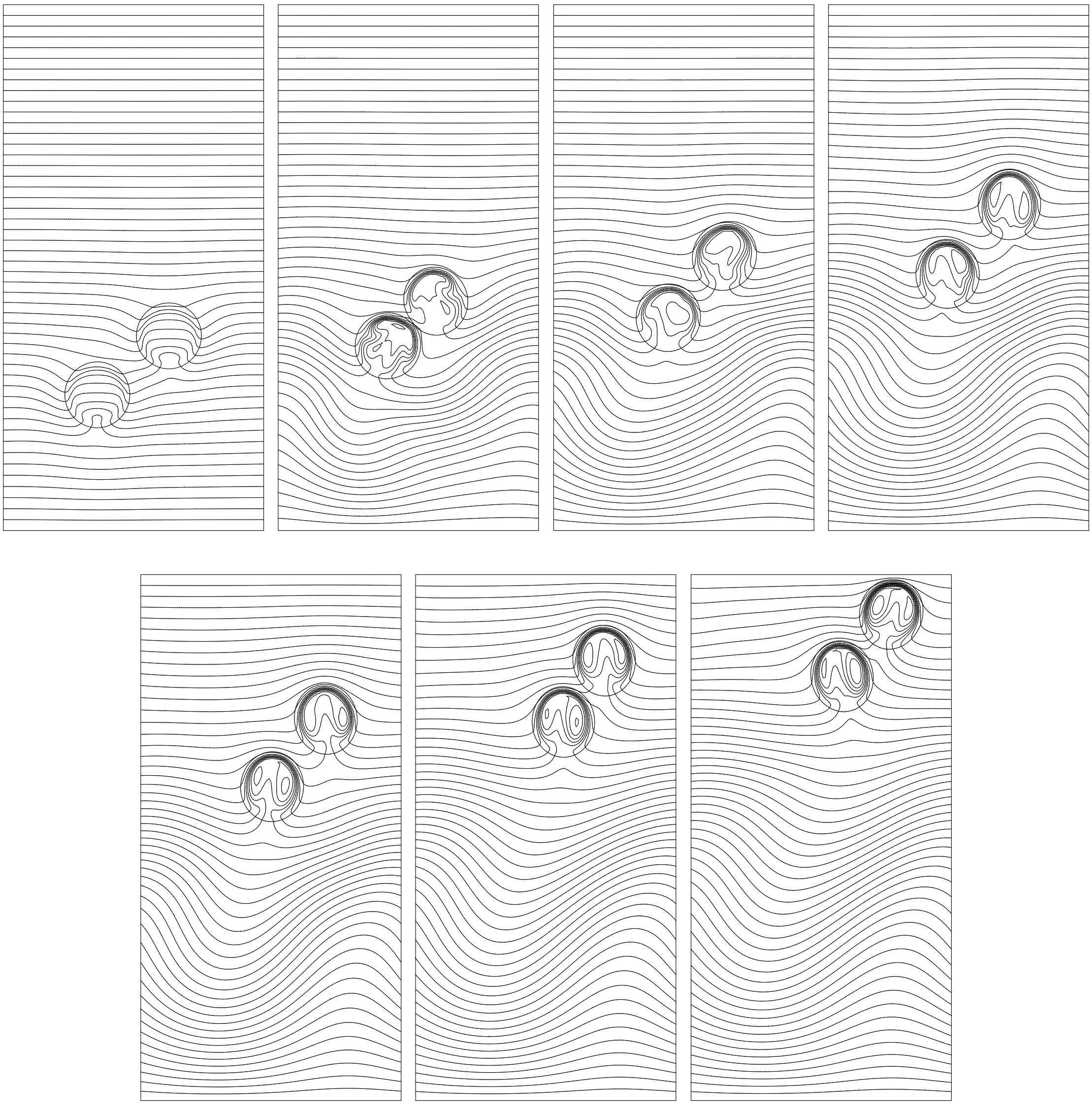

Figure 3.19: Temperature contours for selected frames from the computation of two drop interaction in Figure 3.18. 50 equally spaced contours are shown. Time progresses from left to right. The nondimensional time, t^*, is equal to $12.65, 50.60, 75.89, 101.19, 126.49, 151.79, 170.0$. The nondimensional time is scaled by a/U_r and temperature is scaled, after subtracting a reference temperature, by $a\nabla T_\infty$. Computational domain size is $x/a = 8$ and $z/a = 16$.

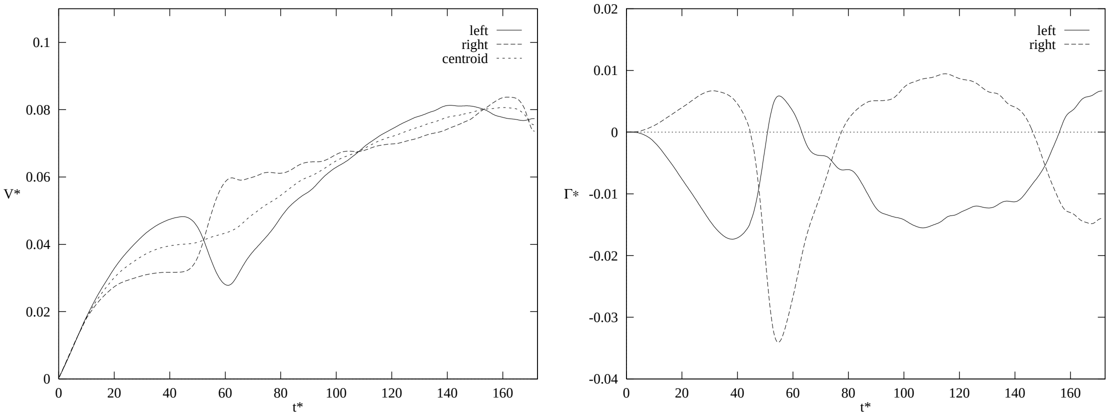

(a) Migration velocity

(b) Internal circulation

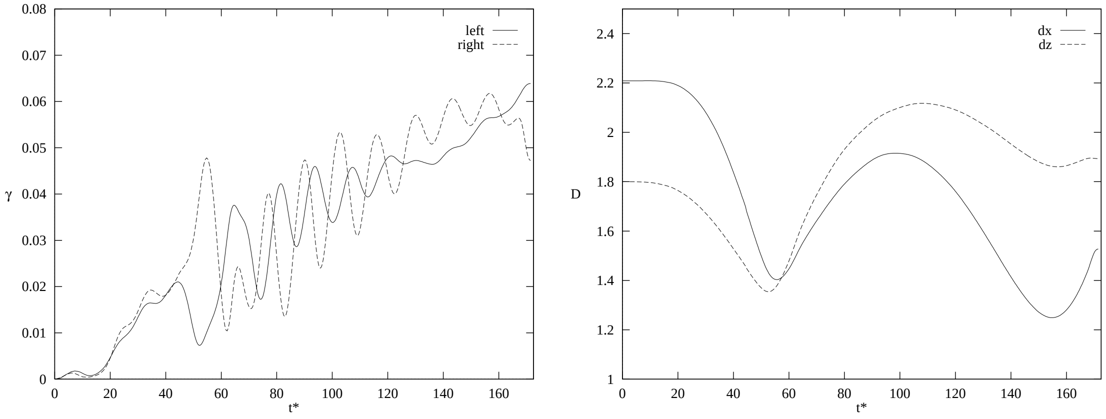

(c) Deformation

(d) Separation distance

Figure 3.20: Quantitative description of the two drop interaction in Figures 3.18 and 3.19. (a) Migration velocity versus time. (b) Internal circulation versus time. (c) Deformation versus time. (d) Separation distance versus time. Velocity is scaled by U_r, separation distance by a, time by a/U_r, and the internal circulation by $2\pi a U_r$.

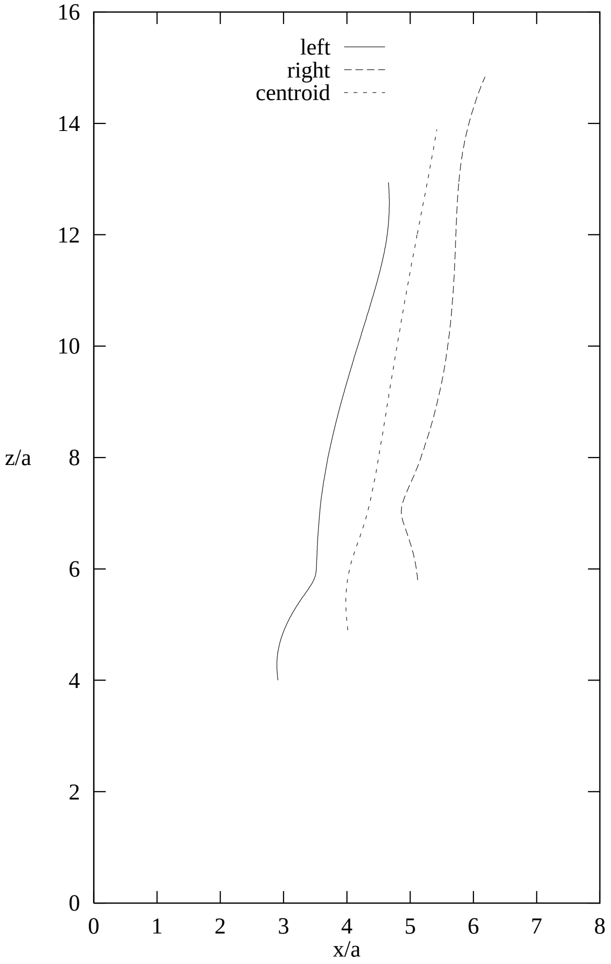

Figure 3.21: Trajectories of the center of mass of drops in Figures 3.18 and 3.19. Both axis are scaled by the drop radius a.

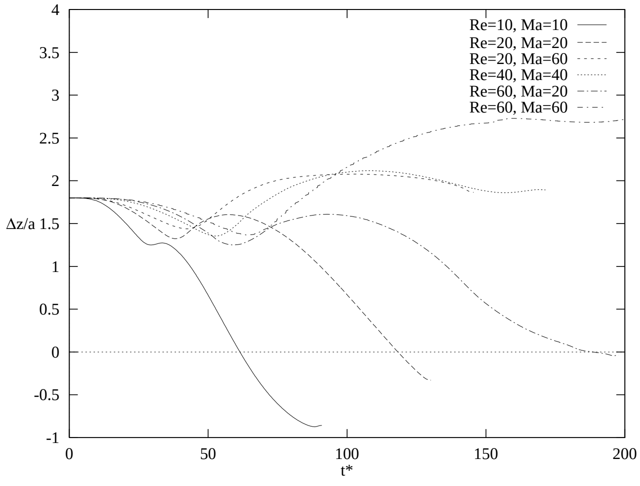

(a) The vertical separation distance

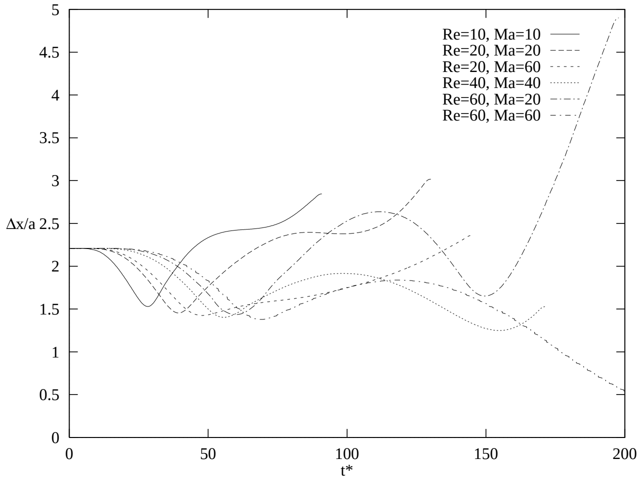

(b) The horizontal separation distance

Figure 3.22: Quantitative information for two-drop interactions for different Reynolds and Marangoni numbers. (a) The vertical separation distance versus time. (b) The horizontal separation distance versus time. Time is scaled by a/U_r, separation difference, Δ, by, a. The differences are between the drop on the right and drop on the left.

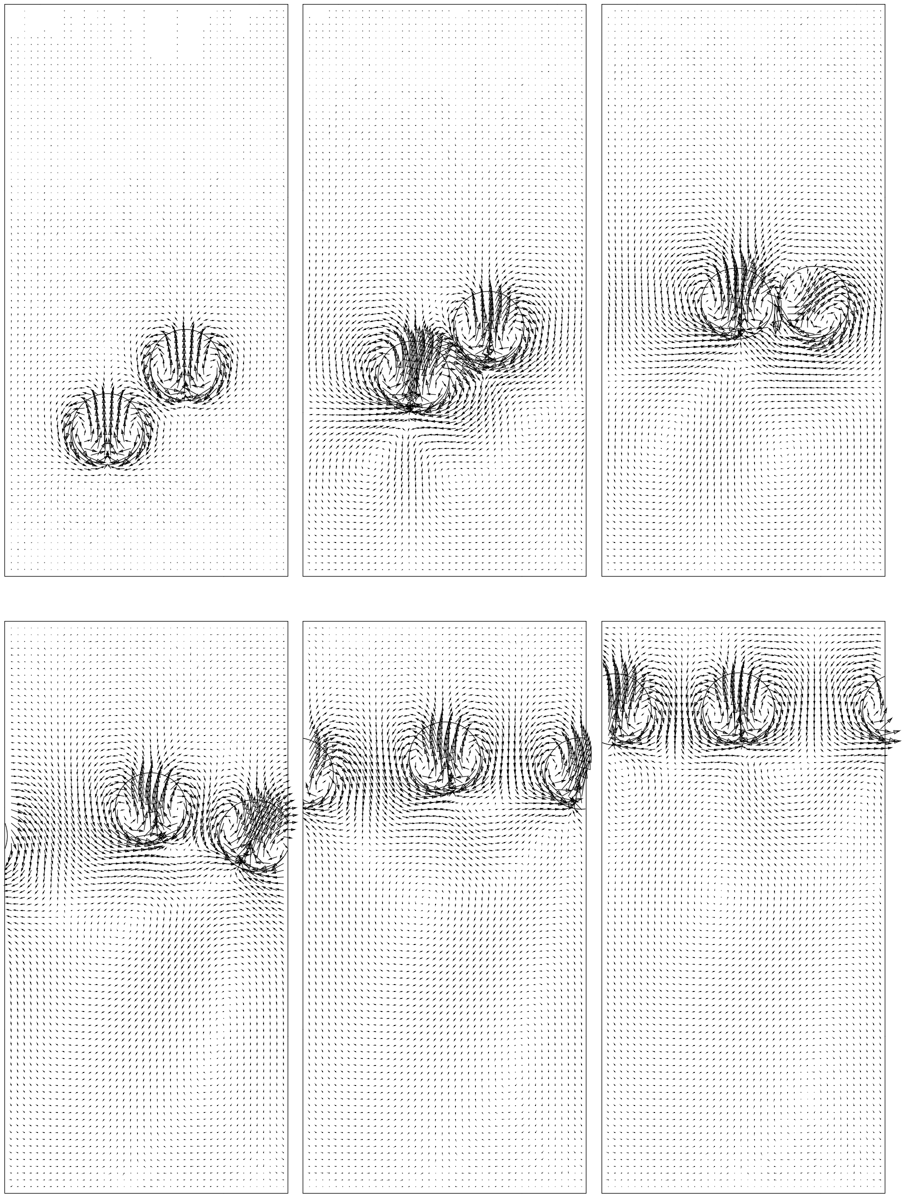

Figure 3.23: Velocity field for selected frames from the computation of two bubble interaction. The velocity field is shown at every third grid point. Time progresses from left to right. The nondimensional time, t^*, is equal to $4, 20, 40, 80, 100, 120$. The nondimensional time is scaled by a/U_r and velocity is scaled by reference velocity, U_r. Computational domain size is $x/a = 8$ and $z/a = 16$. Here, $Re = Ma = 40$ and $Ca = 0.04166$.

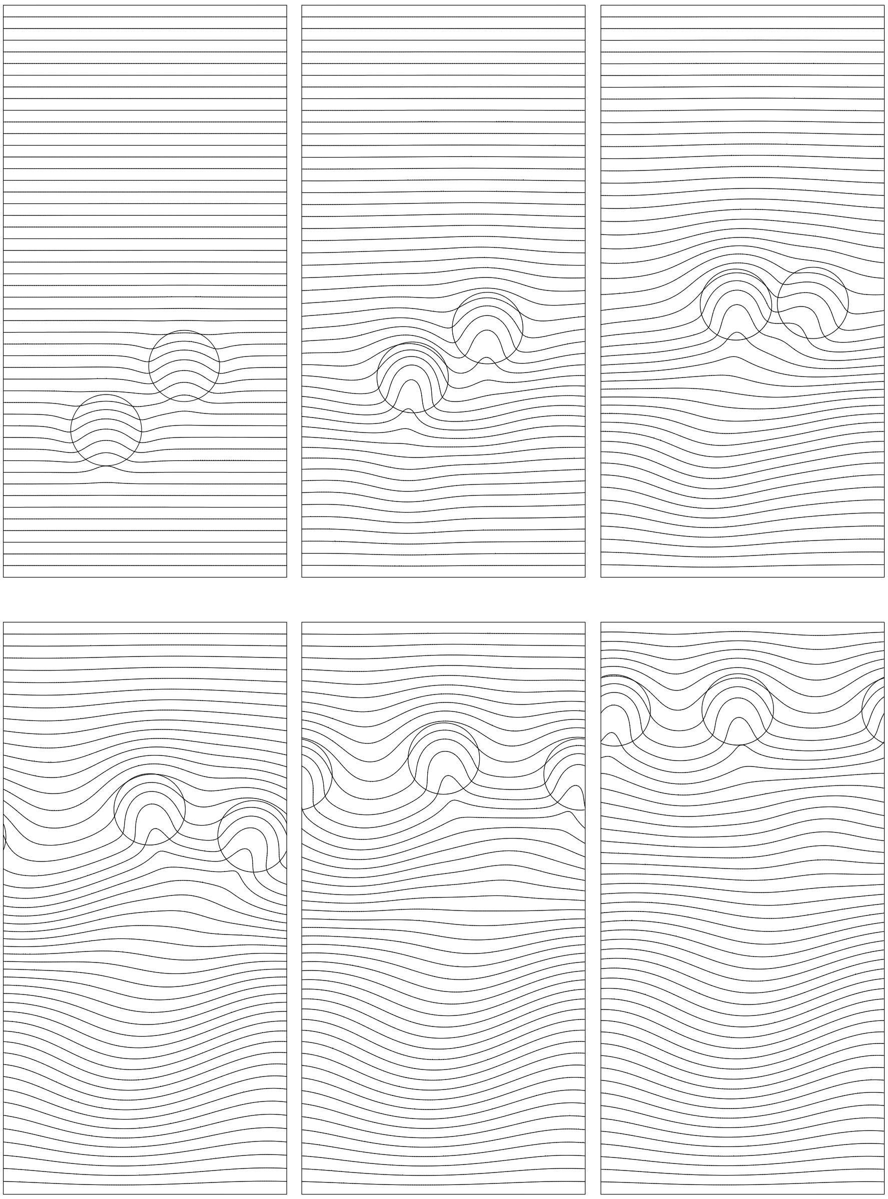

Figure 3.24: Temperature contours for selected frames from the computation of two bubble interaction in Figure 3.23. 50 equally spaced contours are shown. Time progresses from left to right. The nondimensional time, t^*, is equal to $4, 20, 40, 80, 100, 120$. The nondimensional time is scaled by a/U_r and temperature is scaled, after subtracting a reference temperature, by $a\nabla T_\infty$. Computational domain size is $x/a = 8$ and $z/a = 16$.

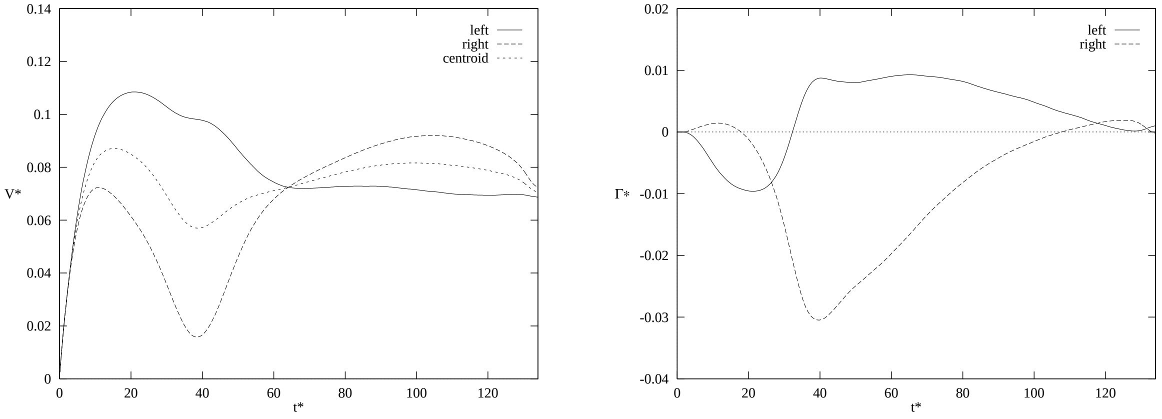

(a) Migration velocity (b) Internal circulation

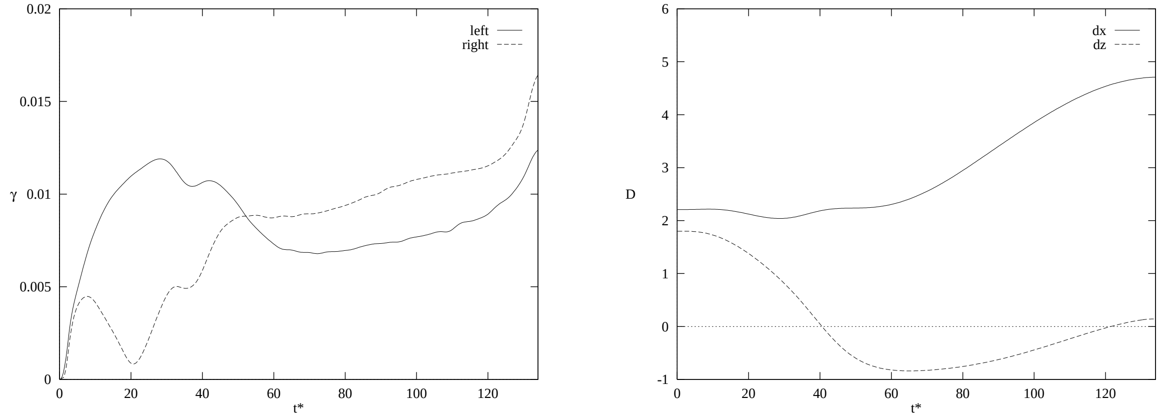

(c) Deformation (d) Separation distance

Figure 3.25: Quantitative description of the two bubble interaction in Figures 3.23 and 3.24. (*a*) Migration velocity versus time. (*b*) Internal circulation versus time. (*c*) Deformation versus time. (*d*) Separation distance versus time. Velocity is scaled by U_r, separation distance by a, time by a/U_r, and the internal circulation by $2\pi a U_r$.

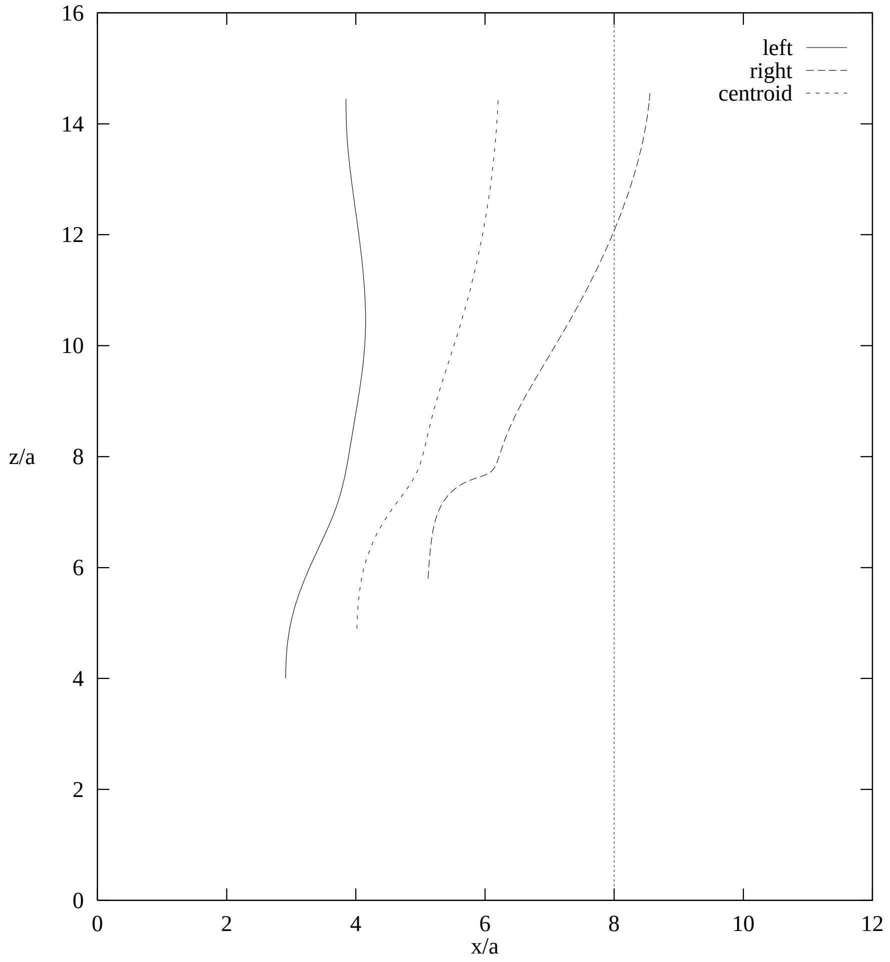

Figure 3.26: Trajectories of the center of mass of the bubbles in Figures 3.23 and 3.24. Both axis are scaled by the bubble radius a.

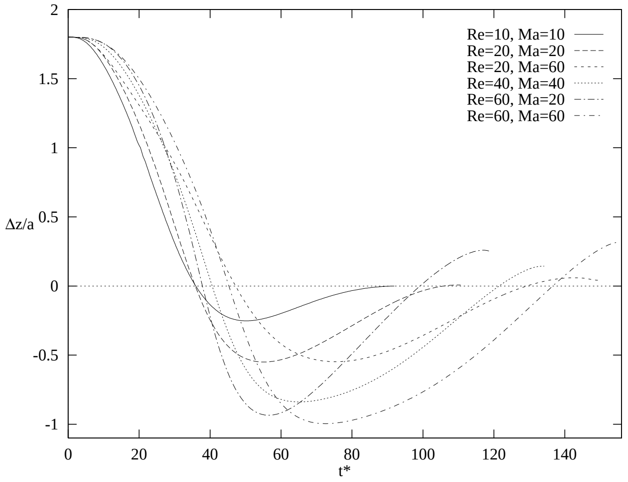

(a) The vertical separation distance

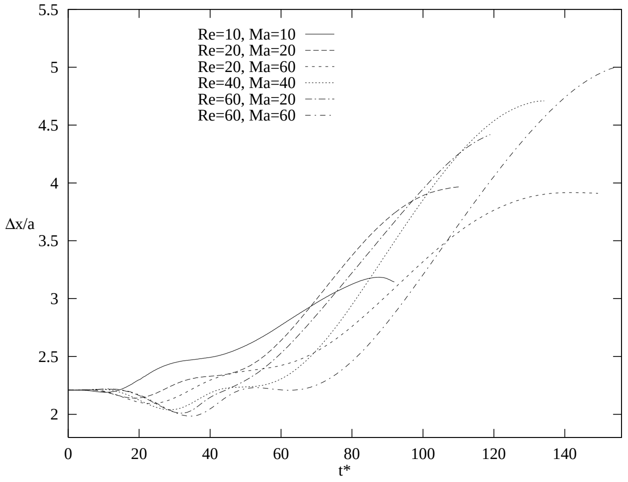

(b) The horizontal separation distance

Figure 3.27: Quantitative information for two-bubble interactions for different Reynolds and Marangoni numbers. (a) The vertical separation distance versus time. (b) The horizontal separation distance versus time. Time is scaled by a/U_r, separation difference, D, by, a. The differences are between the bubble on the right and the left.

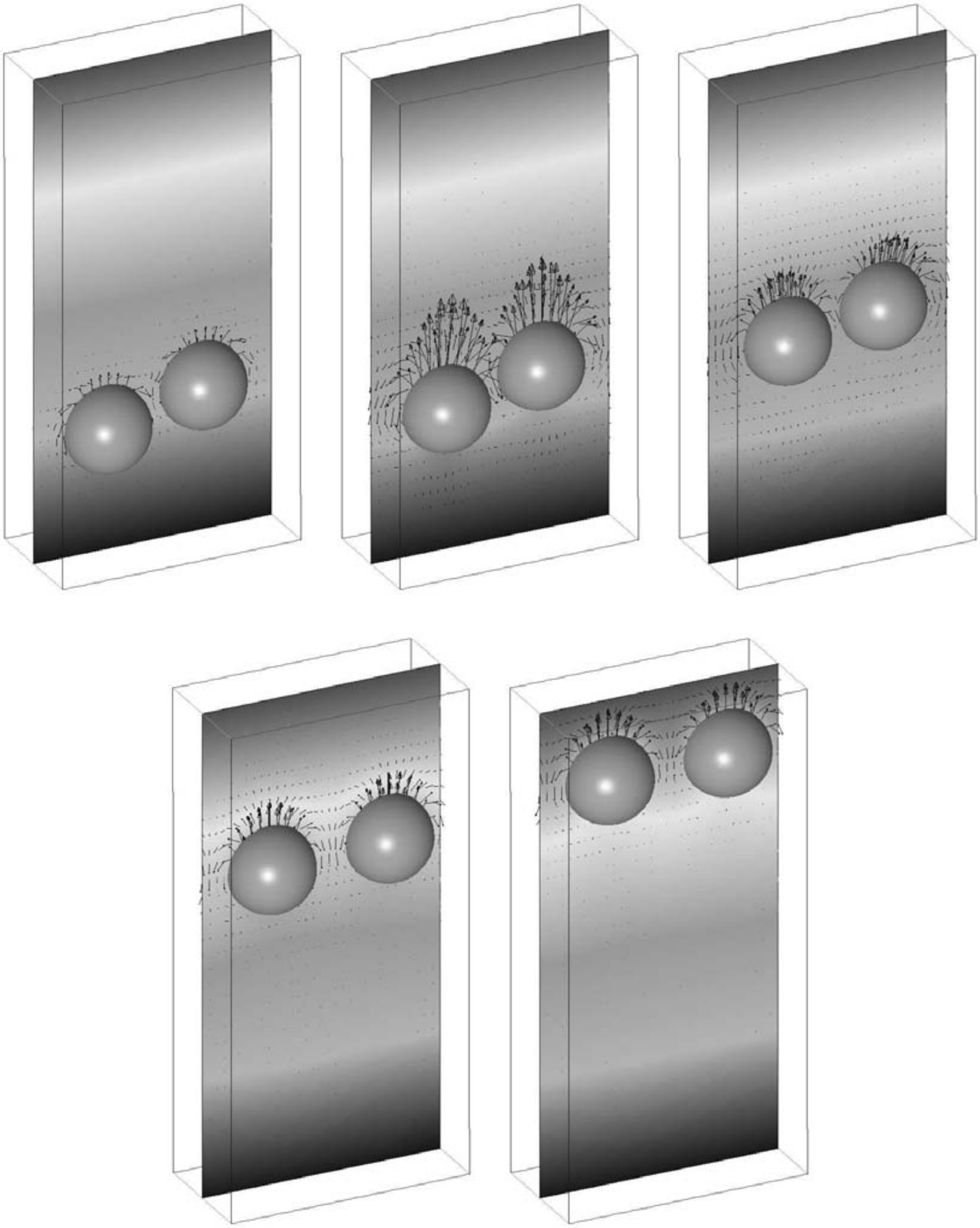

Figure 3.28: Velocity and temperature field for selected frames from the fully three-dimensional simulation of two-bubble interaction. The velocity field is shown at every other grid point in the middle plane of the computational box in y direction. Time progresses from left to right, top to bottom. The nondimensional time, t^*, is equal to $0.57, 5.71, 22.85$, $57.14, 85.71$. The nondimensional time is scaled by a/U_r and velocity is scaled by reference velocity, U_r. Computational domain size is $x/a = 5.71$, $y/a = 2.86$ and $z/a = 11.43$. Here, $Re = 20$, $Ma = 60$ and $Ca = 0.04166$.

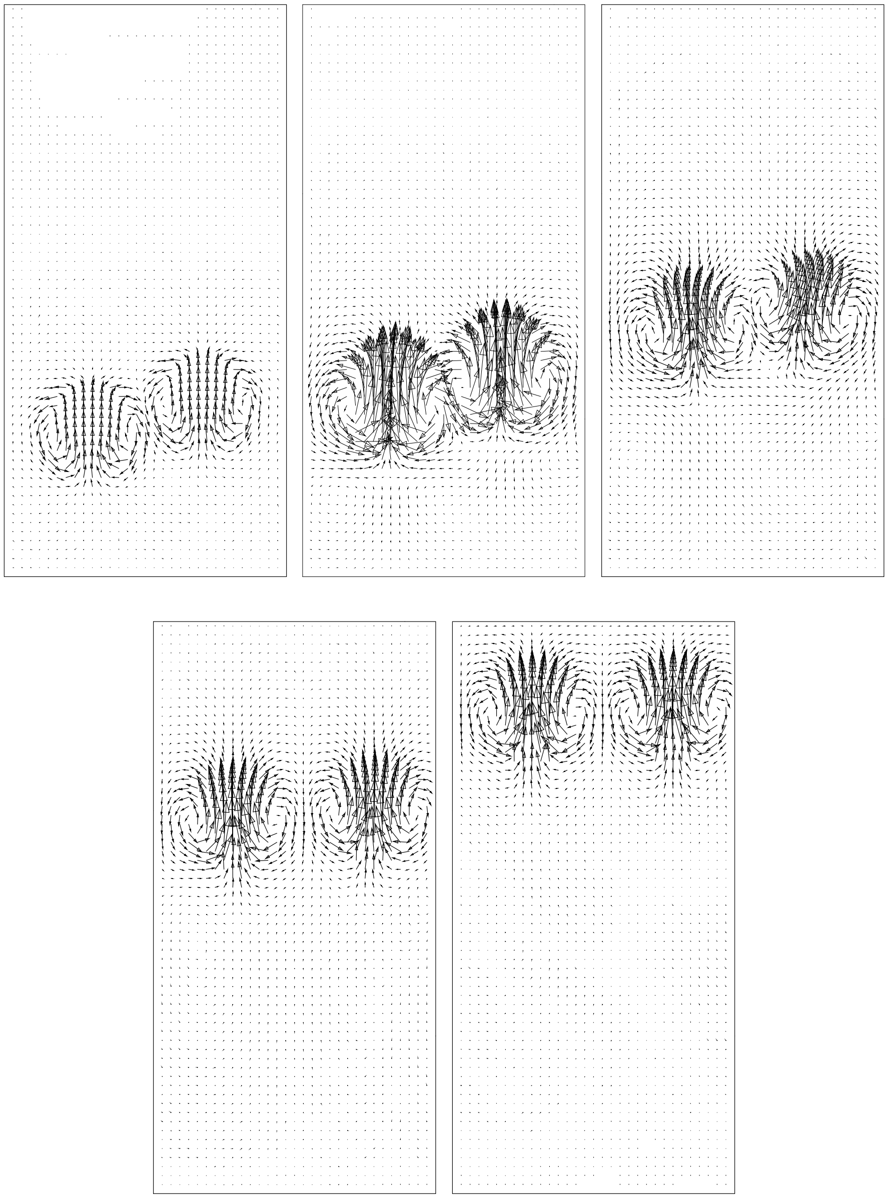

Figure 3.29: Velocity field for selected frames from the fully three dimensional computation of two bubble interaction in Figure 3.28. The velocity field is shown at every other grid point in the middle plane of the computational box in y direction. Time progresses from left to right. The nondimensional time, t^*, is equal to $0.57, 5.71, 22.85, 57.14, 85.71$. The nondimensional time is scaled by a/U_r and velocity by U_r. Computational domain size is $x/a = 5.71$, $y/a = 2.86$ and $z/a = 11.43$.

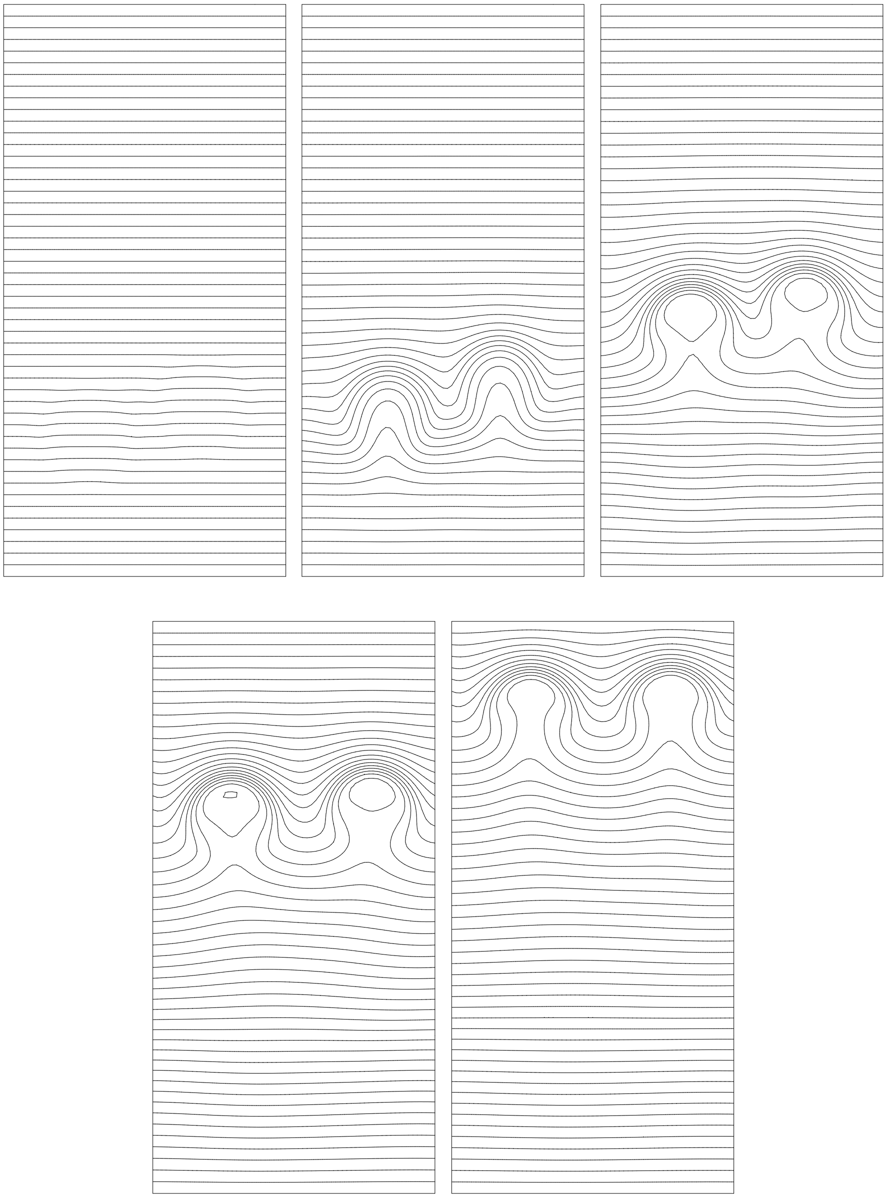

Figure 3.30: Temperature contours for selected frames from the fully three dimensional computation of two bubble interaction in Figure 3.28. 50 equally spaced contours are shown in the middle plane of the computational box in y direction. Time progresses from left to right. The nondimensional time, t^*, is equal to $0.57, 5.71, 22.85, 57.14, 85.71$. The nondimensional time is scaled by a/U_r and temperature is scaled, after subtracting a reference temperature, by $a\nabla T_\infty$. Computational domain size is $x/a = 5.71$, $y/a = 2.86$ and $z/a = 11.43$.

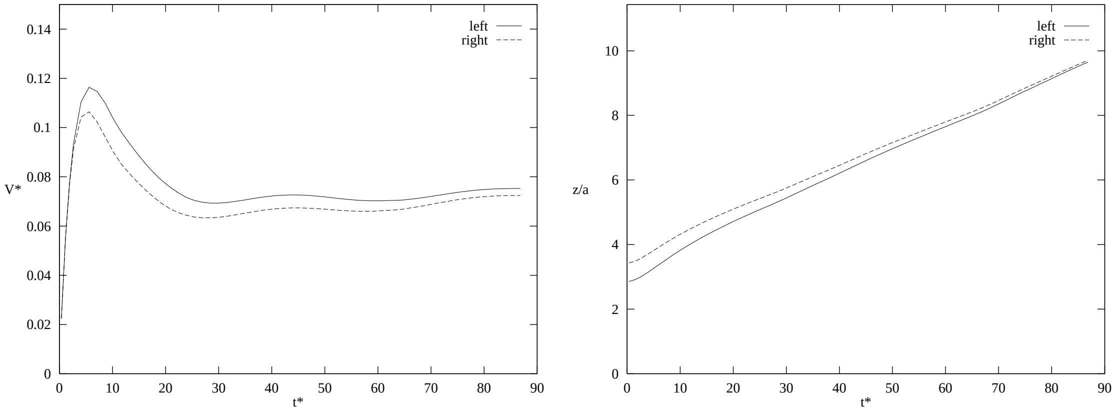

(a) Migration velocity

(b) Vertical position

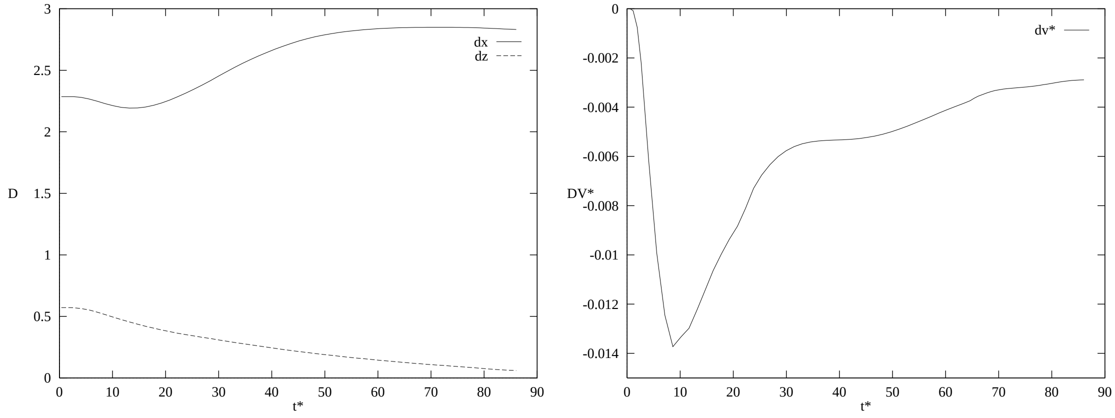

(c) Separation distance

(d) Velocity difference

Figure 3.31: Quantitative description of the two-bubble interaction in Figures 3.28, 3.29 and 3.30. (*a*) Migration velocity versus time. (*b*) z component of the centroid of bubbles versus time. (*c*) The separation distance versus time and (*d*) The velocity difference versus time between the bubble on the right and the left. Velocity is scaled by reference velocity U_r, seperation distance and z axis by a, and time by a/U_r.

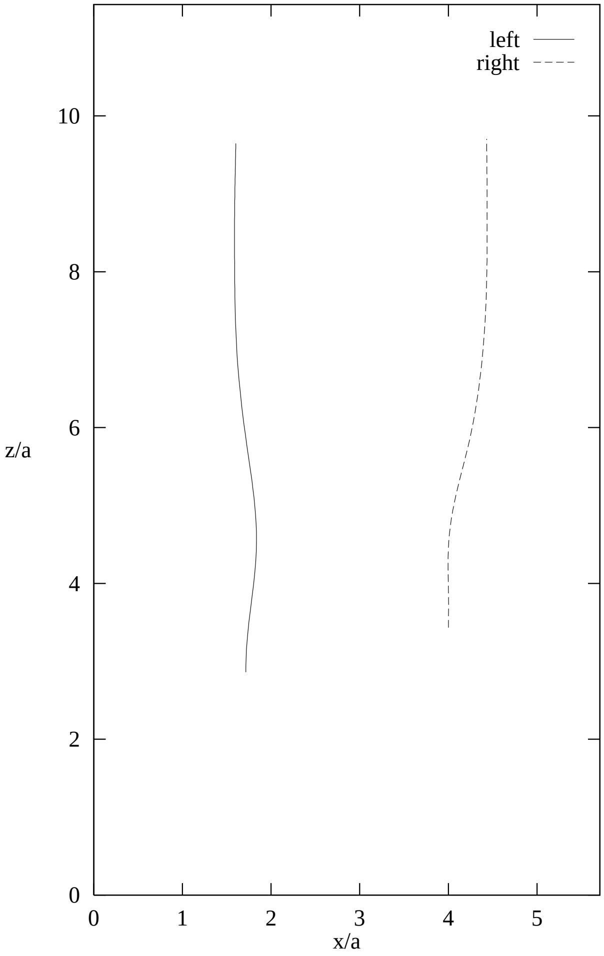

Figure 3.32: Trajectories of the center of mass of the bubbles. Both axis are scaled by the bubble radius a.

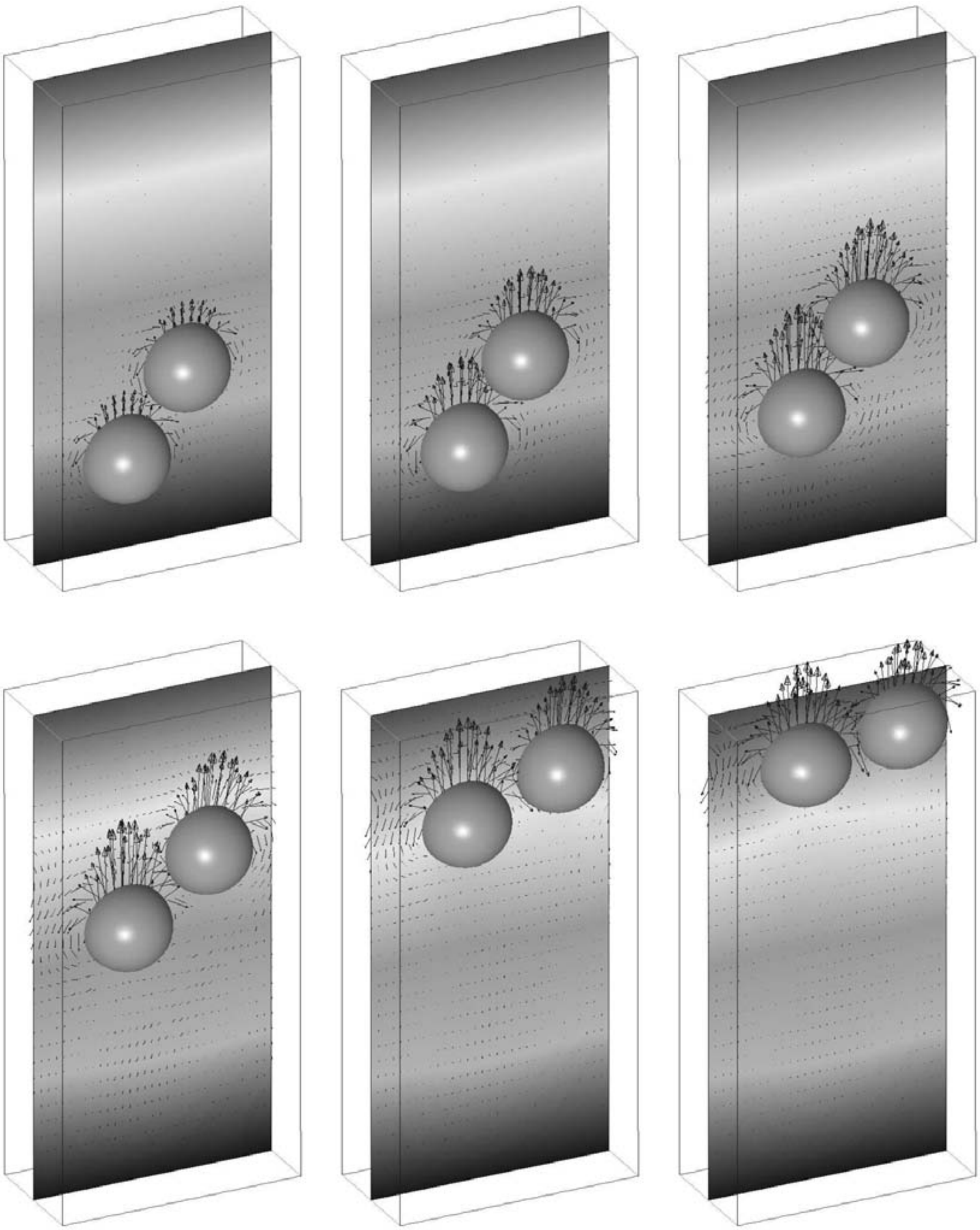

Figure 3.33: Velocity and temperature field for selected frames from the fully three-dimensional simulation of two-bubble interaction. The velocity field is shown at every other grid point in the middle plane of the computational box in y direction. Time progresses from left to right, top to bottom. The nondimensional time, t^*, is equal to $3.5, 7.0, 14.0, 35.0,\ 52.5, 63.0$. The nondimensional time is scaled by a/U_r and velocity is scaled by reference velocity, U_r. Computational domain size is $x/a = 5.71$, $y/a = 2.86$ and $z/a = 11.43$. Here, $Re = 60$, $Ma = 20$ and $Ca = 0.04166$.

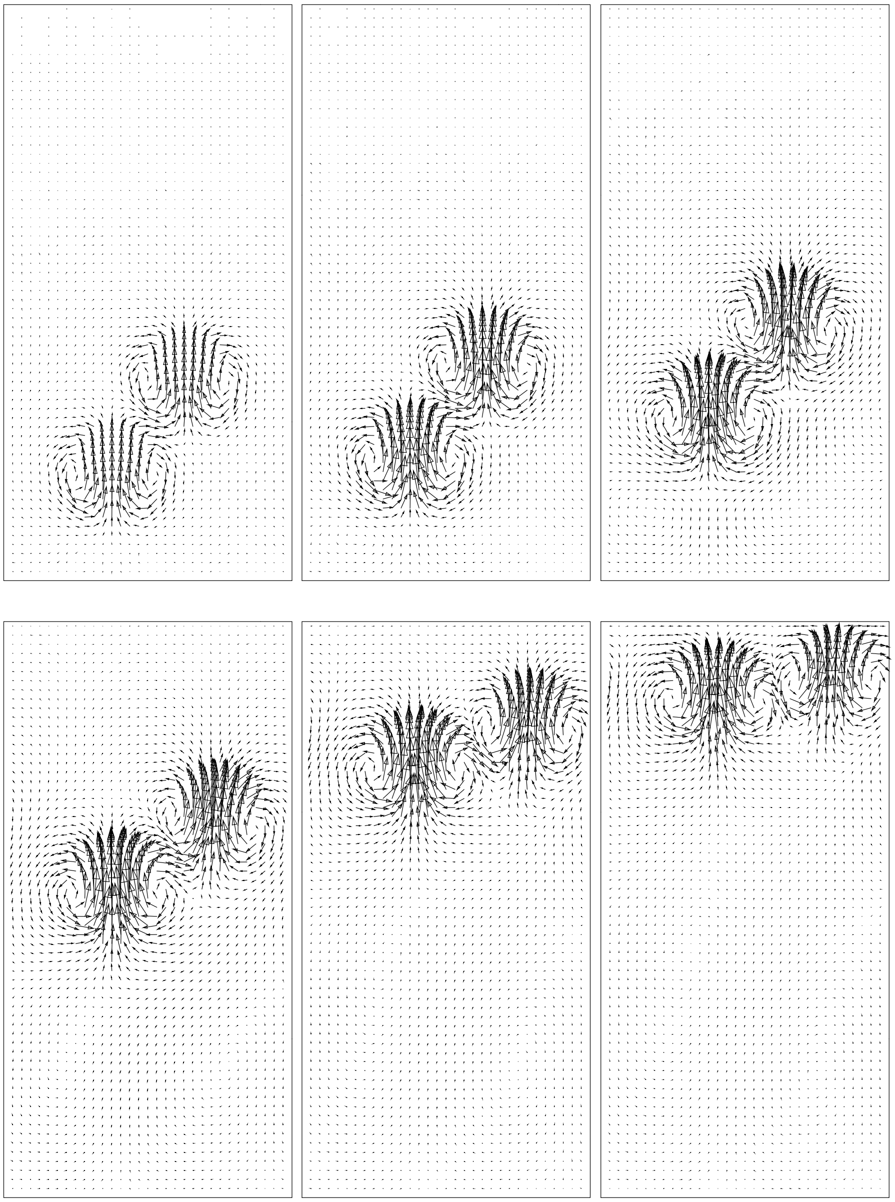

Figure 3.34: Velocity field for selected frames from the fully three dimensional computation of two bubble interaction. The velocity field is shown at every other grid point in the middle plane of the computational box in y direction. Time progresses from left to right. The nondimensional time, t^*, is equal to $3.5, 7.0, 14.0, 35.0,\ 52.5, 63.0$. The nondimensional time is scaled by a/U_r and velocity by U_r. Computational domain size is $x/a = 5.71$, $y/a = 2.86$ and $z/a = 11.43$.

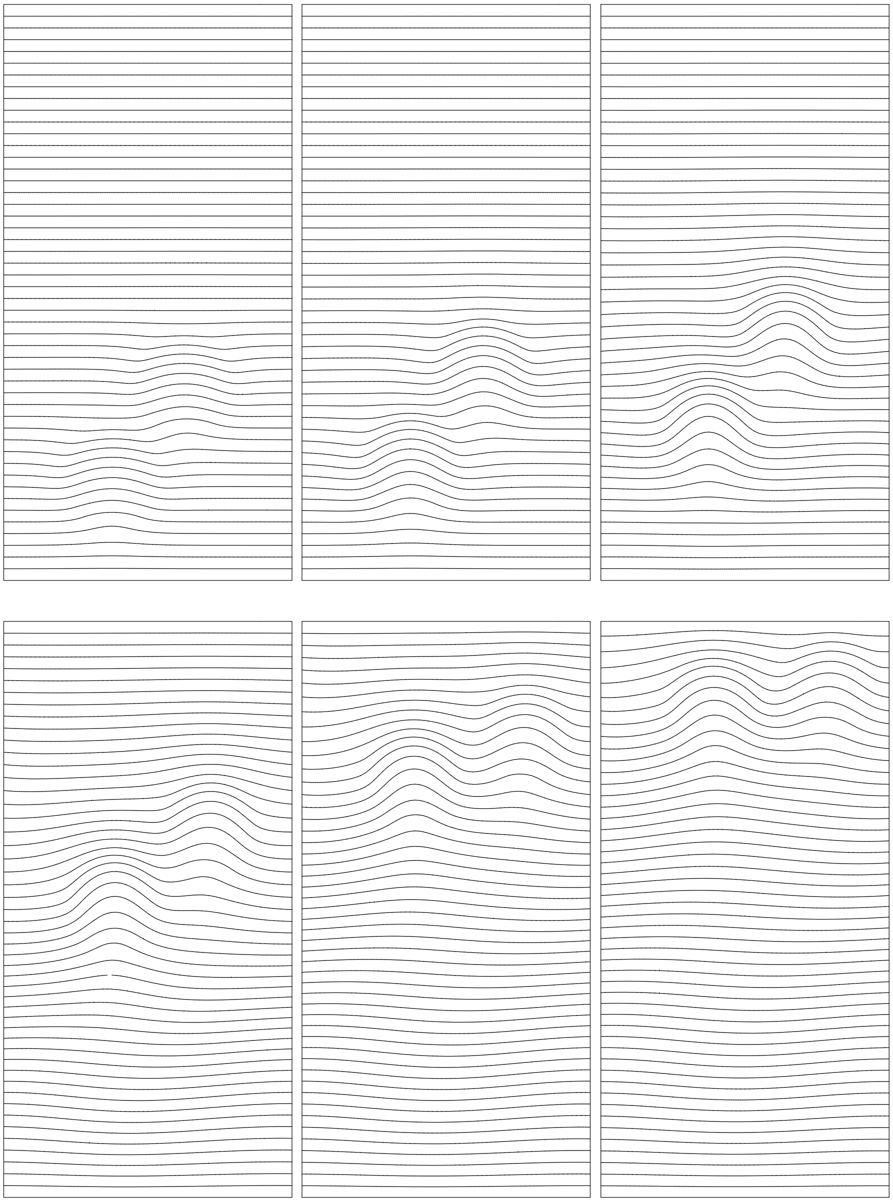

Figure 3.35: Temperature contours for selected frames from the fully three dimensional computation of two bubble interaction. 50 equally spaced contours are shown in the middle plane of the computational box in y direction. Time progresses from left to right. The nondimensional time, t^*, is equal to $3.5, 7.0, 14.0, 35.0, 52.5, 63.0$. The nondimensional time is scaled by a/U_r and temperature is scaled, after subtracting a reference temperature, by $a\nabla T_\infty$. Computational domain size is $x/a = 5.71$, $y/a = 2.86$ and $z/a = 11.43$.

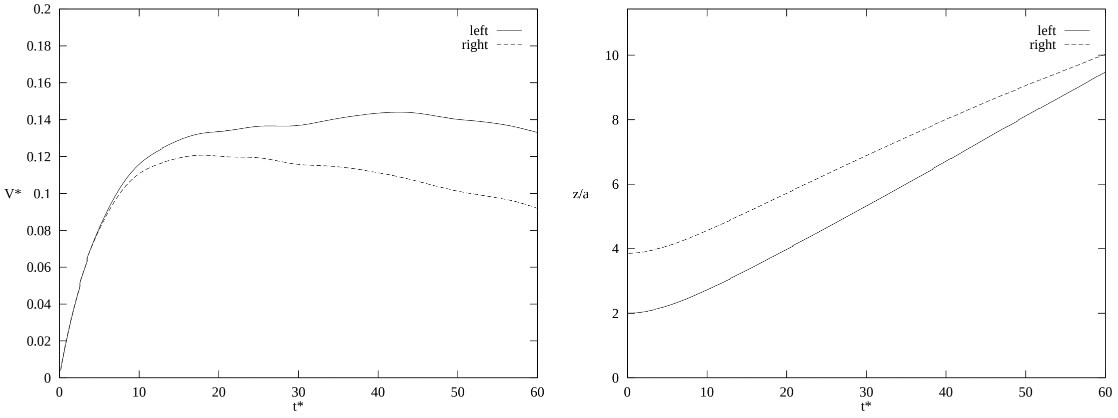

(a) Migration velocity

(b) Vertical position

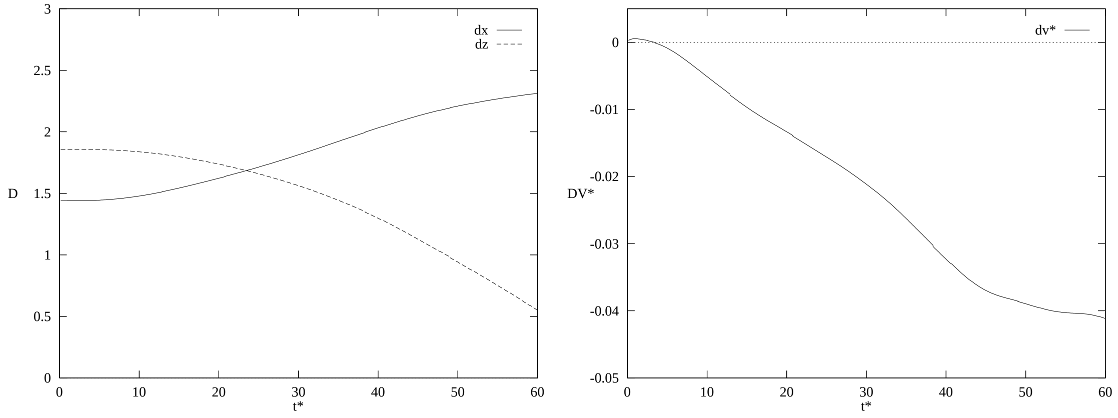

(c) Separation distance

(d) Velocity difference

Figure 3.36: Quantitative description of the two-bubble interaction in Figures 3.33, 3.34 and 3.35. (*a*) Migration velocity versus time. (*b*) z component of the centroid of bubbles versus time. (*c*) The separation distance versus time and (*d*) The velocity difference versus time between the bubble on the right and the left. Velocity is scaled by reference velocity U_r, separation distance and z axis by a, and time by a/U_r.

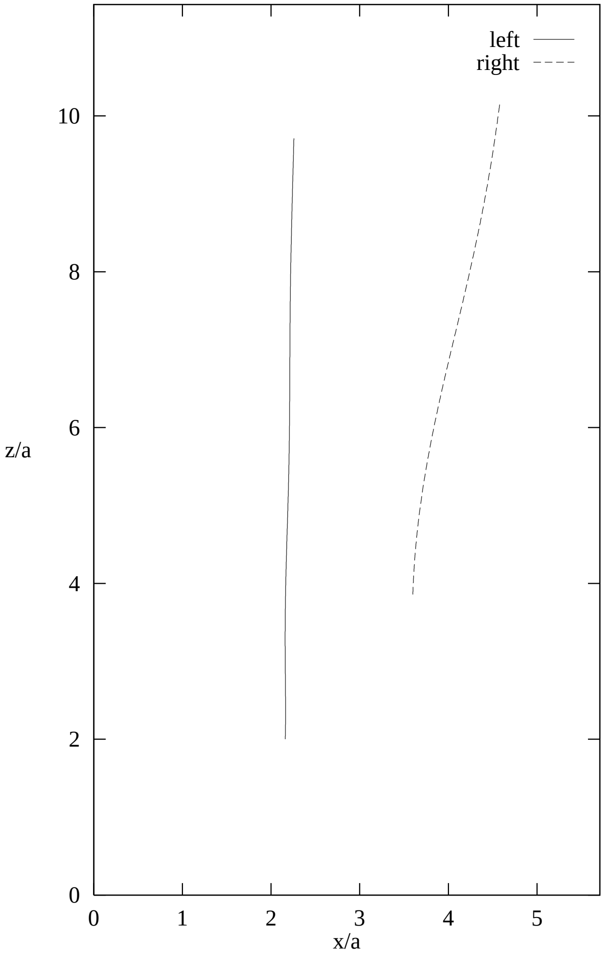

Figure 3.37: Trajectories of the center of mass of the bubbles. Both axis are scaled by the bubble radius a.

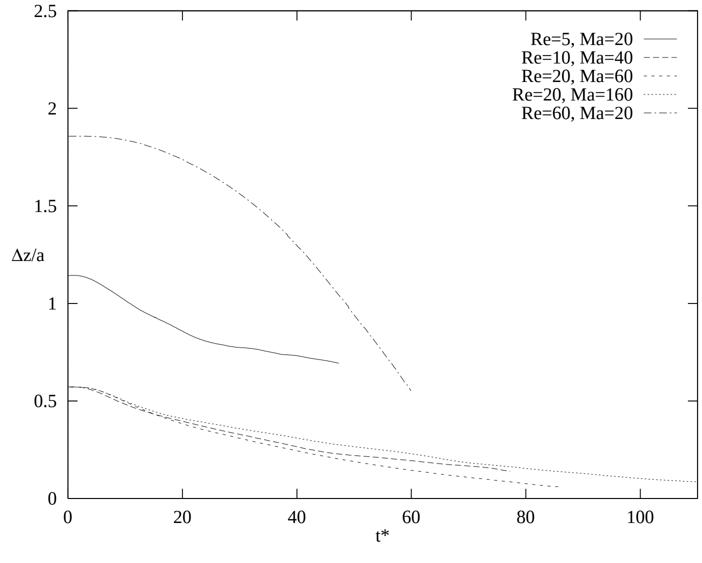

(a) The vertical separation distance

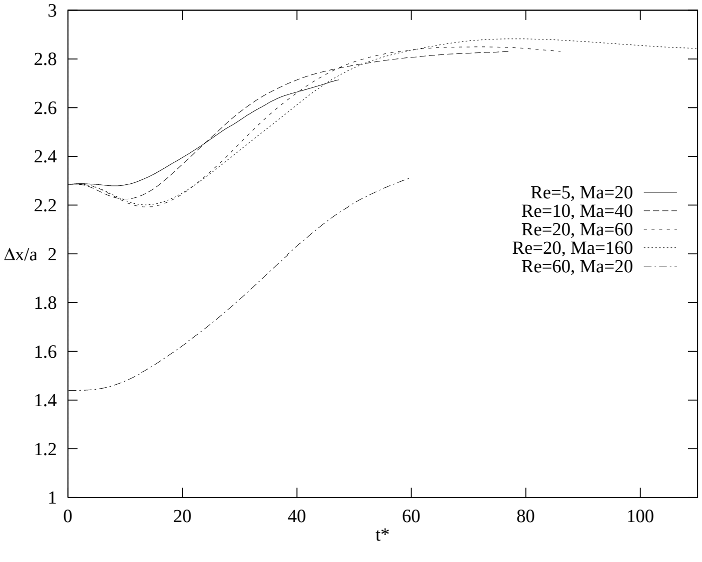

(b) The horizontal separation distance

Figure 3.38: Quantitative information for two-bubble interaction for different Reynolds and Marangoni numbers. (*a*) The vertical separation distance versus time. (*b*) The horizontal separation distance versus time. Time is scaled by a/U_r, separation difference, Δ, by, a. The differences are between the bubble on the right and the bubble on the left.

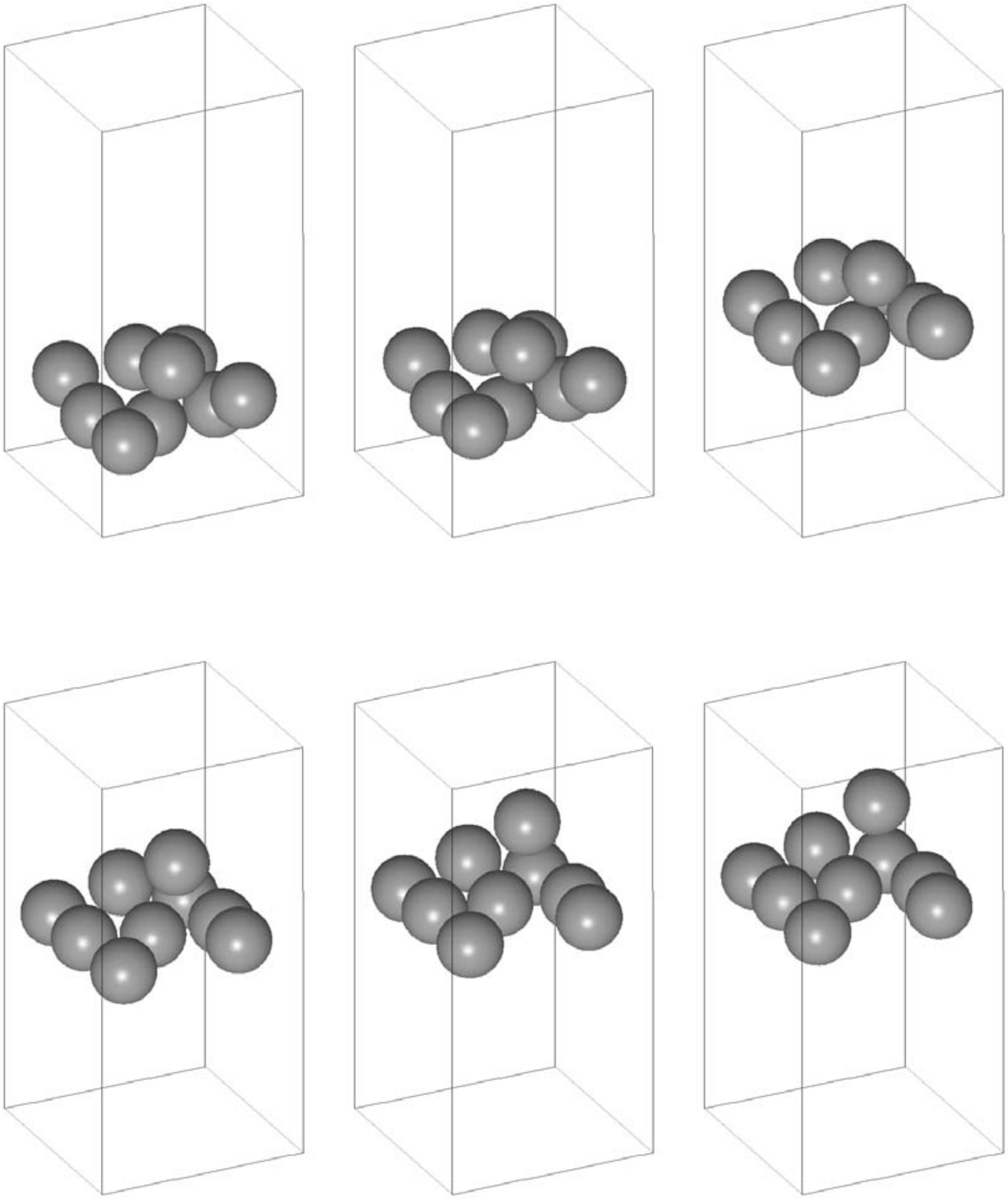

Figure 4.10: A fully three-dimensional simulation of the interaction of nine equal sized bubbles. Time progresses from left to right, top to bottom. The nondimensional time, t^*, is equal to 0.66, 6.66, 40, 66.66, 80, 86.66. The nondimensional time is scaled by a/U_r and velocity is scaled by reference velocity, U_r. Computational domain size is $x/a = 6.66$, $y/a = 6.66$ and $z/a = 13.33$.

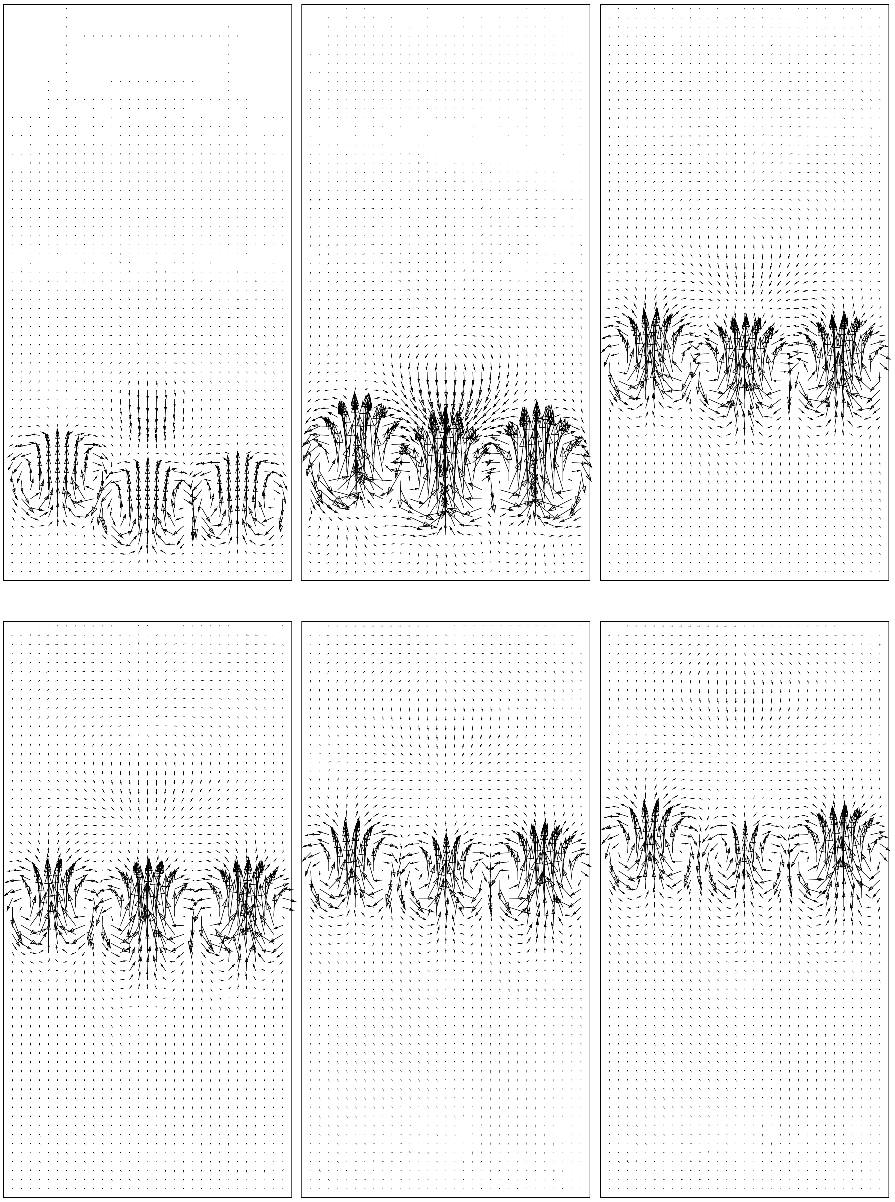

Figure 4.11: Velocity field for selected frames from the fully three dimensional simulation of nine-bubble interaction. The velocity field is shown at every other grid point in the middle plane of the computational box in y direction. Time progresses from left to right. The nondimensional time, t^*, is equal to 0.66, 6.66, 40, 66.66, 80, 86.66. The nondimensional time is scaled by a/U_r and velocity is scaled by reference velocity, U_r. Computational domain size is $x/a = 6.66$, $y/a = 6.66$ and $z/a = 13.33$.

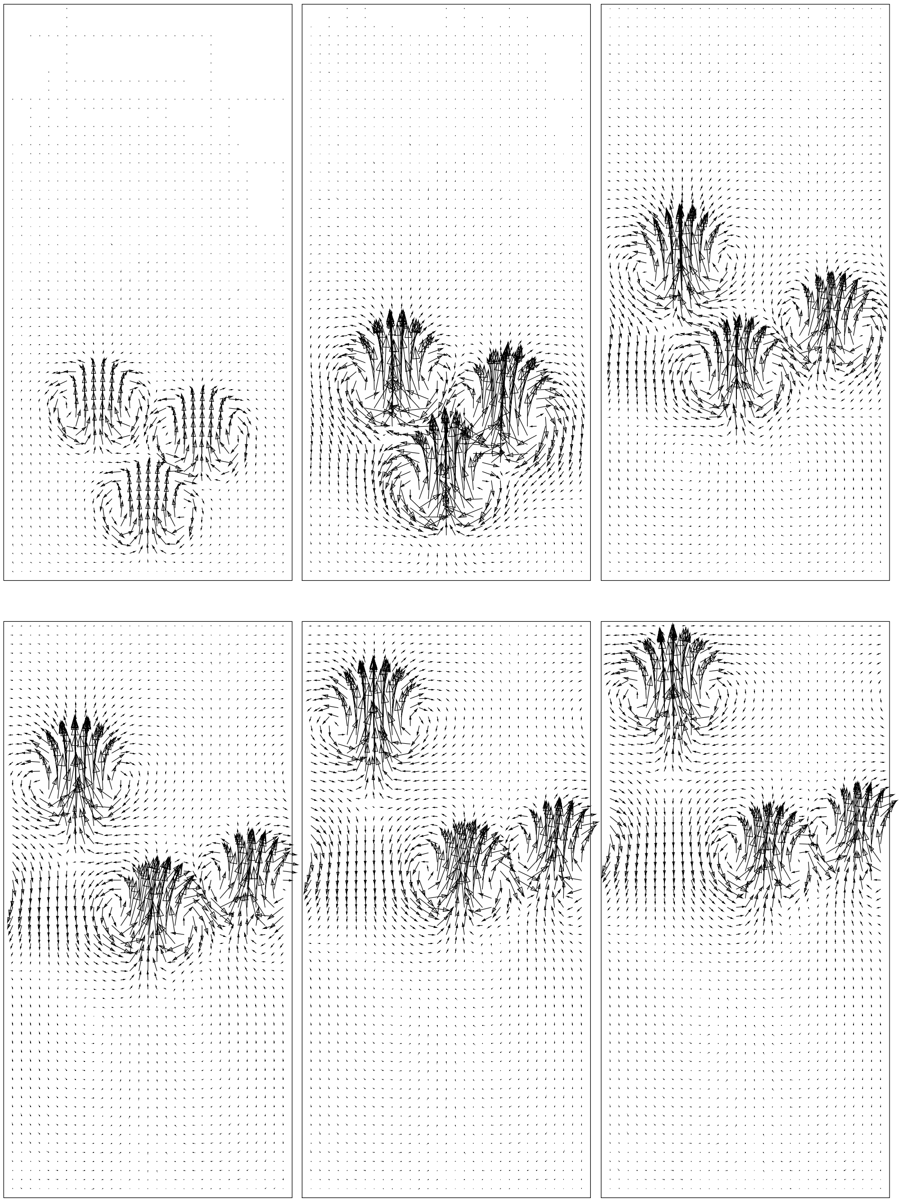

Figure 4.12: Velocity field for selected frames from the fully three dimensional simulation of nine-bubble interaction. The velocity field is shown at every other grid point in the middle plane of the computational box in x direction. Time progresses from left to right. The nondimensional time, t^*, is equal to 0.66, 6.66, 40, 66.66, 80, 86.66. The nondimensional time is scaled by a/U_r and velocity is scaled by reference velocity, U_r. Computational domain size is $x/a = 6.66$, $y/a = 6.66$ and $z/a = 13.33$.

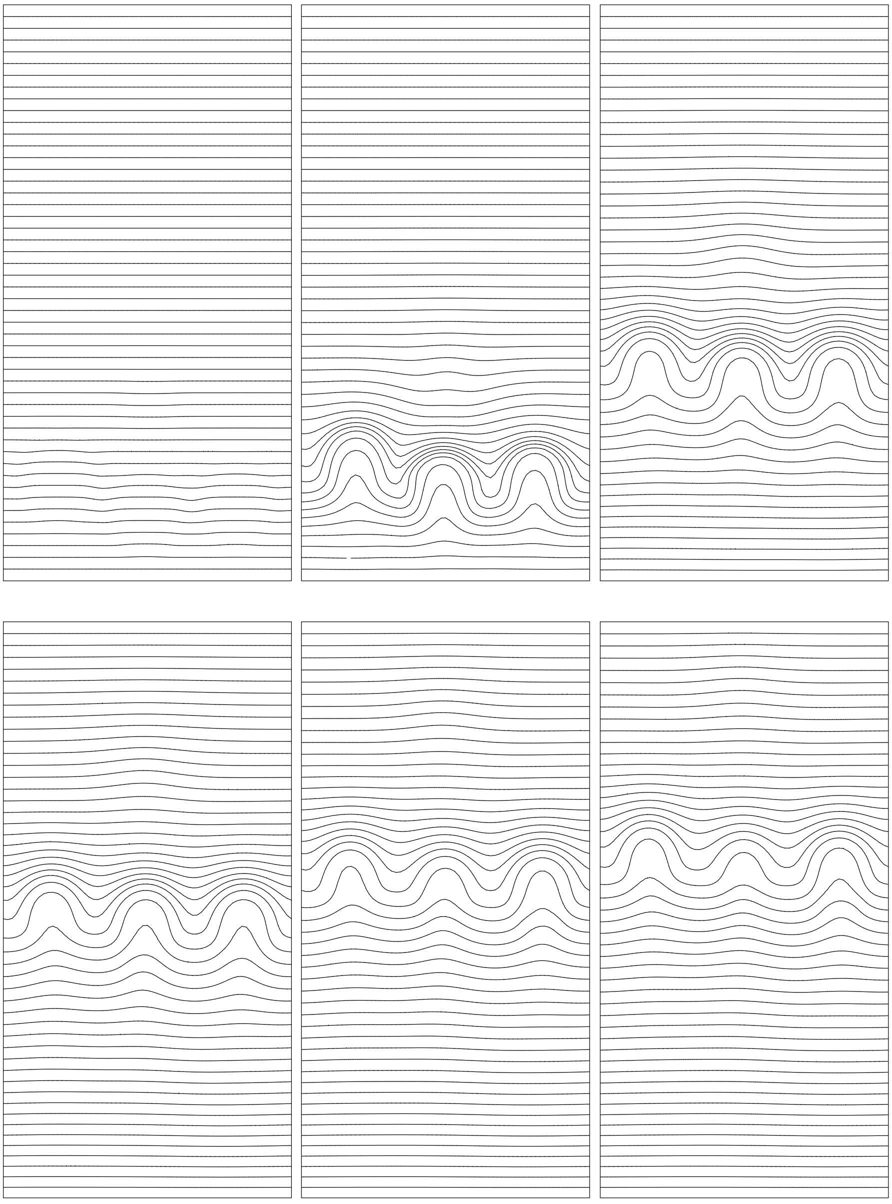

Figure 4.13: Temperature contours for selected frames from the fully three dimensional simulation of nine-bubble interaction. 50 equally spaced contours are shown in the middle plane of the computational box in y direction. Time progresses from left to right. The nondimensional time, t^*, is equal to 0.66, 6.66, 40, 66.66, 80, 86.66. The nondimensional time is scaled by a/U_r and temperature is scaled, after subtracting a reference temperature, by $a\nabla T_\infty$. Computational domain size is $x/a = 6.665$ $y/a = 6.66$ and $z/a = 13.33$.

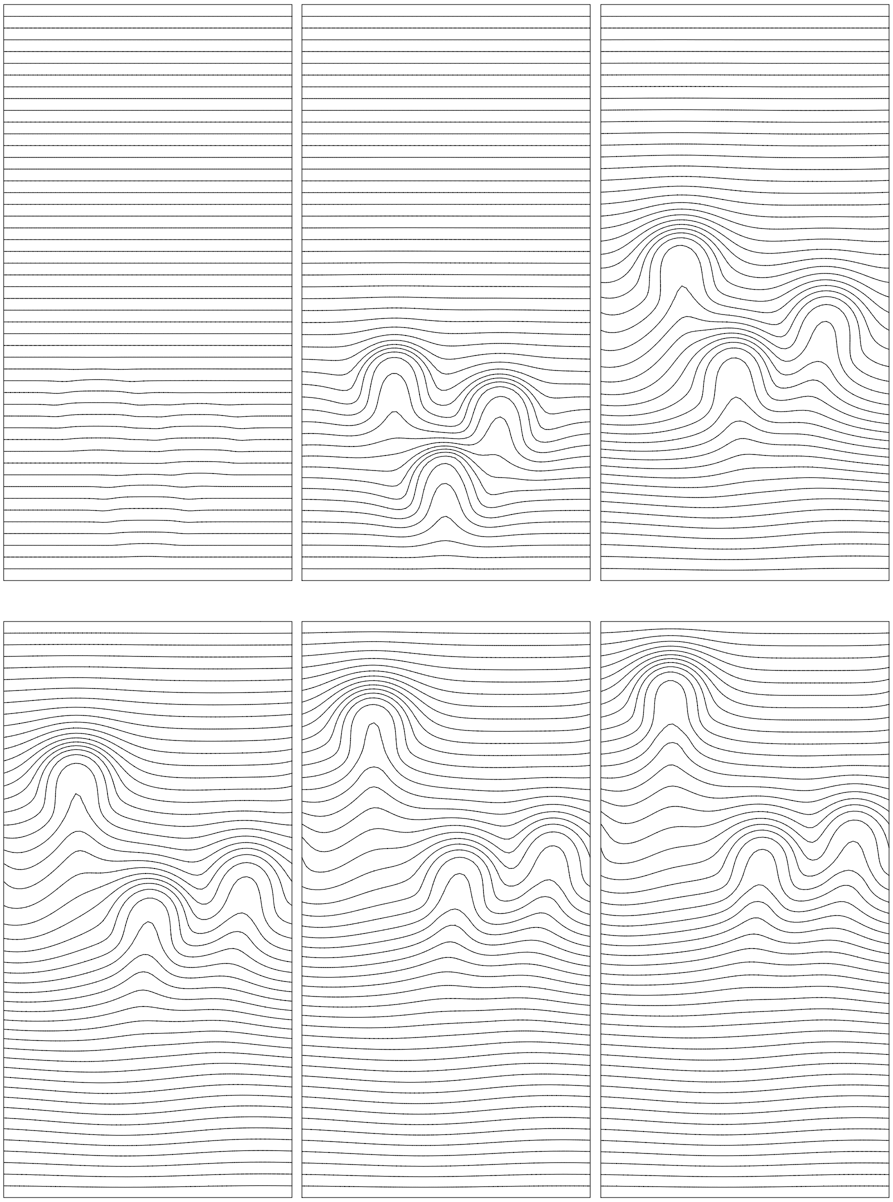

Figure 4.14: Temperature contours for selected frames from the fully three dimensional simulation of nine-bubble interaction. 50 equally spaced contours are shown in the middle plane of the computational box in x direction. Time progresses from left to right. The nondimensional time, t^*, is equal to 0.66, 6.66, 40, 66.66, 80, 86.66. The nondimensional time is scaled by a/U_r and temperature is scaled, after subtracting a reference temperature, by $a\nabla T_\infty$. Computational domain size is $x/a = 6.66$, $y/a = 6.66$ and $z/a = 13.33$.

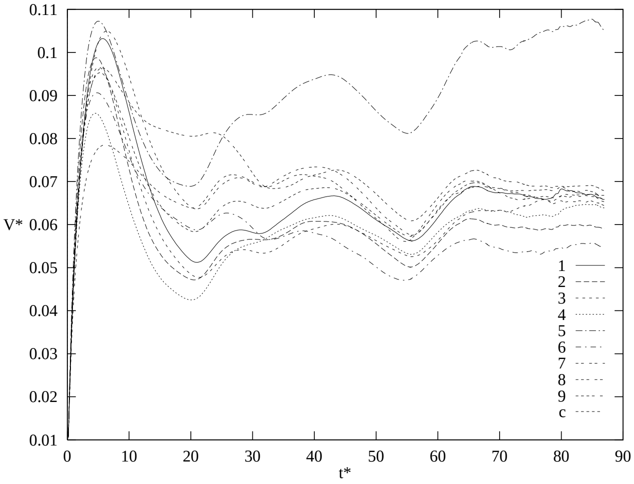

(a) Migration velocity

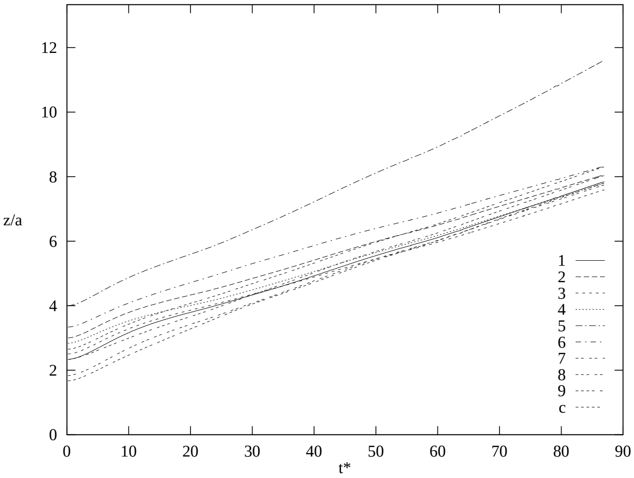

(b) Vertical position

Figure 4.15: (a) Migration velocity versus time (b) z component of the centroid of bubbles versus time, for nine-bubble simulation in Figure 4.10. Velocity is scaled by U_r, time by a/U_r and z axis by a.

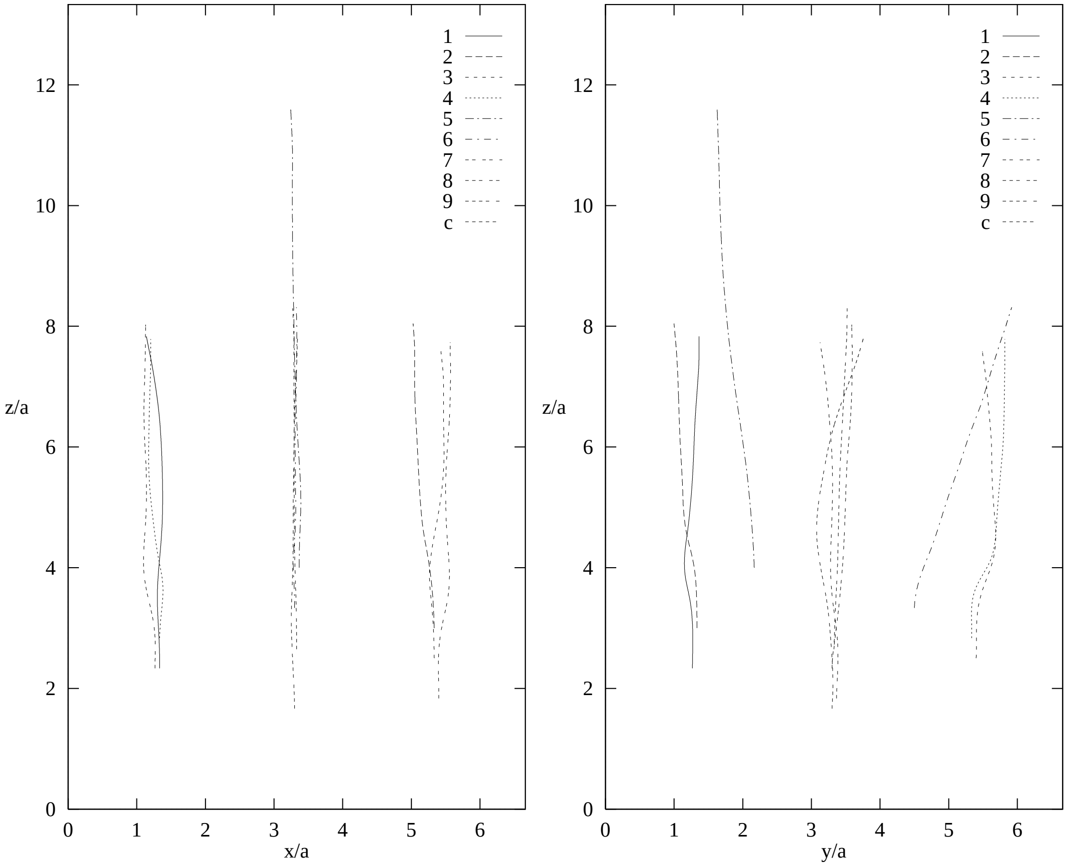

Figure 4.16: (a) $x - z$ trajectories of the center of mass of the bubbles (left). (b) $y - z$ trajectories of the center of mass of the bubbles (right). Both axis are scaled by the bubble radius a.

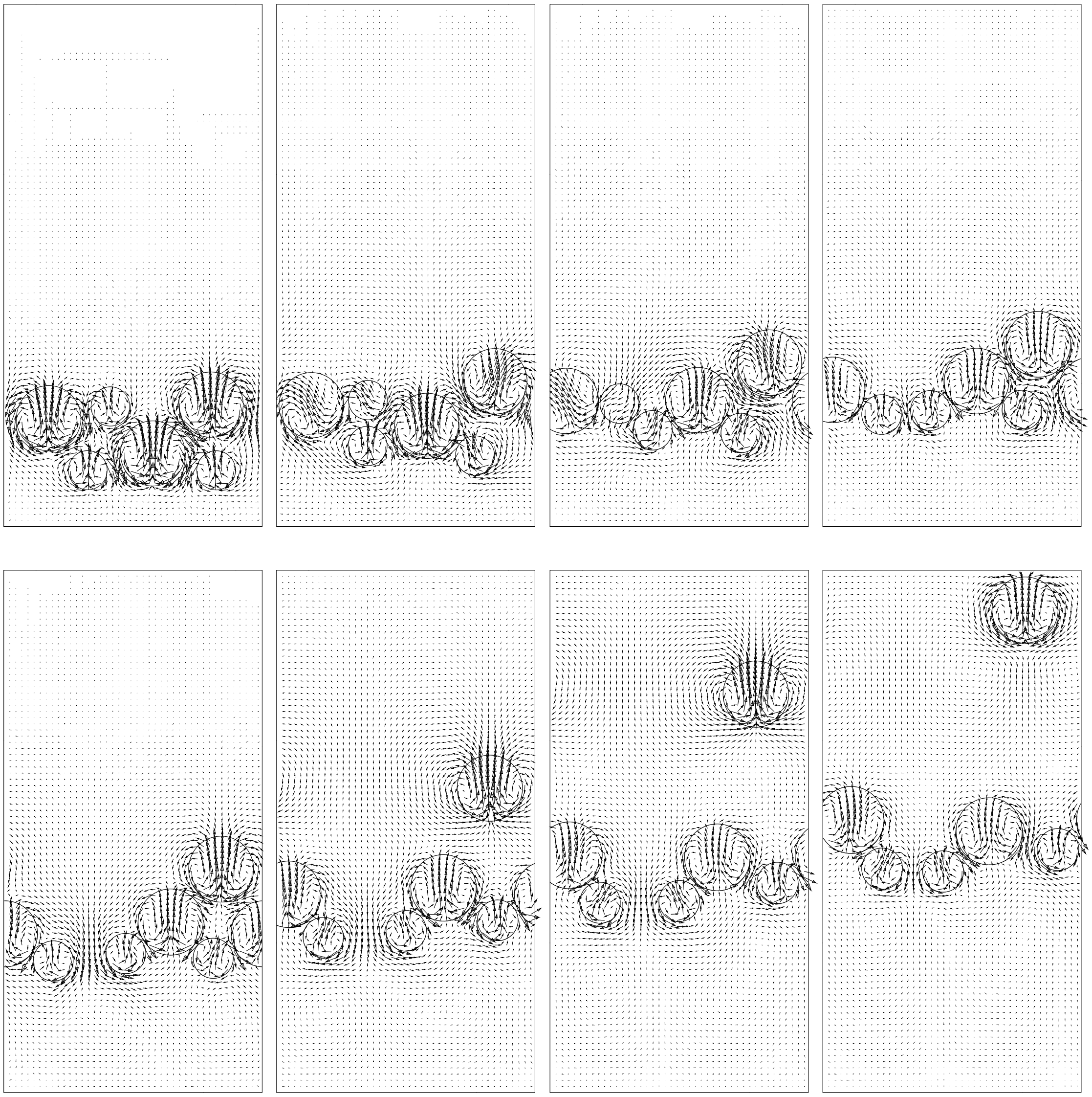

Figure 4.17: Velocity field for selected frames from the computation of six unequal-sized-bubble interaction. Third of the velocity field is shown at every third grid point. Time progresses from left to right. The nondimensional time, t^*, is equal to $2.5, 12.5, 25, 40, 62.5, 87.5, 112.5, 137.5$. The nondimensional time is scaled by a_v/U_{rv} and velocity is scaled by reference velocity, U_{rv}. Computational domain size is $x/a_v = 10$ and $z/a_v = 20$.

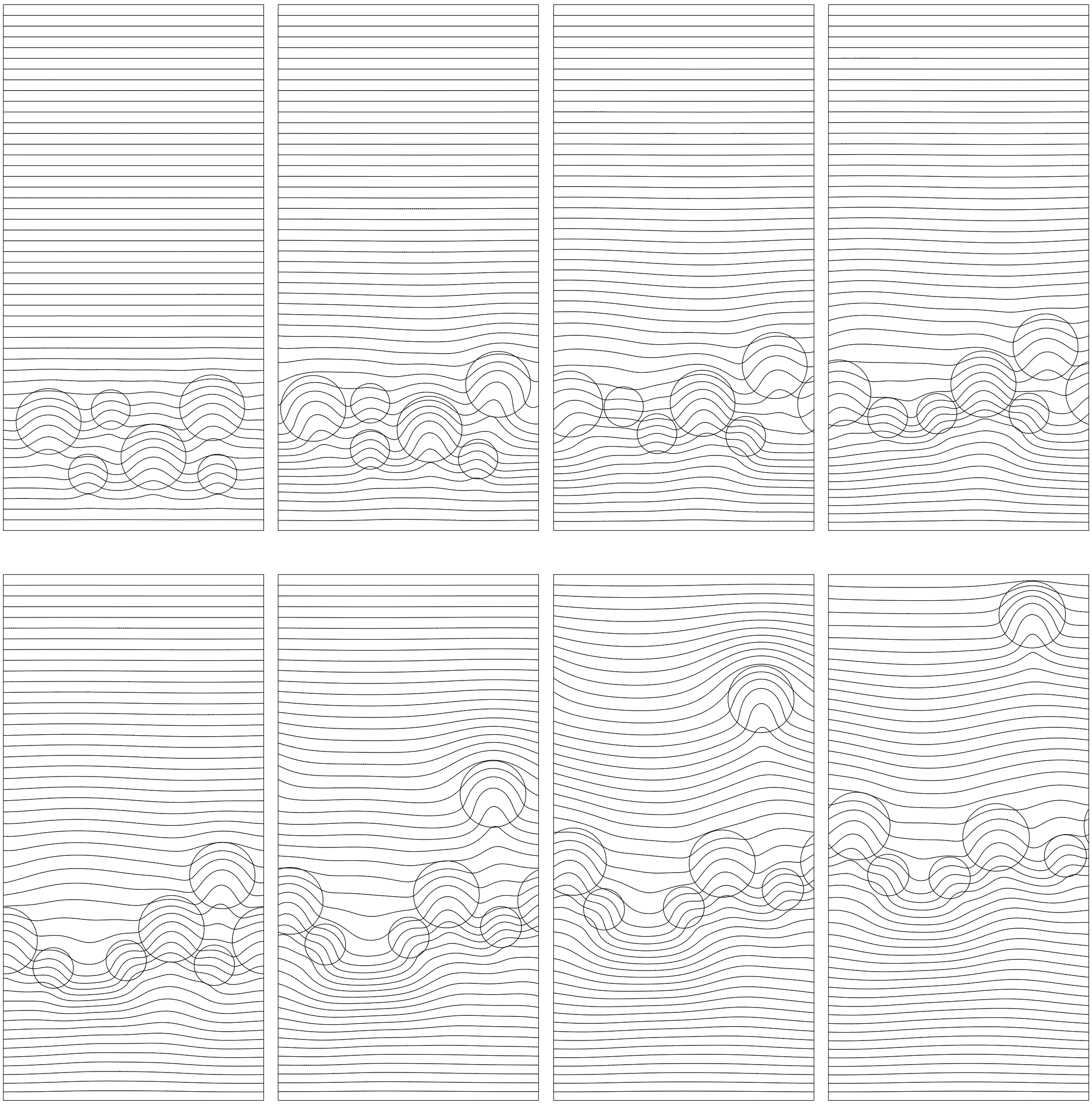

Figure 4.18: Temperature contours for selected frames from the computation of six unequal-sized-bubble interaction. 50 equally spaced contours are shown. Time progresses from left to right. The nondimensional time, t^*, is equal to $2.5, 12.5, 25, 40, 62.5, 87.5, 112.5, 137.5$. The nondimensional time is scaled by a_v/U_{rv} and temperature is scaled, after subtracting a reference temperature, by $a_v \nabla T_\infty$. Computational domain size is $x/a_v = 10$ and $z/a_v = 20$.

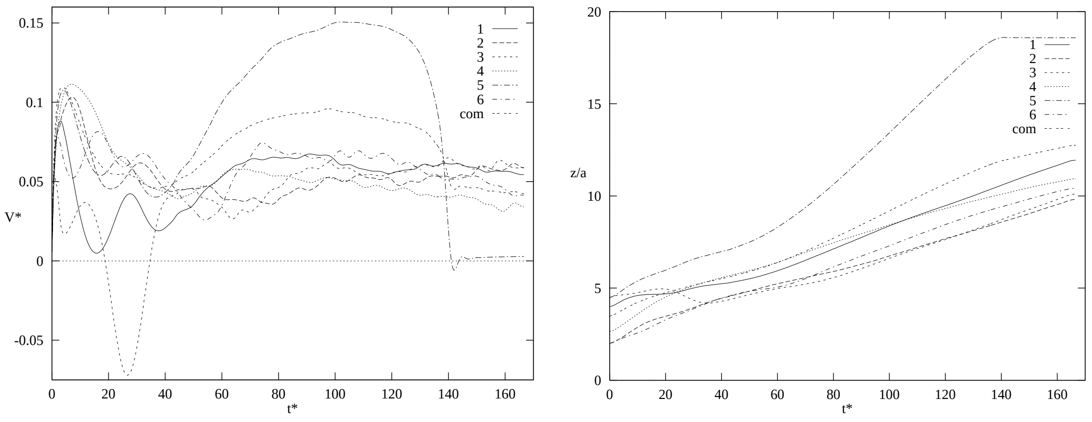

(a) Migration velocity

(b) z component of the centroid of bubbles

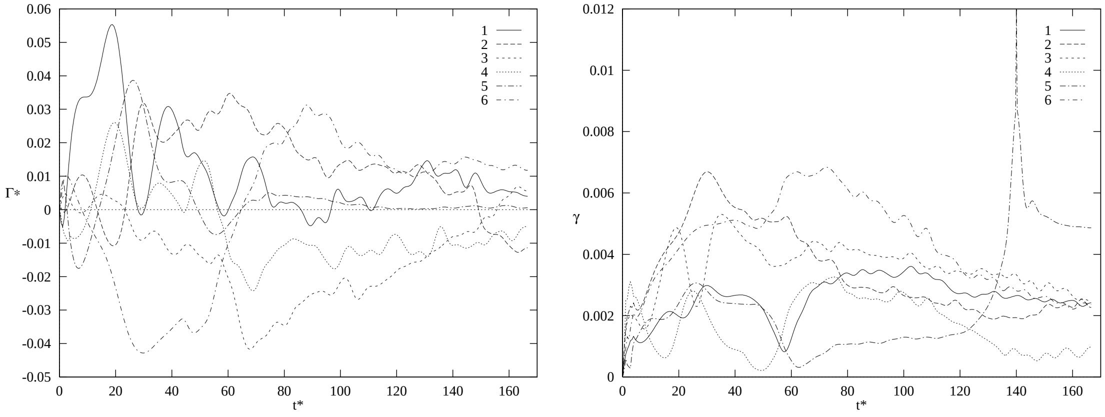

(c) Internal circulation

(d) Deformation

Figure 4.19: Quantitative description of the six unequal-sized-bubble interaction in Figures 4.17 and 4.18. (a) Migration velocity versus time. (b) z component of the centroid of bubbles versus time. (c) Internal circulation versus time. (d) Deformation versus time. Velocity is scaled by U_{rv}, z axis by the averaged bubble radius, a_v, time by a_v/U_{rv}, and the internal circulation by $2\pi a_v U_{rv}$. Bubbles marked 1 to 6 from left to right in the domain. Com is the velocity of the center of mass.

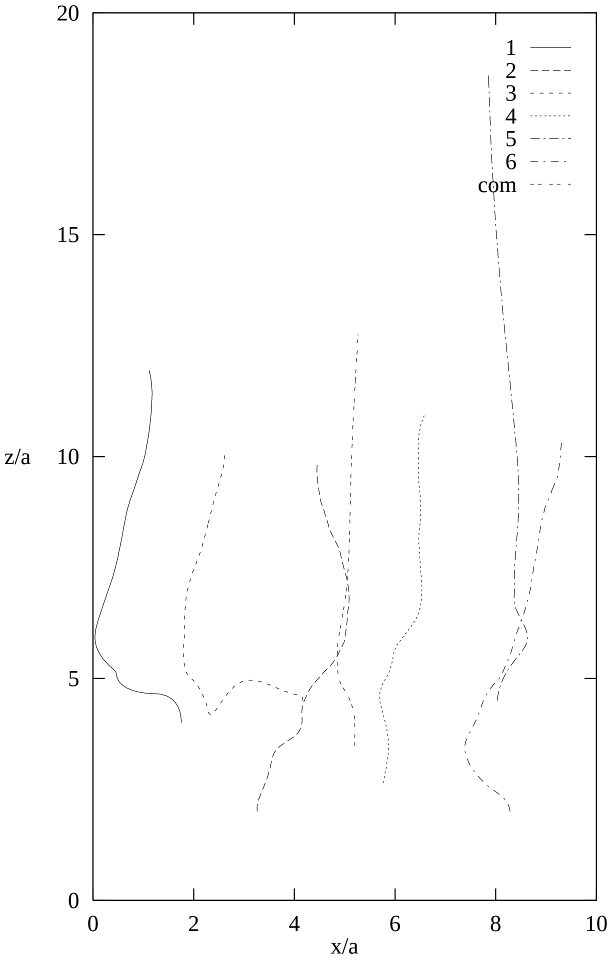

Figure 4.20: Trajectories of the center of mass of the bubbles. Both axis are scaled by the average bubble radius a_v.

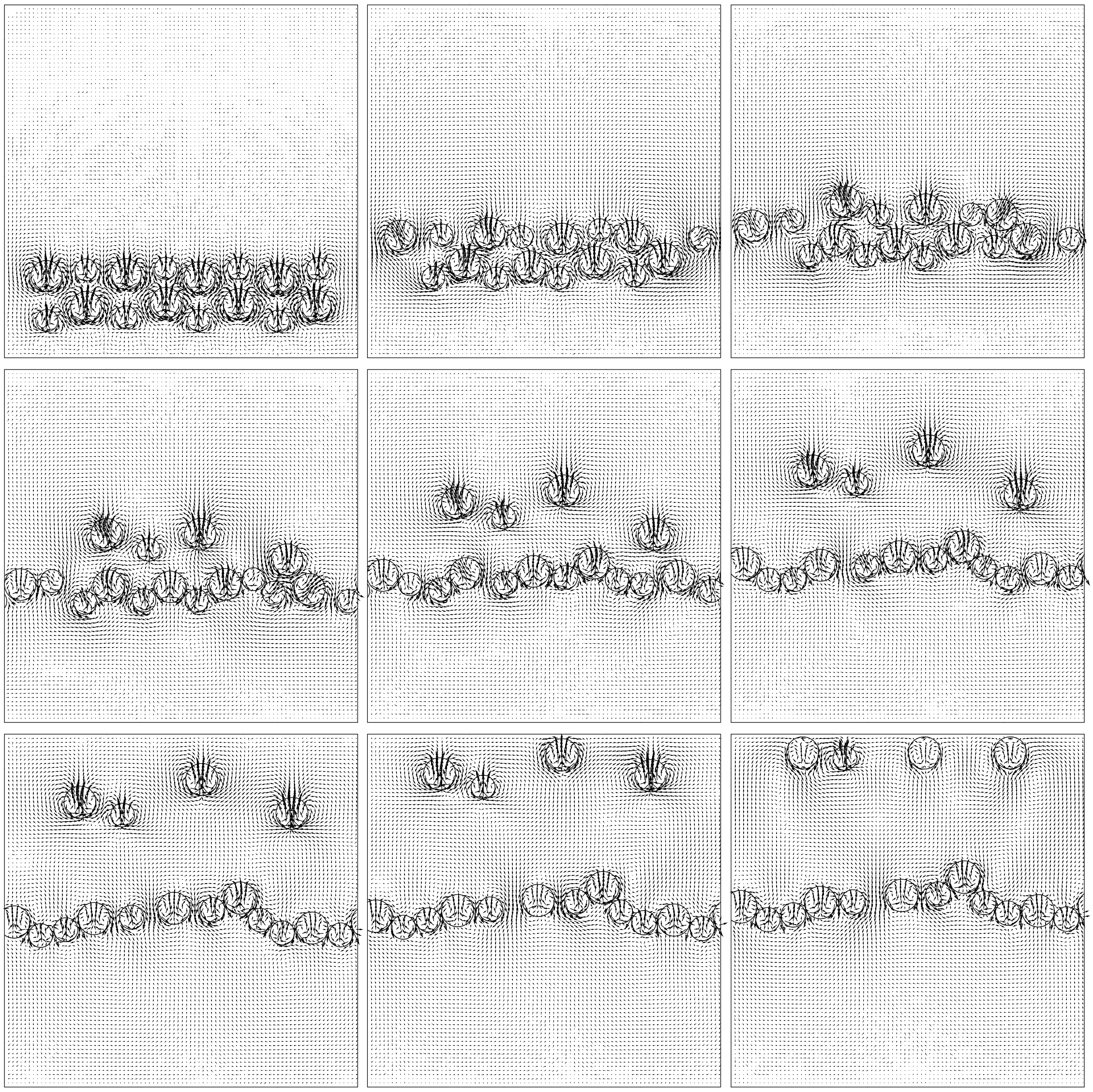

Figure 4.21: Velocity field for selected frames from the simulation of 16 unequal-sized bubble interaction. The velocity field is shown at every third grid point. Time progresses from left to right, top to bottom. The nondimensional time, t^*, is equal to 4, 40.5, 64.7, 89, 113.3, 137.6, 161.9, 182, 202.4. The nondimensional time is scaled by a_v/U_{rv} and velocity by U_{rv}. Computational domain size is $x/a_v = 13.33$ and $z/a_v = 13.33$.

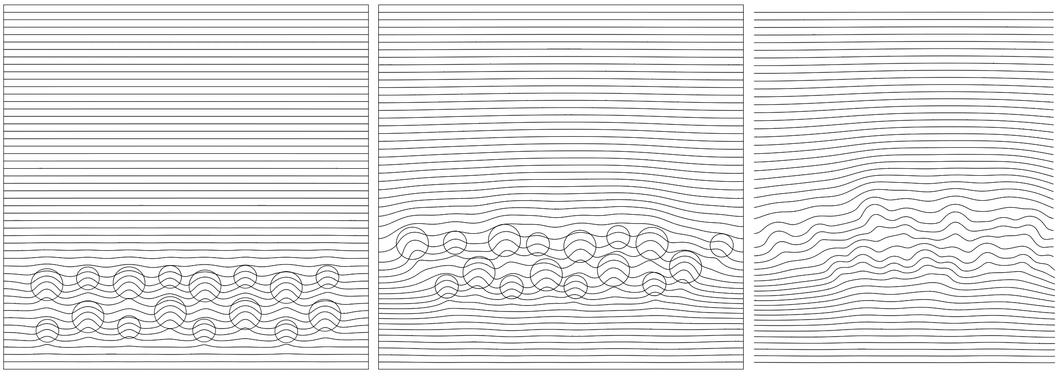

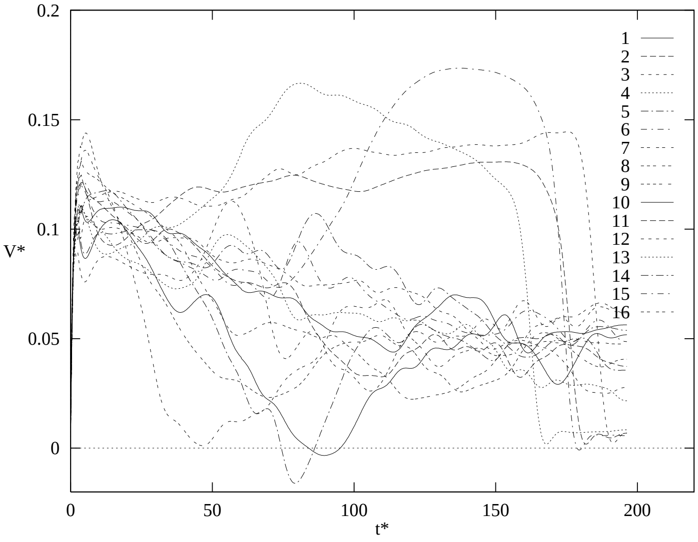

(a) Migration velocity

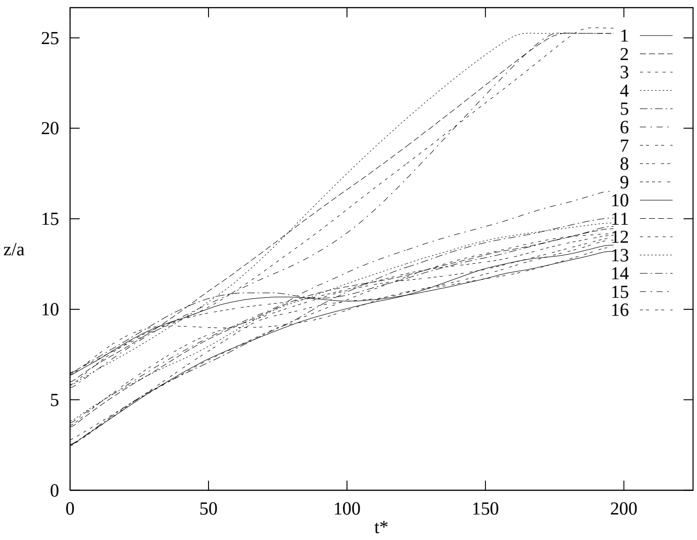

(b) z component of the centroid of bubbles

Figure 4.23: (a) Migration velocity versus time (b) z component of the centroid of bubbles versus time for 16 unequal-sized bubble interaction in Figures 4.21 and 4.22. Velocity is scaled by U_{rv}, time by a_v/U_{rv} and z axis by a_v.

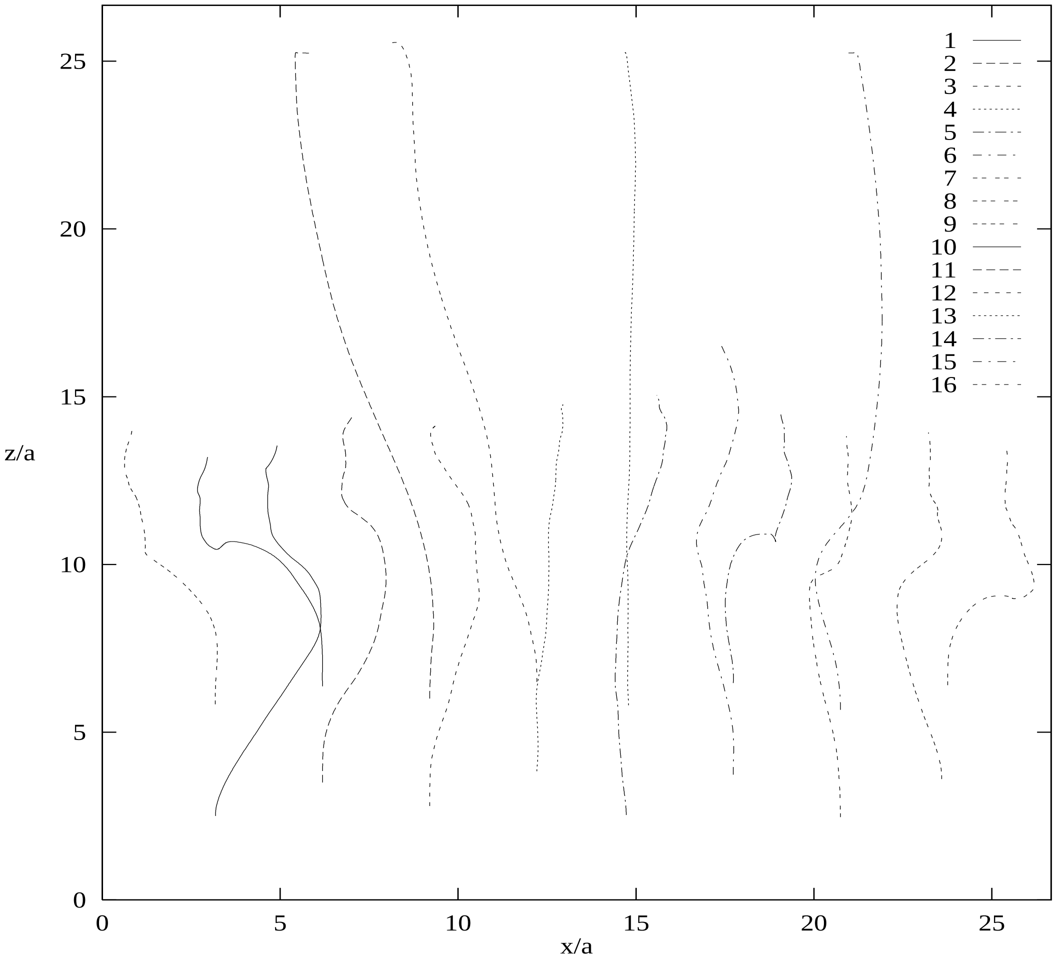

Figure 4.24: Trajectories of the center of mass of the bubbles. Both axis are scaled by the average bubble radius a_v.

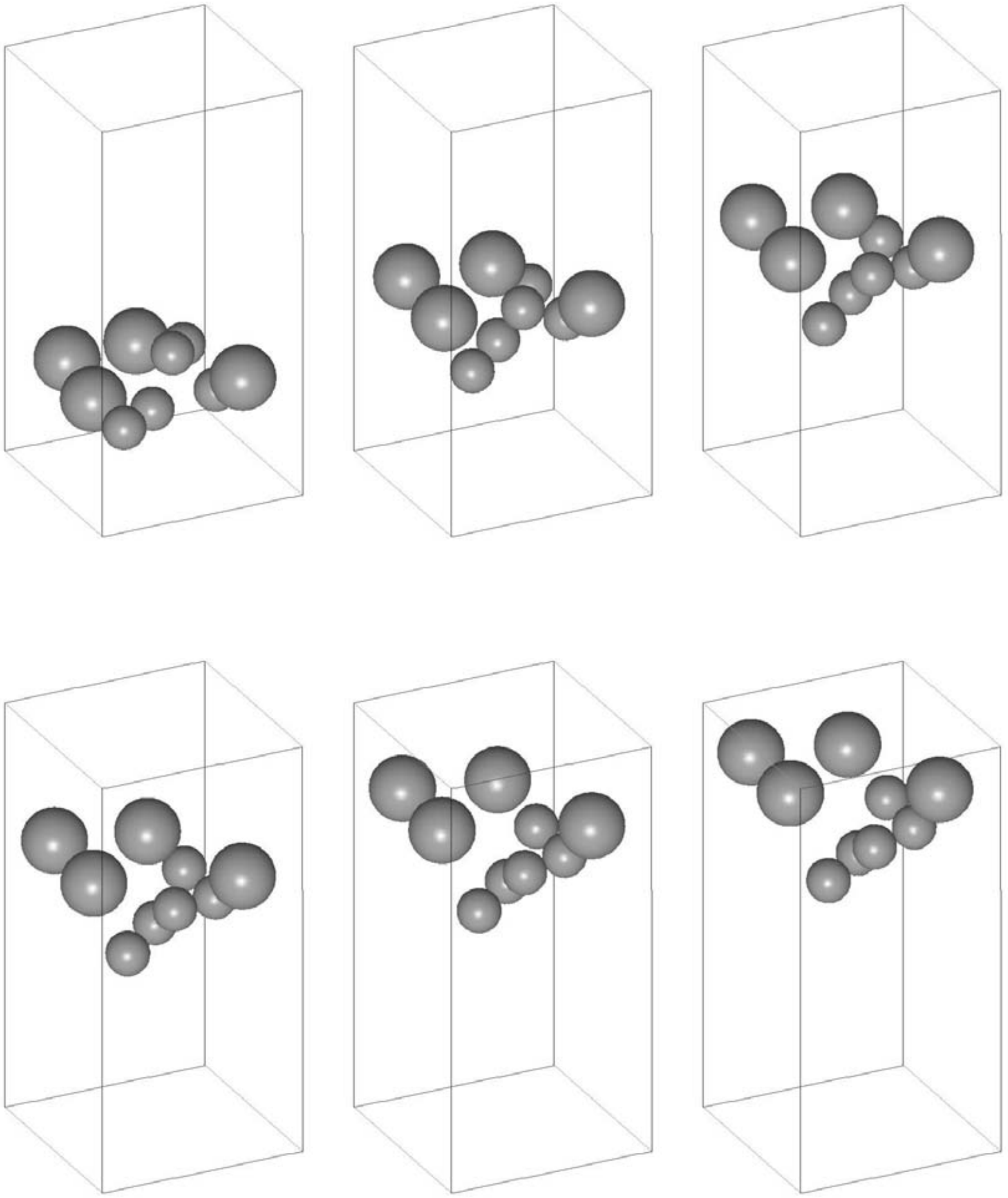

Figure 4.25: A fully three-dimensional simulation of the interaction of nine unequal-sized bubbles. Time progresses from left to right, top to bottom. The nondimensional time, t^*, is equal to 6.66, 40, 66.66, 80, 100, 114.2. The nondimensional time is scaled by a_v/U_{rv} and velocity is scaled by average reference velocity, U_{rv}. Computational domain size is $x/a_v = 8$, $y/a_v = 8$ and $z/a_v = 16$.

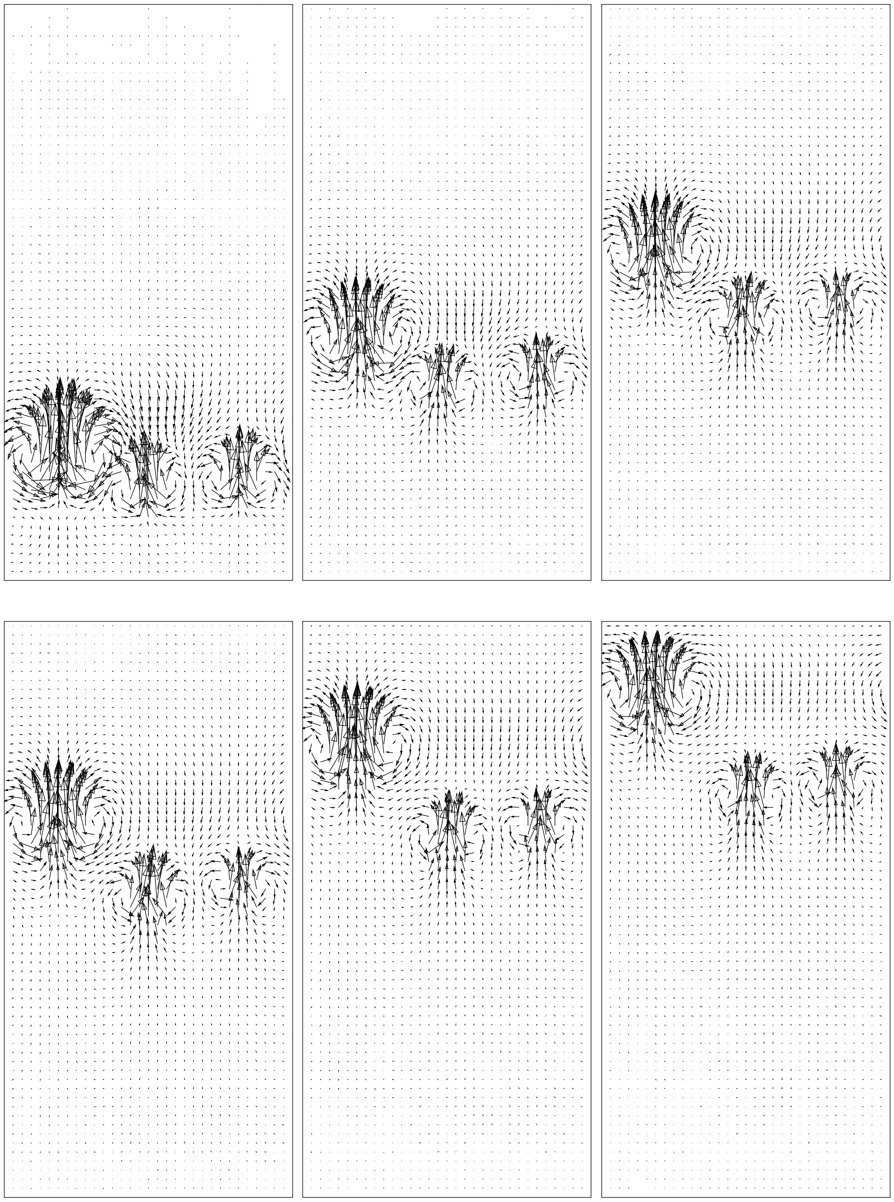

Figure 4.26: Velocity field for selected frames from the fully three dimensional simulation of nine unequal-sized bubble interaction. The velocity field is shown at every other grid point in the middle plane of the computational box in y direction. Time progresses from left to right. The nondimensional time, t^*, is equal to 6.66, 40, 66.66, 80, 100, 114.2. The nondimensional time is scaled by a_v/U_{rv} and velocity is scaled by average reference velocity, U_{rv}. Computational domain size is $x/a_v = 8$, $y/a_v = 8$ and $z/a_v = 16$.

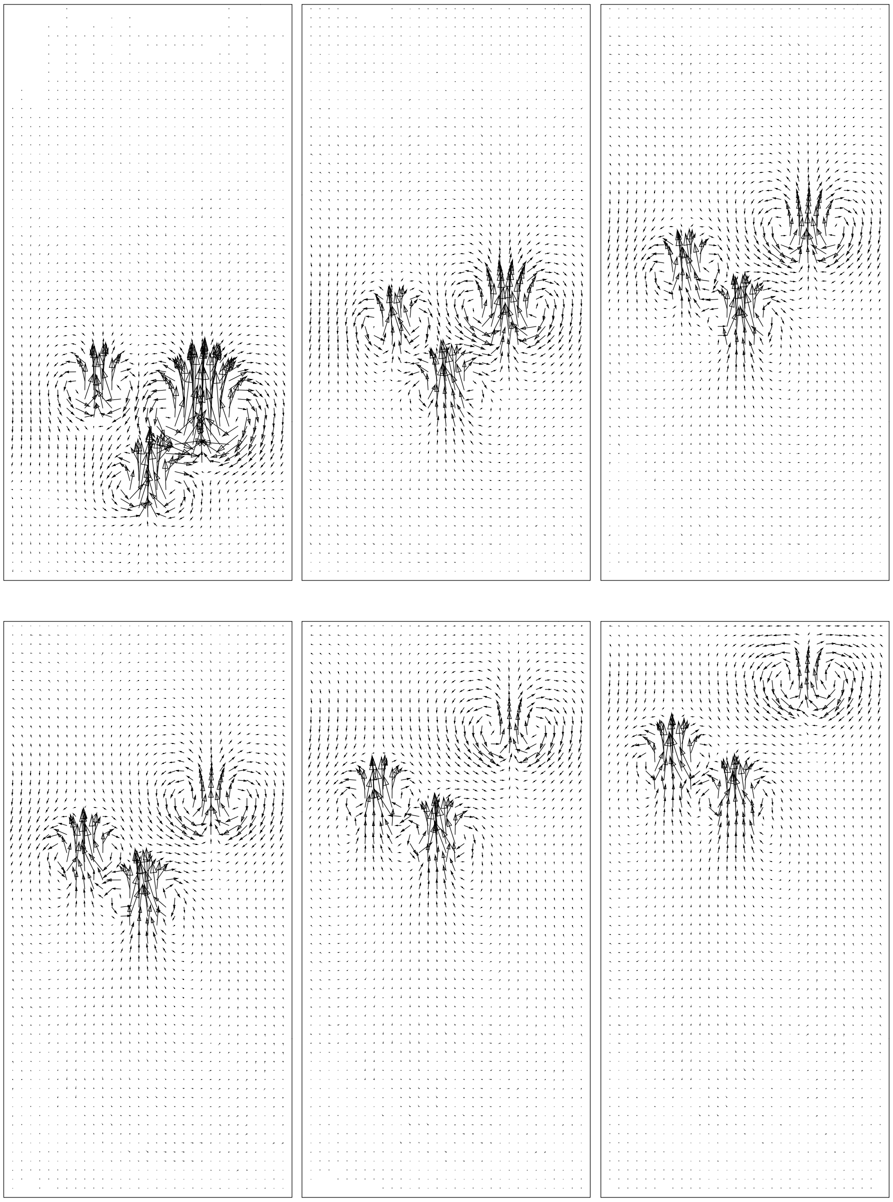

Figure 4.27: Velocity field for selected frames from the fully three dimensional simulation of nine unequal-sized bubble interaction. The velocity field is shown at every other grid point in the middle plane of the computational box in x direction. Time progresses from left to right. The nondimensional time, t^*, is equal to 6.66, 40, 66.66, 80, 100, 114.2. The nondimensional time is scaled by a_v/U_{rv} and velocity is scaled by average reference velocity, U_{rv}. Computational domain size is $x/a_v = 8$, $y/a_v = 8$ and $z/a_v = 16$.

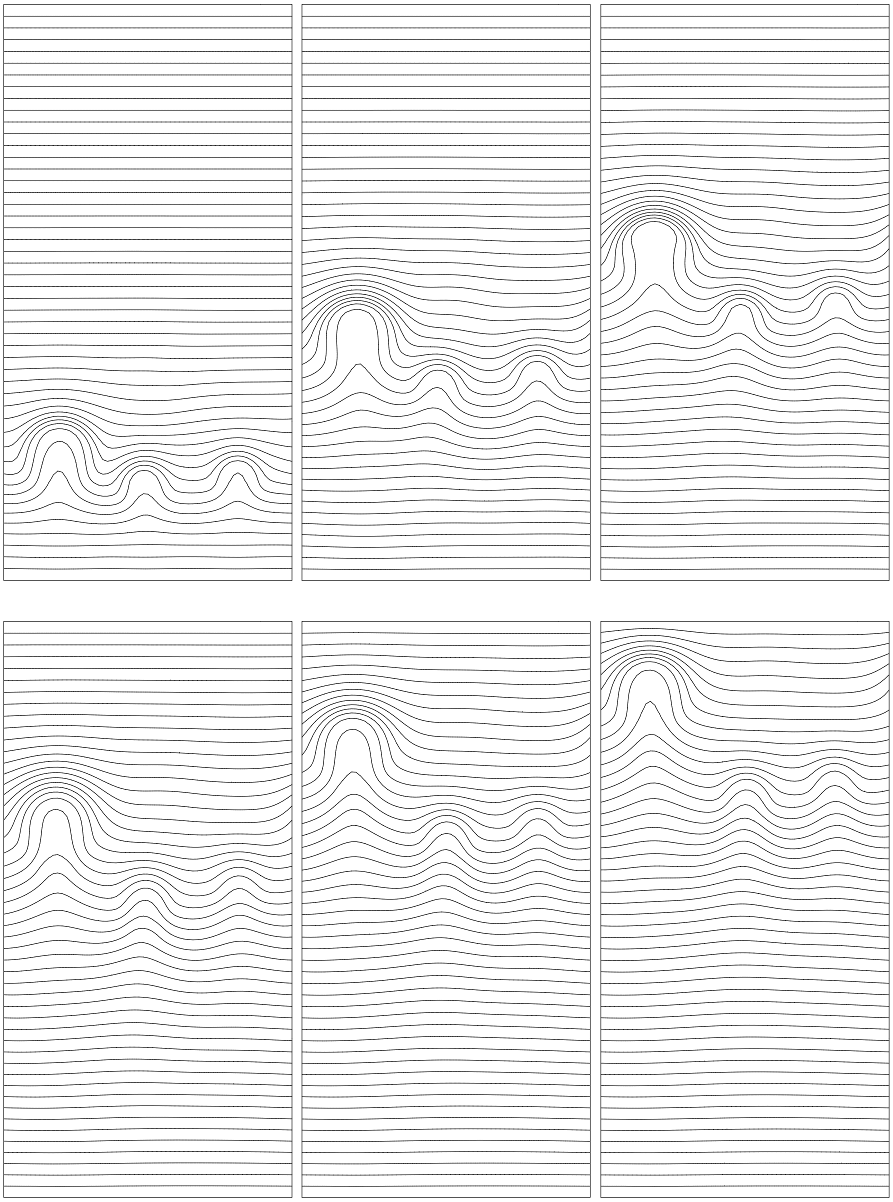

Figure 4.28: Temperature contours for selected frames from the fully three dimensional simulation of nine unequal-sized bubble interaction. 50 equally spaced contours are shown in the middle plane of the computational box in y direction. Time progresses from left to right. The nondimensional time, t^*, is equal to 6.66, 40, 66.66, 80, 100, 114.2. The nondimensional time is scaled by a_v/U_{rv} and temperature is scaled, after subtracting a reference temperature, by $a_v \nabla T_\infty$. Computational domain size is $x/a_v = 8$, $y/a_v = 8$ and $z/a_v = 16$.

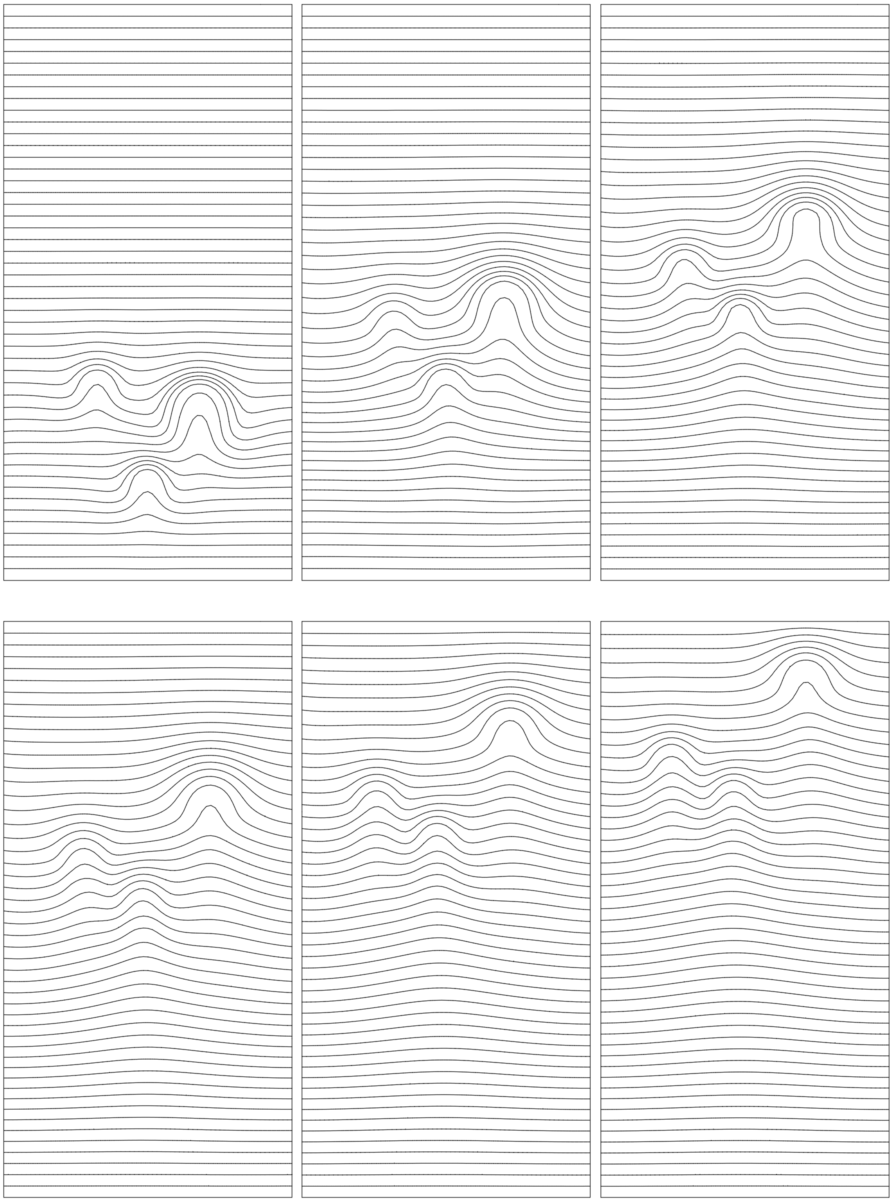

Figure 4.29: Temperature contours for selected frames from the fully three dimensional simulation of nine unequal-sized bubble interaction. 50 equally spaced contours are shown in the middle plane of the computational box in x direction. Time progresses from left to right. The nondimensional time, t^*, is equal to 6.66, 40, 66.66, 80, 100, 114.2. The nondimensional time is scaled by a_v/U_{rv} and temperature is scaled, after subtracting a reference temperature, by $a_v \nabla T_\infty$. Computational domain size is $x/a_v = 8$, $y/a_v = 8$ and $z/a_v = 16$.

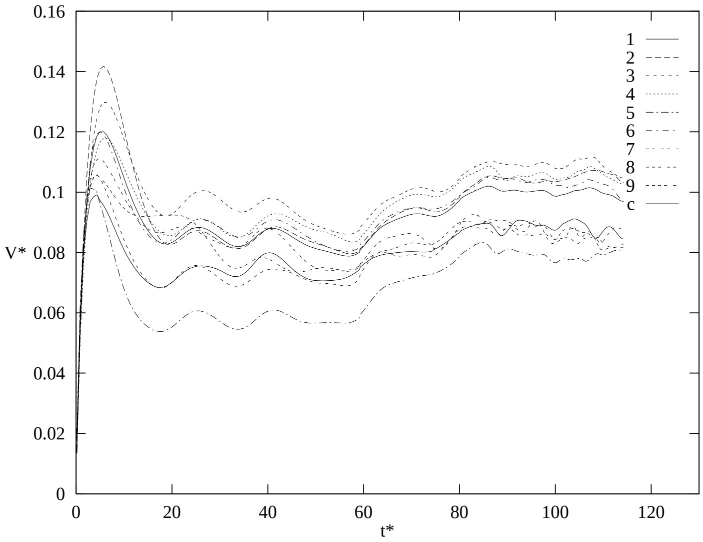

(a) Migration velocity

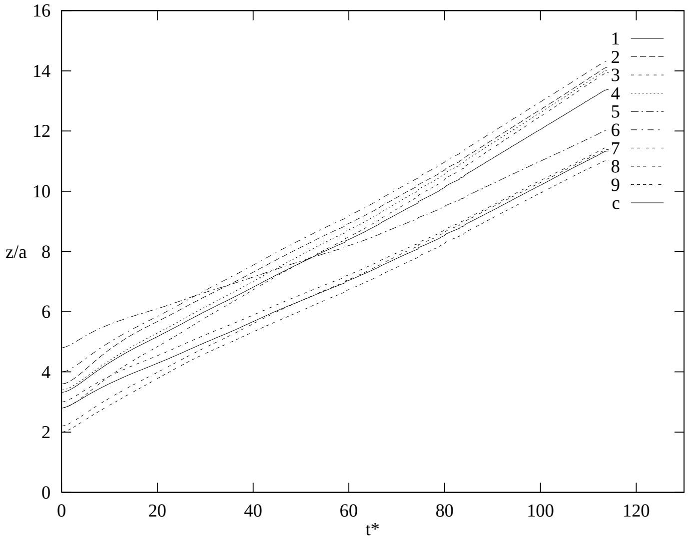

(b) Vertical position

Figure 4.30: (a) Migration velocity versus time (b) z component of the centroid of bubbles versus time, for 9 unequal-sized-bubble simulation. Velocity is scaled by U_{rv}, time by a_v/U_{rv} and z axis by average bubble radius, a_v. Even numbered bubbles are the larger ones.

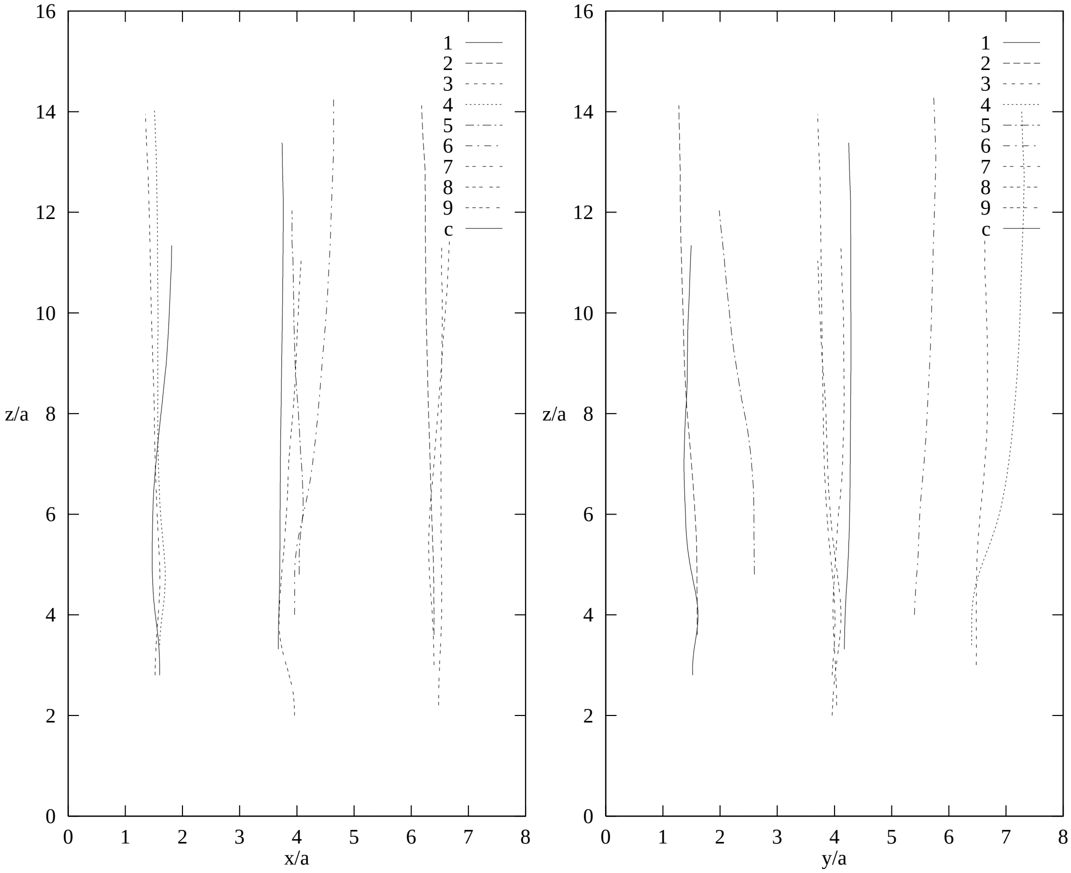

Figure 4.31: (a) $x-z$ trajectories of the center of mass of the bubbles (left). (b) $y-z$ trajectories of the center of mass of the bubbles (right). Both axis are scaled by the average bubble radius, a_v.

CHAPTER V

CONCLUSIONS

5.1 Conclusions

In this thesis, we have examined thermocapillary migration of bubbles and drops in zero gravity by full numerical simulations. We have extended the front tracking method developed by Unverdi and Tryggvason (1992) to include the energy equation as well as temperature dependent surface tension. The results have been verified to be quantitatively and qualitatively reliable by comparison with theoretical results.

We studied the thermocapillary migration of a single bubble in Chapter III and confirmed the effect of the governing parameters on the migration velocity, by showing that the migration velocity of the bubble decreases with an increasing Reynolds and Capillary number. Then, we studied the interaction of two bubbles and drops in detail. The major finding of the two-bubble study, reported in Chapter III, is the tendency of the bubbles to line up, side by side, perpendicular to the temperature gradient. This tendency to form bubble layers could be of considerable significance for, for example, material processing in microgravity where layers like these might affect the bulk properties of solidified materials. Drops, on the other hand, behaved somewhat differently. In the low Re and Ma number region, they act similar to bubbles; however, they tend to line up in tandem when both the Re and the Ma

are high. Drops also deform more than bubbles, along the direction of temperature gradient.

In Chapter IV, we examined the behavior of a bubble cloud, for both mono-dispersed and polydispersed cases. The numerical simulations of mono-dispersed systems show that the bubbles form horizontal layers. As soon as the bubbles form one layer that fills the channel horizontally, the rest of the bubbles form another layer. Although we saw, in the two-dimensional sixteen bubble simulation, that this layer can break up by instability waves, the layer is eventually regenerated. Three dimensional simulations confirm the formation of layers while simulation of bubbles in polydispersed systems show the same behavior. In contrast to two dimensional simulations of polydisperse systems, where bubbles of different size form a horizontal layer, a three dimensional simulation of a polydisperse system shows that different sizes of bubbles form different layers. Each layer moves with a different velocity and the larger the bubbles, the higher the migration velocity of each layer. This results in a layer of large bubbles that moves ahead of a layer of small bubbles. While the prominent feature of layer formation is a persistent characteristic in these simulations, only bubbly flows are explored here. In the light of Chapter III, where two dimensional drops were examined, we do not expect drops to form layers at high Re and Ma.

The thermocapillary interactions of two bubbles and drops as well as many bubbles reported in this thesis are the first full simulations calculated at non-zero Reynolds and Marangoni numbers, allowing for full deformations. The computatations presented here represent a significant advance in the state of the art of numerical modeling of thermal migration of bubbles and drops. Previously, no fully three-dimensional simulations have been reported, and only axisymmetric and asymmetric calculations of spherical two-bubble or two-drop interactions have been done by Wei and Subramanian (1993), and Keh and Chen (1993) at zero Reynolds and Marangoni numbers. In additon to advances on the computational side, our results show a previously unknown behaviour for multi bubble systems. No experimental evidence exists yet, but Balasubramaniam (personal communication) and collaborators expect to investigate two bubble behavior on future Space Shuttle flights. The observed layer formation appears to be very robust, and could have important consequenses for both material processing in space as well as thermal management in gas-liquid systems.

5.2 Suggestions for future work

The surface tension between two fluids depends on the properties of both fluids as well as the temperature. In addition, it also depends on adsorbed surface active materials and the electrical charge on the surface. For bubbles where the temperature is not the only factor determining the surface tension, these effects should be included also.

Although it is a good assumption that the surface tension decreases linearly with increasing temperature, the relation is not linear when the temperature varies over a large range. Non-linear relations will be needed to account for this. This could easily be changed in our current code.

Even though the magnitude of the gravity in space is small, it is still on the order of $10^{-5} g\ m/s^2$. The effect of low levels of gravity, where surface tension forces are comparable to buoyancy forces, should be considered. This, again, is easily added to our code.

If the temperature variation in the system considered are not large, the material properties do not depend on temperature. When this requirement is not satisfied, variation of properties with temperature should be taken into account.

Although some polydisperse systems are considered in this thesis, engineering systems usually involve many different-sized bubbles or drops. To simulate such systems by fully resolving the flow field accurately will be a challenging issue for future work. One way of achieving calculations along this lines is to parallelize the code. Although we attempted to do this by using the domain decomposition method, the final code has not been fully tested as yet. This extension, however, has the potential of allowing simulations with as many as 256^3 grid points.

APPENDIX

APPENDIX A

Nomenclature

$Ca = \frac{\mu_o U_r}{\sigma}$	Capillary Number
H	Scaled distance from wall
$Ma = \frac{U_r a}{\alpha_o}$	Marangoni Number
$Re = \frac{\rho_o U_r a}{\mu_o}$	Reynolds Number
U_r	Reference velocity
U_{rv}	Average reference velocity
Q	Total mass flux
a	Bubble radius
a_v	Average bubble radius
c_{pi}	Heat capacity of bubble fluid
c_{po}	Heat capacity of host-fluid
d	distance
k_i	Conductivity of bubble fluid
k_o	Conductivity of host-fluid
$\mathbf{n}$	Normal vector
s	Surface coordinate
$\mathbf{t}$	Tangent vector

t^*	Nondimensional time
$\mathbf{u}$	Velocity vector
u	x-component of velocity
v	y-component of velocity
w	z-component of velocity
x	x-coordinate
x^*	nondimensional domain lenght in x direction
$\mathbf{x_f}$	Position vector of interface
y	y-coordinate
y^*	nondimensional domain lenght in y direction
z	z-coordinate
z^*	nondimensional domain lenght in z direction
x_c	x-coordinate of center of mass of a bubble
y_c	y-coordinate of center of mass of a bubble
z_c	z-coordinate of center of mass of a bubble
Δ	Separation
α	Thermal diffusivity
γ	Deformation
Γ^*	Circulation
δ	Delta function
κ	Curvature
λ	Size ratio of bubbles
μ_i	Viscosity of bubble fluid
μ_o	Viscosity of host-fluid

ν	Kinematic viscosity
ρ_i	Density of bubble fluid
ρ_o	Density of host-fluid
σ	Surface tension coefficient
σ_T	Surface tension gradient with respect to temperature
σ_x	Surface tension gradient with respect to x

BIBLIOGRAPHY

BIBLIOGRAPHY

[1] A. Acrivos, D. J. Jeffrey, and D. A. Saville. Particle Migration in Suspensions by Thermocapillary or Electrophoretic Motion. J. of Fluid Mech. **212** (1990), 95-110.

[2] J. Adams. MUDPACK: Multigrid Fortran Software for the Efficient Solution of Linear Elliptic Partial Differential Equations. Applied Math. and Comput. **34** (1989), 113-146.

[3] J. L. Anderson. Droplet Interaction in Thermocapillary Motion. Int. J. Multiphase Flow **11** (1985), 813-824.

[4] E. P. Ascoli and L. G. Leal. Thermocapillary Motion of a Deformable Drop Toward a Planar Wall. J. Colloid Interface Sci. **138** (1990), 220-230.

[5] R. Balasubramaniam and J. E. Lavery. Numerical Simulation of Thermocapillary Bubble Migration Under Microgravity for Large Reynolds and Marangoni Numbers. Num. Heat Transfer A**16** (1989), 175-187.

[6] R. Balasubramaniam and A. Chai. Thermocapillary Migration of Droplets: An Exact Solution for Small Marangoni Numbers. J. Colloid Interface Sci. **119** (1987), 531-538.

[7] Y. K. Bratukhin. Thermocapillary Drift of a Viscous Fluid Drop. NASA Technical Translation NASA TT 17093 (1976).

[8] K. D. Barton and R. S. Subramanian. The Migration of Liquid Drops in a Vertical Temperature Gradient. J. Colloid Interface Sci. **133** (1989), 211-222.

[9] K. D. Barton and R. S. Subramanian. The Thermocapillary Migration of a Liquid Drop Normal to a Plane Surface. J. Colloid Interface Sci., **137** (1990), 170-187.

[10] B. Braun, C. Ikier, H. Klein and D. Woermann. Thermocapillary Migration of Droplets in a Binary Mixture with Miscibility Gap during Liquid/Liquid Phase Separation under Reduced Gravity. J. Colloid Interface Sci. **159** (1993), 515-516.

[11] J. Chen, Z. Dagan, and C. Malderelli. The Axysymmetric Thermocapillary MOtion of a Fluid Particle in a Tube. J. of Fluid Mech. **233** (1991), 405-437.

[12] J. C. Chen and Y. T. Lee. Effect of Surface Deformation on Thermocapillary Bubble Migration. AIAA J. **30** (1992), 393-408.

[13] R.Clift, J. R. Grace and M. E. Weber. Bubbles, Drops, and Particles, Academic Press, (1978).

[14] L. H. Dill and R. Balasubramaniam. Unsteady Thermocapillary Migration of Bubbles. NASA Technical Memorandum 101338, 1988, NASA Lewis Research Center.

[15] F. Feuillebois. Thermocapillary Migration of Two Equal Bubbbles Parallel to Their Line of Centers. J. Colloid Interface Sci., **131** (1989), 267-274.

[16] J. Hadamard. Movement permanent lent d'une sphère liquide et visqueuse dans une liquide visqueeux. Comptes Rendus. Academie des Sciences. **152** (1911), 1735-1738.

[17] J. Happel and H. Brenner. Low Reynolds Number Hydrodynamics. Prentice-Hall, Englewood Cliffs, N.J. (1962). 1989.

[18] S.C. Hardy. The Motion of Bubbles in a Vertical Temperature Gradient. J. Colloid Interface Sci., **69** (1979), 157-162.

[19] H. Haj-hariri, A. Nadim and A. Borhan. Effect of Inertia on the Thermocapillary Velocity of a Drop. J. Colloid Interface Sci., **140** (1990), 277-286.

[20] L. S. Chen and H. J. Keh. The Thermocapillary Motion of a Fluid Droplet Normal to a Plane Surface. J. Colloid Interface Sci., **137** (1990), 550-562.

[21] H. J. Keh and S. H. Chen. The Axysymmetric Thermocapillary Motion of Two Droplets. Int. J. Multiphase Flow, **16** (1990), 515-527.

[22] H. J. Keh and L. S. Chen. Droplet Interactions in Axysymmetric Thermocapillary Motion. J. Colloid Interface Sci., **151** (1992), 1-16.

[23] H. J. Keh and L. S. Chen. Droplet Interactions in Thermocapillary Migration. Chemical Engineering Sci., **48** (1993), 3565-3582.

[24] R. M. Merrit and R. S. Subramanian. The Migration of Isolated Gas Bubble in a Vertical Temperature Gradient. J. Colloid Interface Sci., **125** (1988), 333-339.

[25] R. M. Merrit and R. S. Subramanian. Migration of a Gas Bubble Normal to a Plane Horizontal Surface in a Vertical Temperature Gradient. J. Colloid Interface Sci., **131** (1989), 514-525.

[26] M. Meyyapan, W. R. Wilcox and R. S. Subramanian. Thermocapillary Migration of a Bubble Normal to a Plane Surface. J. Colloid Interface Sci. **83** (1981), 199-209.

[27] M. Meyyapan, W. R. Wilcox and R. S. Subramanian. The Slow Axisymmetric Motion of Two Bubbles in a Thermal Gradient. J. Colloid Interface Sci. **94** (1983), 243-250.

[28] M. Meyyapan and R. S. Subramanian. The Thermocapillary Motion of Two Bubbles Oriented Arbitrarily Relative to a Thermal Gradient. J. Colloid Interface Sci. **197** (1984), 291-294.

[29] M. Meyyapan and R. S. Subramanian. Thermocapillary Migration of a Gas Bubble in an Arbitrary Direction with Respect to a Plane Surface. J. Colloid Interface Sci. **115** (1987), 206-219.

[30] C.S. Peskin. Numerical analysis of blood flow in the heart. J. Comput. Phys. **25** (1977), 220-252.

[31] N. Rashidna and R. Balasubramaniam. Thermocapillary Migration of Liquid Droplets in a Temperature Gradient in a Density Matched System. Experiments in Fluids , **11** (1991), 167-174.

[32] N. Shankar and R. S. Subramanian. The Stokes Motion of a Gas Bubble Due to Interfacial Tension Gradients at Low to Moderate Marangoni Numbers. J. Colloid Interface Sci. **123** (1988), 512-522.

[33] J. V. Strape. Interactions and Collisions of Bubbles in Thermocapillary Motion. Phys. of Fluid **A 4** (1992), 1883-1900.

[34] R. S. Subramanian. Slow Migration of a Gas Bubble in a Thermal Gradient. AIChE J. **27** (1981), 646-654.

[35] R. S. Subramanian. Thermocapillary Migration of Bubbles and Droplets. Adv. Space Res. **3** (1983), 145-150.

[36] R. S. Subramanian. The Motion of Bubbles and Drops in Reduced Gravity. Transport Processes in Bubbles, Drops and Particles,Chhabra, R. P. and De Kee, D., ed., Hemisphere Publishing Corp., Washington, D.C., (1992), 1-42.

[37] J.A. Szymczyk and J. Siekmann. Numerical Calculation of the Thermocapillary Motion of a Bubble Under Microgravity. Chem. Eng. Commun., **69** (1988), 129-147.

[38] H. Lamb. Hydrodynamics. Dover Publishers, New York, (1932). 738 pages.

[39] L. D. Landau and E. M. Lifshitz. Fluid Mechanics. Pergamon Press, 1989.

[40] S. Ostrach. Low Gravity Fluid Flows. Annual Reviews of Fluid Mechanics, eds. M. Van Dyke, J.V. Wehausen, and J.L. Lumley, **14** (1982), 313-345.

[41] R. L. Thompson. Marangoni Bubble Migration in Zero Gravity. Ph.D. Thesis, The University of Toledo, 1979.

[42] R. L. Thompson, K. J. Dewitt and T. L. Labus. Marangoni Bubble Motion Phenomenon in Zero Gravity. Chem. Eng. Commun. **5** (1980), 299-314.

[43] L. M. Trefethen. Surface Tension in Fluid Mechanics. A color film by Encyclopedia Brittanica Educational Cooporation, Film No. 21610, (1963).

[44] D.R. Uhlmann. Glass Processing in a Microgravity Environment. Materials Processing in the Reduced Gravity Environment of Space, ed. G.E. Rindone, Elsevier, New York, (1982), 269-278.

[45] S.O. Unverdi. Ph.D. Thesis, The University of Michigan, 1990, 110 pages.

[46] S.O. Unverdi and G. Tryggvason. A Front Tracking Method for Viscous Incompressible Flows. J. Comput. Phys., **100** (1992a), 25-37.

[47] G. Tryggvason, D. Juric, M.H.R. Nobari, and S. Nas Computations of Drop Collision and Coalescence. Second Microgravity Fluid Physics Conference, NASA CP-3276, Clevaland, Ohio, June 21-23, (1994), 135-140.

[48] S.O. Unverdi and G. Tryggvason. Multifluid flows. Physica D **60** (1992b), 70-83.

[49] H. Wei and R. S. Subramanian. Thermocapillary Migration of a Small Chain of Bubbles. Phys. of Fluids **A5** (1993), 512-522.

[50] G. Wozniak and J. Siekmann. Experimental Investigation of Thermocapillary Droplet Motion in Reduced Gravity - Two Sounding Rocket Experiments. Appl. Microgravity Tech., **2** (1989), 173-175.

[51] G. Wozniak, J. Siekmann, and J. Srulijes. Thermocapillary Bubble and Drop Dynamics Under Reduced Gravity - Survey and Prospects. Z. Flugwiss, Weltraumforsch, **12** (1988), 137-144.

[52] N. O. Young, J. S. Goldstein and M. J. Block. The Motion of Bubbles in a Vertical Temperature Gradient. J. Fluid Mech., **6** (1959), 350-356.

[53] X. Zhang and R. H. Davis. The Collision Rate of Small Drops Undergoing Thermocapillary Migration. J. Colloid Interface Sci., **152** (1992), 548-561.

ABSTRACT

COMPUTATIONAL INVESTIGATION OF THERMOCAPILLARY MIGRATION OF BUBBLES AND DROPS IN ZERO GRAVITY

by

Selman Nas

Chairperson: Associate Professor Grétar Tryggvason

The thermocapillary migration of many bubbles and drops in zero gravity is studied numerically in two and three dimensions. The full Navier-Stokes equations and the energy equation for the temperature, are solved for the fluid inside and outside of the bubbles and drops by a front tracking/finite difference method. The method is verified by comparison with analytical solution in the limit of zero Reynolds, Marangoni and Capillary numbers and good accuracy is found. It is found that two bubbles, initially oriented arbitrarily with respect to the temperature gradient, tend to line up, side by side, perpendicular to the temperature gradient in both two and three dimensions. The interaction between two drops, on the other hand, is different. Only in the low Re and Ma number region drops do behave like the bubbles, but when both the Re and the Ma are high, they tend to line up in tandem. Drops also deform more than bubbles, along the direction of the temperature gradient.

Numerical simulations of a large mono-dispersed bubble system show that the bubbles form horizontal layers. As soon as the bubbles form one layer that fills the channel horizontally, the rest of the bubbles form another layer. Although these layers sometimes break up by instability waves, the layers are eventually regenerated. Three-dimensional simulations confirm this tendency to form layers while simulations of bubbles in polydisperse systems show the same behavior. In contrast to the two dimensional simulations of polydisperse systems, where bubbles of different size form a horizontal layer, a three dimensional simulation of a polydispersed system shows that different sizes of bubbles form different layers.